Measurement accuracy in Network-RTK

Ragne Emardson, Per Jarlemark, Sten Bergstrand, Tobias Nilsson, and Jan Johansson

Project Team

The project team consists of members from SP Technical Research Institute of Sweden and Chalmers University of Technology.

The project team at SP consists of Ragne Emardson, Per Jarlemark, Sten Bergstrand, and Jan Johansson

The project team at Chalmers consists of Tobias Nilsson and Jan Johansson

Abstract

This report presents the results of the project "Close – <u>C</u>halmers, <u>L</u>antmäteriet, <u>O</u>nsala, "ä<u>SPe</u>"". Real Time Kinematic (RTK) is a system that utilises Global Navigation Satellite Systems (GNSS) to provide accurate positioning in real time. In this report, we study the different errors affecting measurements with the network-RTK technique. We assume a network configuration with distances between the reference stations of 70 km. The main error sources are troposphere and ionosphere variability, and local effects, such as receiver noise and multipath.

In the study, we find that the inclusion of future satellite systems such as Galileo and Compass can reduce the error in the vertical position estimate from 27 mm to 20 mm. The optimal choice of elevation cutoff angle also changes from approximately 13 degrees today to approximately 25 degrees. For times with a high spatial variability in the ionosphere, the L3 combination can be preferable. A densified network with 35 km between the reference stations results in a similar improvement as the contribution of the new satellite systems. The error in the vertical position coordinate estimate is reduced from 27 mm to 20 mm. Using both a densified network and the new satellite systems reduces the error in the vertical component further down to 14 mm. For dense network, such as distance between the reference stations around 10 km, the vertical error is 11 mm and down to 8 mm for the full future satellite constellation.

Key words: GNSS, GPS, RTK

Contents

Preface

This report is a result of the project Close which is ordered from Lantmäteriet. The purpose of the project is to determine the current quality of network-RTK based on an analysis of the error sources affecting the quality. An aim is also to find out different measures to improve the quality of network-RTK and to get improved knowledge of spatial and temporal correlations. The main focus of the project is on height determination.

1   Introduction

The project reported in this publication is divided into three work packages. Work package 1 (wp1) deals with the current standard of network-RTK. Wp2 contains evaluation of future network-RTK quality based on the changes that will occur in infrastructure, such as the introduction of the Galileo system. Finally in wp3, we investigate the possibilities for new algorithms and methods that will increase the accuracy of network-RTK. Below, we report the findings from the work in the different work packages.

2   Work Package 1

2.1   Detailed investigation of current RTK

Real Time Kinematic (RTK) is a system that utilises Global Navigation Satellite Systems (GNSS) to provide accurate positioning in real time. The reader is assumed to be familiar with GNSS concepts and related terminology in large. A minor collection of terms and acronyms is attached to this document.

The general idea in RTK is to receive GNSS-signals at a stationary reference with known position coordinates and to use these to correct position data at a roving receiver in another location. The ideal signal is perturbed by ionosphere, troposphere and imperfections related to ephemerides, clocks and multipath (historically also Selective Availability, SA) and thus the calculated position coordinates differ from the known coordinates. By calculating corrections that mathematically "moves" the reference to its known position and subsequently apply a similar set of corrections to the rover, the rover's position can also be determined very accurately. As the reference and rover are at different locations, the signals have been perturbed differently and the correction data are therefore affected by uncertainties that compromise the reliability of the rover's corrected position. The factors that affect the uncertainties can be classified in different ways, e.g. distance dependent, systematic, random, site specific, rapid, frequency dependent (dispersive).

With RTK it is also implicit that, in addition to the broadcast code signals that are handled by relatively cheap off-the-shelf products, the carrier phase of the signal is analysed with a geodetic receiver. With this technique it is possible to obtain position coordinates with accuracy of order 1 cm. The difference between RTK and Network RTK is that the latter combines data from several reference stations to provide the rover with corrections. With Network RTK the distance dependent errors are interpolated between the reference stations, which allows for increased distance between reference stations without losing position accuracy.

The data flow in the process can be split into several general steps that are shown in Figure 1 [*Euler,* 2008]. Depending on the chosen strategy, these steps can be distributed or combined in different ways.
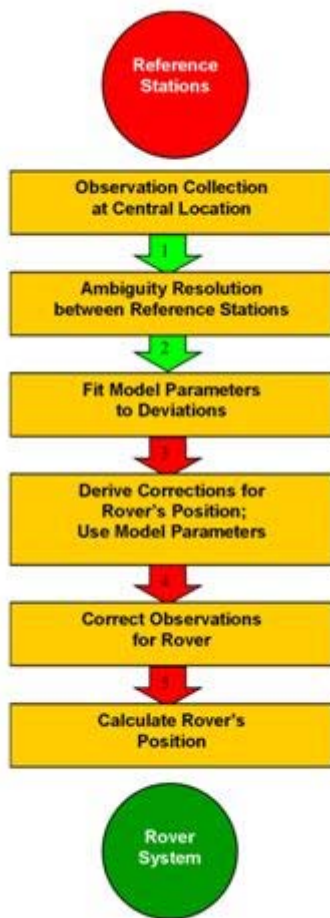
Figure 1   **The general computational steps involved in network RTK. From** *Euler,* **[2008].**

Currently, two main strategies for network RTK can be identified: Virtual Reference Station (VRS) developed by Trimble, and Master-Auxiliary Concept (MAC) developed by Leica Geosystems. In addition, another strategy that uses area correction parameters (FKP from German Flächenkorrekturparametern) was developed by Geo++ in the mid nineties is still in use. All methods adhere to the flow depicted in Figure 1, but distribute the computational load between central software and rover differently. For VRS, the interface between central software and rover is at step 5, for MAC the interface is at step 2 and for FKP the interface is at step 3.

All three major vendors of RTK equipment in Sweden (Leica Geosystems, Topcon and Trimble) have software that supports VRS for central software as well as for rovers. Currently, MAC is supported by Leica Geosystems and Trimble receivers, not Topcon [*Topcon,* 2007]. The FKP method and vendors with minor market shares have not been considered in the project.

Virtual Reference Station, VRS

Methodology: The rover calculates a position from uncorrected code data like any off-the-shelf receiver and uploads this navigated solution to the central unit. The central software then deploys a virtual reference station at the coordinates of the initial navigated solution on the common phase ambiguity level that is calculated from data from an appropriate combination of the surrounding reference stations. From the synthetic data of

the calculated surface, the VRS emulates a real reference receiver at the initial navigated coordinates. The rover receives the VRS data and makes a phase adjustment of its own position on the relatively short baseline.

Master-Auxiliary Concept, MAC

MAC may be used as either a one-way or two-way communication system with minor modifications. Methodology in the case of two-way communication: As for the VRS, the rover uploads its navigated position to the central unit. The central software then appoints the closest reference station as Master and then transmits raw data from the Master and an appropriate set of Auxiliary stations to the rover. The rover receives raw data from the appointed stations and makes phase corrections to all of these.

Area Correction Parameters, Flächenkorrekturparametern, FKP

Methodology: The reference network broadcast RTK data from a base station in the network along with a set of model parameters of the distance dependent errors. The rover evaluates the area correction parameters at its own position and adjust its position accordingly. The broadcast parameters are typically linear east-west and north-south gradients and are thus limited around each base station.

Vulnerable/weak parts of the concept

This section deals solely with GNSS aspects of Network RTK. Geodetic aspects such as geoid models, map projections etc are important but not addressed here. Practical aspects such as power failures, communication breakdowns between reference stations and the central unit as well as central unit and rover respectively, are important but not addressed further in this report. In case of a reference station outage, the use of models in a broadcast solution may result in different model recalculations and subsequent production loss. In case of broadcast raw observations, such outages will not affect productivity, but the end result will nevertheless be a less dense network and affect the uncertainties of different strategies similarly.

Satellite geometry is crucial for accurate measurements. The general overall GNSS design was for unaided code observations and was specified to a global coverage with at least four satellites in view above five degrees elevation at 99.9% of the time. As phase observations for 3D positioning requires five observable satellites, short periods occur when RTK measurements are impossible with one GNSS system only. A combination of several GNSS's, e.g. GPS/Glonass will increase the feasibility of an RTK solution. Also poor satellite configuration, i.e. satellite distribution in the observer's sky-view, results in increased dilution of the precision (DOP). Sky-blocks close to house walls, under tree canopies, etc inhibit GNSS observations.

The satellite characteristic to be viewed only above the horizon means that satellites are visible in all horizontal quadrants but only in the receiver's celestial hemisphere. The end result is that the vertical component of the receiver's position is less constrained than the horizontal and, accordingly, vertical position estimates are more uncertain than the horizontal, see Figure 2.
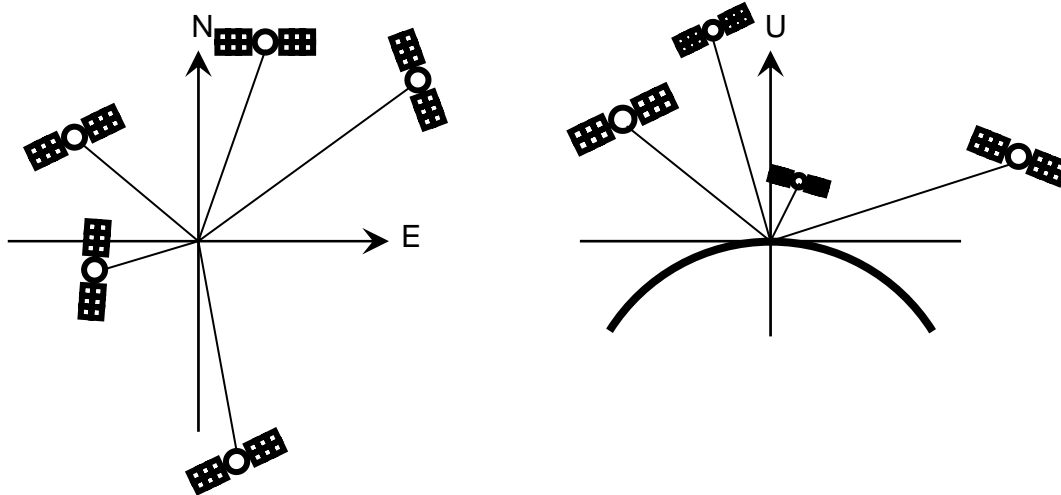
Figure 2　　**Satellite availability in a local receiver coordinate system (East, North and Up). As no satellite observations are possible below the horizon, there are generally weaker vertical constraints on the receiver's position and hence larger uncertainty in that component.**

As the satellite signal is perturbed by the neutral as well as the electrically charged part of the atmosphere, atmospheric models needs to be incorporated in the calculations of position estimates. For GNSS signals, the important neutral part is referred to as troposphere and the charged part the ionosphere. As signals from low elevation satellites experience much atmospheric disturbance, those observations are also less certain than those of higher elevation satellites. Should the network incorporate a band of extrinsic stations, effectively extending the operational area to an outer boundary zone, improved reliability would result at the core-network boundaries due to earlier detection of e.g. weather fronts. Inclusion of external data, e.g. to have highly reliable and densely spaced weather data in real time, could improve system performance.

Modelling may be performed slightly differently between different software. This may result in different position estimates from identical observation data, with increasing errors depending on baseline lengths and height difference between reference and rover. *Landau et al* [2003] made such a comparison including different models as well as values for temperature, pressure, and humidity. *Landau et al* [2003] used a modified Hopfield model [*Goad and Goodman*, 1974] as standard troposphere for the reference network. For the dispersive part, i.e. the ionosphere it is possible that the Klobuchar model parameters that are incorporated in the GPS code is not used, and that local real-time corrections are used instead [*Kolb et al.*, 2006].

GPS broadcast signals on two frequencies, L1 and L2, mainly to compensate for the dispersive effects of the ionosphere. During periods of high ionospheric activity in the 11 year solar cycle, these dispersive effects increase as do the risk of lost phase locks or cycle slips. L3, which is a linear combination of L1 and L2, gets rid of the vast majority of the ionosphere's contribution to position uncertainty. In a broadcast solution such as VRS where distances between reference and rover appear to be short, the information of the ionospheric differences between reference and rover are lost. *Brown et al*. [2006] as well as *Takac and Lienhart* [2008] showcased instances where the neglected L3 information in a broadcast solution called "Standard Net RTK" resulted in poorer performance compared to the MAC strategy under non-linear ionosphere conditions.

Different approaches have been used to convey the reference system performance to the rover [*Chen et al,* 2003*, Alves et al,* 2005*, Takac and Lienhart,* 2008]. With a broadcast solution strategy, distance dependent errors are hidden to the rover since the virtual baseline is short whereas the true distances to reference stations are considerably longer. As in the case above, the information of the uncertainty that is imposed by e.g the atmospheric modelling is thus not available to the rover.

In addition to the atmospheric effects, antenna characteristics are also elevation dependent. Such dependence can be compensated by knowledge of the antenna characteristics. In the rover, several antenna models to choose from are provided, so that the correct antenna model characteristics are taken care of in the calculation of the rover's position estimate. It is important to use consistent values for reference and rover antenna models in order not to impose an error in the position estimate, cf. *Johnsson and Wallerström* [2007].

Error sources that are site specific or unalike for reference stations and rovers will propagate in the solution and result in erroneous position estimates. Antenna uncertainties affect references and rovers similarly but unequally and thus increase the uncertainty of the final position estimate. In addition to the reference station aspects, uncertainties beyond the influence of the provider of correction signals need to be considered on the rover side of the system. At reference sites uncertainties include but aren't limited to:
-physical misalignment of the reference antenna with respect to the corresponding appointed marker
-electromagnetic disturbances, such as electromagnetic coupling between antenna and monument
-stability of antenna foundation e.g. with respect to ground movements and ambient temperature
-phase centre variations including uncertainties of phase centre position with respect to physical antenna centre and ditto base
-elevation and azimuth dependence of the antenna
-signal delay due to moist/frost/snow in and on radomes
In addition to the reference station maintenance, user related errors and negligence of periodic and proper maintenance on the rover side may degrade system performance significantly. For a hand-held rover, the factors above need to be complemented with at least:
-GPS pole height calibration
-appropriate choice of bubble level resolution
-adjustment of bubble level horizontation
-pole tilting during observation point occupation
-number of observations on each position
-ground imprint
-marker quality
In the case of a machine guidance rover, e.g. an excavator, a number of additional parameters are added to get to the designated point of interest on the machine and consequently increase the complexity of the system. All the combinations of individual lengths, orientations and tilts of the excavator's boom, stick and different buckets add to the uncertainty. In this case and many others, the rover terms add significant uncertainty to the positioning result and the importance of rover calibration becomes increasingly important. As these terms may vary greatly between individual users on the rover side and aren't directly related to the Network RTK performance per se, they are mentioned here to extend the view of the uncertainty of the end result.

Especially earlier but still effective, critique has been aimed at the use of proprietary information in messages, which result in considerable production loss when combining equipment of different brands. Subsequent to the use of the RTCM 3.0 format and higher,

this should no longer be a problem. As a note, several instances of problems have also occurred with single RTK at privately administrated construction sites in conjunction with the combined use of GPS/Glonass satellites and receivers of different brands (different representatives, personal communication). This is probably due to a lack of information dissipation and would affect single and Network RTK equally.

An example of the benefit with using network-RTK compared to single station RTK can be seen in Figure 3 and Figure 4. The figures show the contribution from the ionosphere on the L1 observable. Figure 3 shows the ionospheric delay on L1 for different observations to different satellites during one day. In the figure, the individual satellite curves are arbitrarily offset due to unknown phase offsets. Note that for specific satellite observations this delay can vary some meters. Figure 4 shows how this delay can be interpolated, and thus compensated for, using one reference station only or an entire network of stations. The figure shows the interpolation error for a single satellite observation with a duration of five hours. The blue curve shows the interpolation error for the site Borås when the ionosphere is interpolated from the reference station Falköping and the red curve shows the interpolation error for the site Borås when the ionosphere is interpolated from three reference stations, namely Falköping, Rörö, and Ätran.
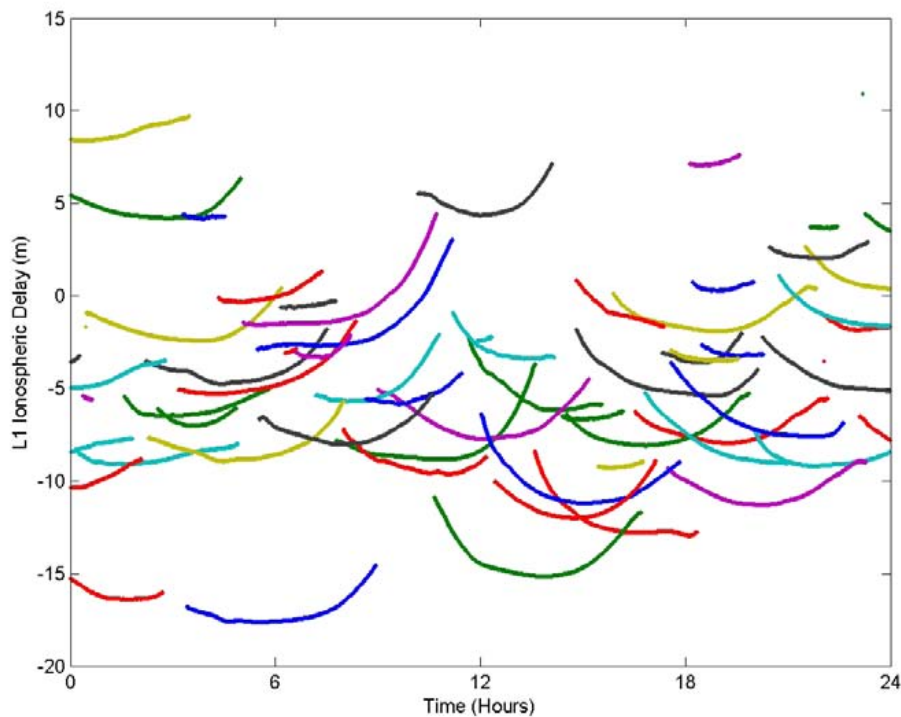

Figure 3   **Ionospheric delay on L1 for the Borås site during 24 hours.**
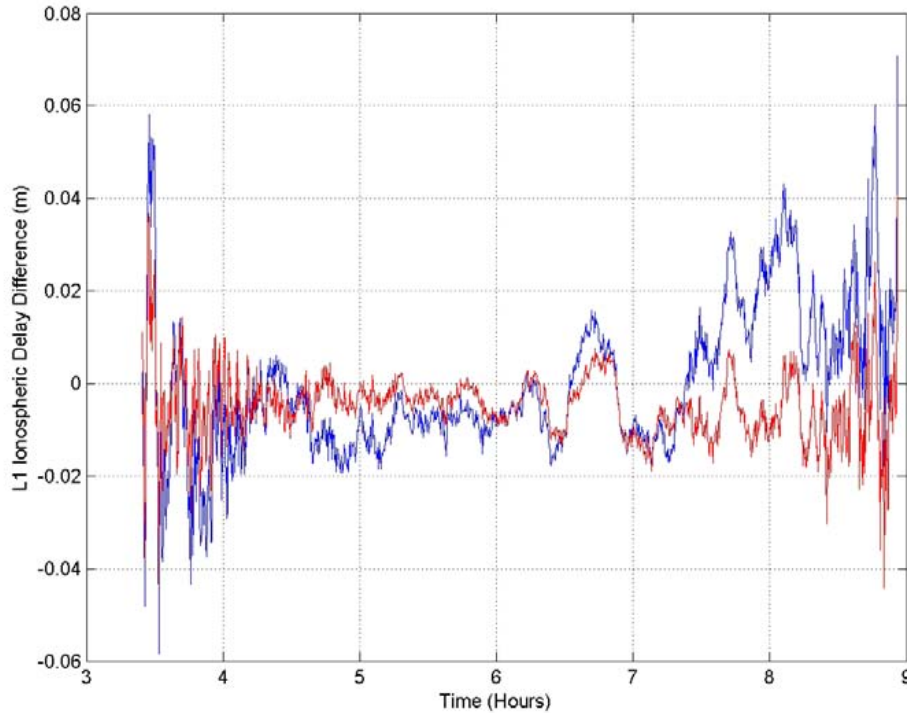
Figure 4   **Interpolation error based on single station RTK (blue) and network-RTK (red).**

2.2   Error budget

In this part, we investigate the different error sources affecting network-RTK in order to produce an error budget. Below we introduce the assumptions made during the simulations. This is followed by short descriptions of the different error sources, how they affect the position estimates and how we model them. Finally the different error sources are put together in the summary part.

We report all errors in network-RTK as the square root of the variance of the errors. Hence, hereafter all reported errors are presented this way.

We suggest that the presented errors in this reported are used in order to evaluate the measurement uncertainty of performed network-RTK measurements. The measurement uncertainty is defined as a non-negative parameter characterizing the dispersion of the quantity values being attributed to a measurand, based on the information used [*VIM*, 2008]. The presented errors correspond to the standard measurement uncertainties. These standard uncertainties can then be multiplied with a coverage factor, k, in order to obtain an expanded measurement uncertainty, U. The result of the measurement can then be expressed as $Y = y \pm U$, where Y can be, for example the height component of a position. This should be interpreted as that the estimate of the value attributable to the measurand Y is y and that $y-U$ to $y+U$ is an interval that may be expected to encompass a large fraction of the distribution of values that could reasonably be attributed to Y [*GUM*, 2008]. By choosing $k=2$, we obtain an interval having a level of confidence of approximately 95% and choosing $k=3$ produces an interval having a level of confidence of approximately 99%.

2.2.1   Assumptions

We assume a network configuration as outlined in Figure 5. The distance, d_{ref}, between the reference stations are 70 km. When positioning a rover as depicted in Figure 5 as a blue circle, we use information from the surrounding reference stations. In our configuration, we use measurements from six surrounding reference stations. Three of those form an inner triangle and the rest form an outer triangle.
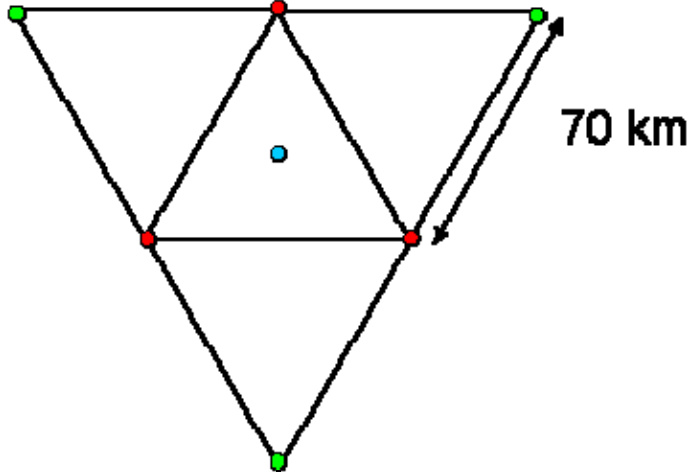

Figure 5   **Network configuration. For an explanation of the symbols, see text.**

Here the distance from the rover to any reference station in the inner triangle is

$$d_a = d_{ref} / \sqrt{3} \tag{1}$$

and the distance from the rover to a reference station in the outer triangle is

$$d_b = 2d_{ref} / \sqrt{3} \tag{2}$$

where in the nominal situation $d_{ref} = 70$km. Hence the interpolated phase, which constitutes the virtual reference station, at the site of the rover can be written as:

$$\varphi_r = \sum_i w_a \varphi_i + \sum_j w_b \varphi_j \tag{3}$$

Where we choose the weights w_a=2/9 and w_b=1/9 for the inner and outer reference stations respectively. This choice is a trade off between an optimal choice for atmospheric interpolation where we benefit from higher weights on the stations in the inner triangle (see Figure 15)and optimal choice for local effects where an optimal weighing would be w_a=w_b=1/6.

Here we assume that broadcast satellite positions and a priori atmospheric delay are removed from the phase observables before the summation above. We also assume that all *a priori* phase ambiguities are fixed to integer values. Ambiguity fixing can be difficult under certain conditions. However in this report, we do not cover this field. We focus on measurement accuracy given that the fixed integer values are correct. We assume that no structural variations or systematic errors in the reference network used

exists. We assume no height variations in the reference network. This effects is described in the section about troposphere influence. We assume that the operator uses the equipment correctly and not introduce additional errors by erroneous handling.

The baseline approach in this study is to use L1 observations only. All observations are weighted with respect to their elevation angle. The weighing function is sin(ε). Simulations show that the choice of weighting function has a rather insignificant impact on the final results. Using the chosen weighting reduced the impact of the tropospheric delay by 10% compared to the use of equal weights. Hence, we have not tried to imitate any specific software in this respect. The rover estimates 4 parameters, namely east, north, height, and local clock offset to the virtual reference station. The integration time of the observations for the rover is one sample.

2.2.2 Observations

In order to study the different error sources in network-RTK applications, we model the received signals by the GNSS receivers. The phase measurements from the rover and the reference receiver can be described by (4) and (5), where φ is the measured phase in fraction of cycles, ρ is the true geometrical distance between the receiver and the satellite, N is the integer number of cycles referred to as the ambiguity parameter. The δt^t and δt^r represents the satellite and receiver clock error respectively, l_o is the error in the reported satellite position, l_t is the signal delay in the lower part of the atmosphere referred to as the troposphere, l_i is the signal delay in the ionosphere part of the atmosphere, m is signal multipath, and ε is measurement error. λ is the signal wavelength and f is the signal frequency.

$$\varphi_A = \frac{1}{\lambda}\rho_A + N_A + f\ (\delta t_A^t + \delta t_A^r) + \ell_o + \ell_i + \ell_t + m + \varepsilon \tag{4}$$

$$\varphi_B = \frac{1}{\lambda}\rho_B + N_B + f\ (\delta t_B^t + \delta t_B^r) + \ell_o + \ell_i + \ell_t + m + \varepsilon \tag{5}$$

Forming the difference between the observed signals at the rover and the reference station, we obtain an observable that can be used for determining the vector between the rover and reference position. By multiplying (4) and (5) with the signal wavelength and subtracting them the, we obtain a phase difference measurement:

$$\lambda\varphi_D = \Delta\rho + c\delta t_D^t + \Delta\ell_o + \Delta\ell_i + \Delta\ell_t + c\delta t_D^r + m_D + \varepsilon_D \tag{6}$$

Here, we assume that the local ambiguities are resolved. Hence, we can write the displacement vector Δρ as:

$$\Delta\rho = \lambda\varphi_D - (c\delta t_D^t + \Delta\ell_o + \Delta\ell_i + \Delta\ell_t + c\delta t_D^r + m_D + \varepsilon_D) \tag{7}$$

That is the sought displacement vector equals the phase measurement difference plus the errors in satellite clocks, satellite orbits, delay in the ionosphere, delay in the troposphere, local clocks, environmental multipath, and receiver noise. Below, we describe the different error sources and explain how they influence the network-RTK position estimates.

2.2.3 Satellite clocks

Information on satellite clock offsets are included in the broadcast message received by the GNSS receivers. This information contains errors of the order 10 ns [*IGS,* 2009]. However, the effect of satellite clock errors is identical for the rover as for the reference stations. As a consequence the errors are cancelled when using the network corrections. Hence satellite clock variations pose no problem in RTK positioning. A minor exception is the earlier selective availability (SA) that was removed from the GPS system in may 2000. Such rapid variations in the satellite clock behaviour can offset the sampling of the receivers in the network-RTK systems and in this way affect the results.

2.2.4 Satellite orbits

Information on satellite orbits are included in the broadcast message received by the GNSS receivers. This information contains errors of the order a few meters. For a single reference station baseline with a baseline length r, a satellite orbit error e_o at distance R to the satellites results in an error in the estimated position, e_p, of approximately

$$e_p \approx e_o \cdot \frac{r}{R} \qquad (8)$$

This approximation can be derived from Taylor expansion. For broadcast orbits, that are used in RTK applications, we can assume that the orbit error is of the order 2 m [*IGS,* 2009]. If the distance between reference and rover is of the order r=50-100 km , and R=20 000 km, we have errors of 5-10 mm due to the satellite orbits. However, for Network-RTK with at least 3 reference stations and a linear geographical interpolation the effect is cancelled to the 1:st order. Hence the estimated position, e_p, is approximately

$$e_p \approx e_o \cdot \left(\frac{r}{R}\right)^2 \qquad (9)$$

The following term will be of the order of less than 0.1 mm based on the assumptions above. Hence we assume this error source to be equal to zero in the following analysis.

2.2.5 Ionosphere

The ionosphere is a dispersive medium. That is, the refractive index depends on the signal frequency. A consequence of this property is that the GPS signal delays on L1 and L2 are different through the ionosphere. Hence a technique to remove a large part of the contribution from the ionosphere is to form a linear combination, L3, of the L1 and L2 observables [e.g., *Hoffman-Wellenhof et al*, 1994]

$$L_3 \approx 2.55L_1 - 1.55L_2 \qquad (10)$$

Another common practice is to use L1 only which is suitable for short baselines where ionospheric variations to a large extent are cancelled when differencing observations.

Figure 6 shows the observational geometry for the ionosphere. Note that the distance from the antennas to the point of intersection between the signals and the main part of the ionosphere is much larger than the distance between the reference stations in the RTK-network.
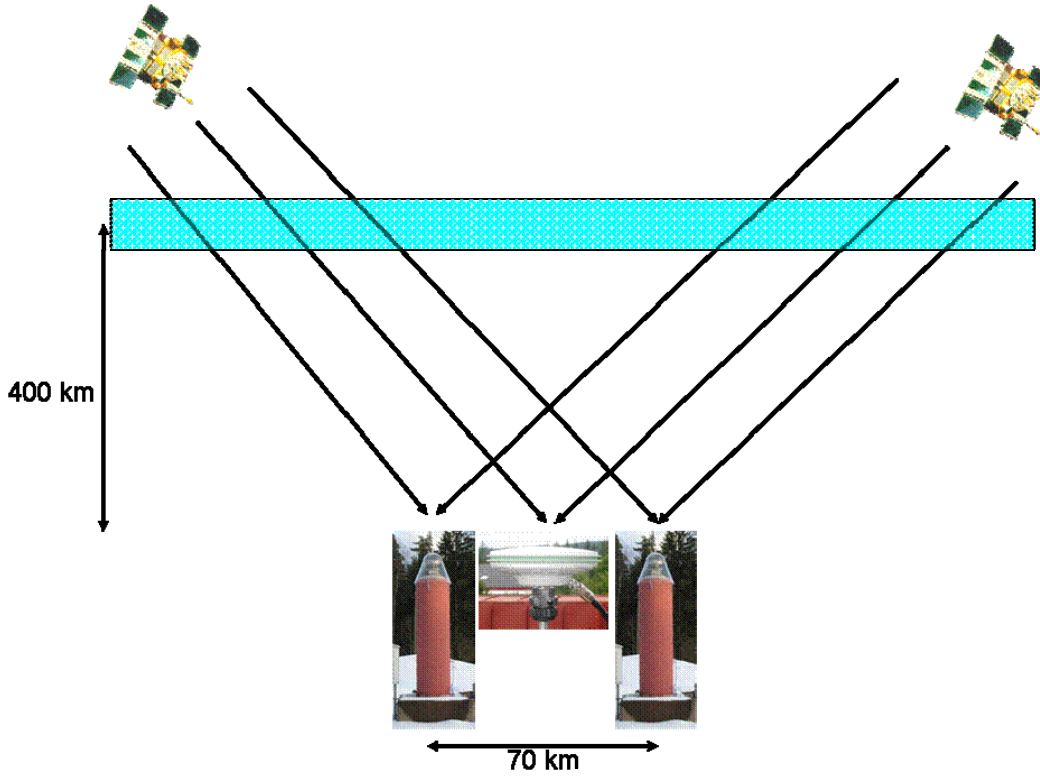
Figure 6   Observational geometry for the ionosphere

In the following, we use observations of the ionospheric delay from Rörö, Falköping, and Ätran to interpolate the ionospheric delay for the site Borås. We then compare the interpolated time series with the measured using the observations from the Borås site. Figure 7 shows the root mean square (rms) differences between the interpolated ionosphere and the measured. All data are from the year 2008. Each curve represents observations for one day. The results have been grouped in bins of 3 degrees. Figure 8 shows the same differences mapped to equivalent zenith values with the standard ionospheric mapping function, which can easily be derived from the geometry of the ionosphere:

$$m_i(\varepsilon) = \frac{1}{\cos\left(\arcsin\left(\dfrac{R\sin(\varepsilon + \pi/2)}{R + h}\right)\right)} \tag{11}$$

Where ε is the elevation angle of the observation, R is the radius of the earth and h is the height of the ionosphere, here represented as a thin shell. Most of the elevation angle dependent features is then removed, which indicates that the mapping function can be used in the model for predicting ionospheric interpolation errors.

Figure 7 shows the ionospheric delay error as a function of elevation angle. Each curve represents one day of observations. For each satellite observation, we determine the network interpolation error, as in Figure 4 (red curve). We calculate the rms of the errors for all observations during one day for a set of elevation angles, which is shown in the figure. Figure 8 shows the same ionospheric delay error, but mapped to zenith using (11). To a large extent this removes the elevation dependence of these errors.
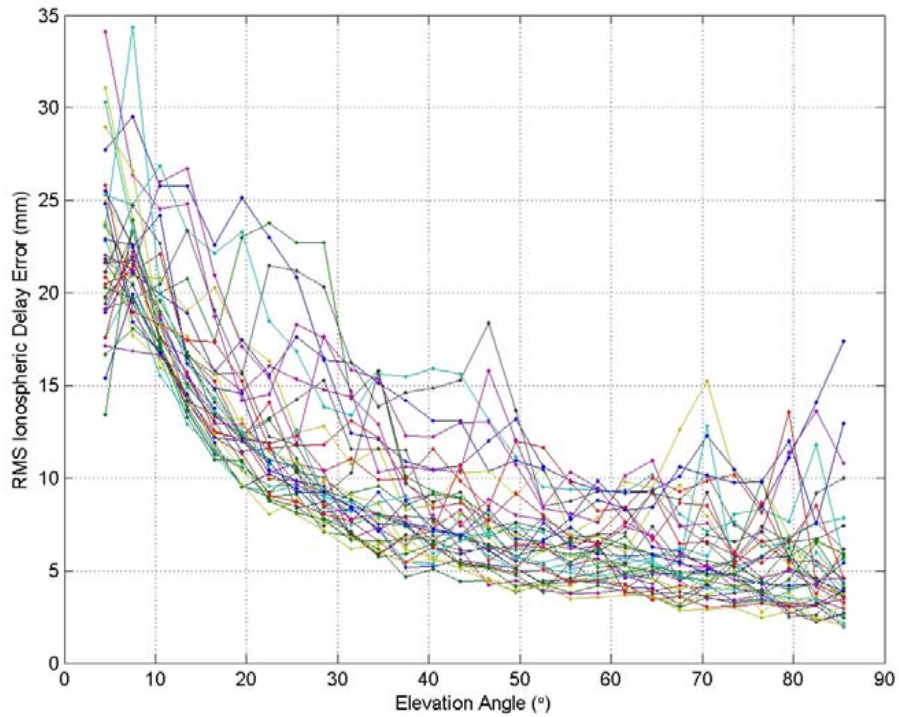
Figure 7   **Ionospheric delay error as a function of elevation angle. Each curve represents one day of observations during 2008.**
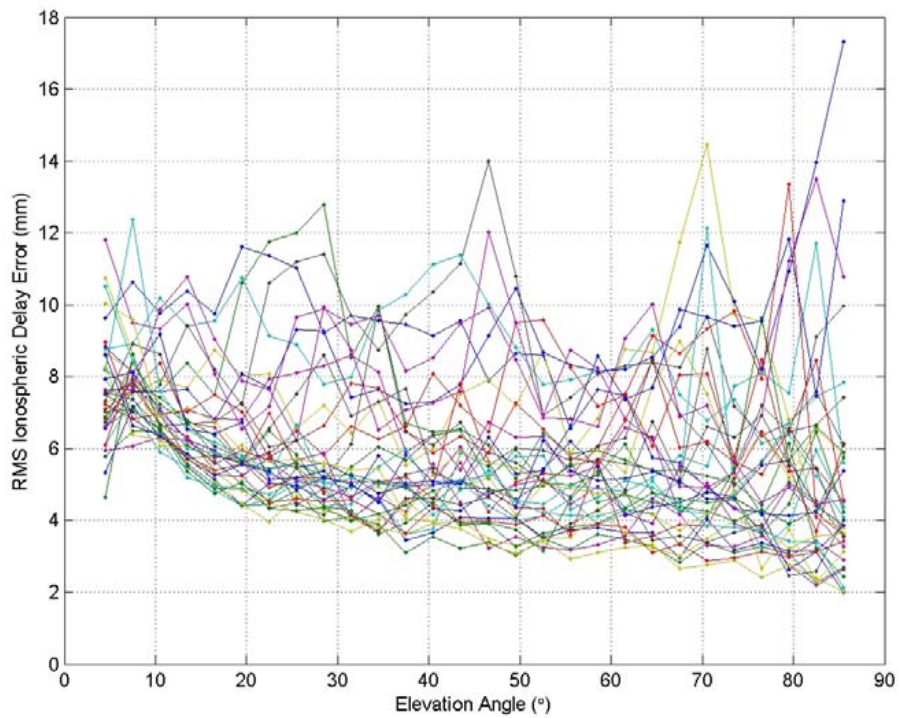

Figure 8   **Ionospheric delay error as a function of elevation angle. The values have been mapped to equivalent zenith values. Each curve represents one day of observations during 2008.**

We use mean zenith mapped values between 15 and 40 degrees for each day, see Figure 8, to form the values in Figure 9. Here the interpolation errors are plotted against daily mean vertical TEC. In the figure data from both 2003 and 2008 are shown. The straight line represents a least squares fit to the data points. This is the model we hereafter use to estimate ionospheric interpolation error based on daily mean vertical TEC values.
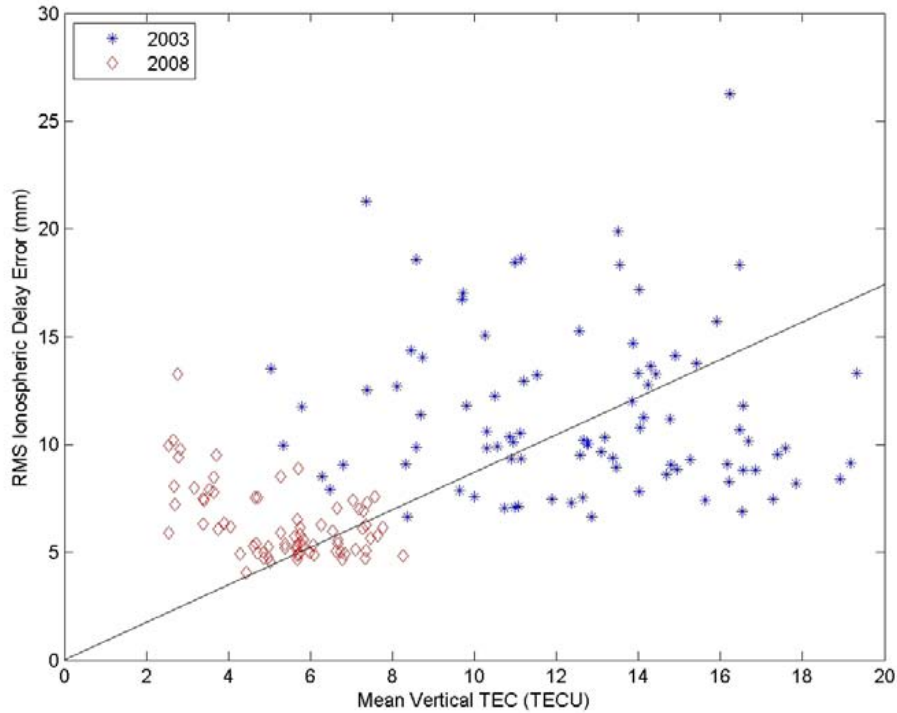
Figure 9   **Interpolation error of the ionospheric delay error as a function of daily mean value of vertical TEC.**

Figure 10 shows the daily mean vertical TEC during half a solar cycle for a typical Swedish location. We can see that the averaged values during the half solar cycle varies from below 5 TECU to almost 20 TECU during the period. Hence the interval represented in Figure 9 is relatively representative for Swedish conditions. However, TEC values vary geographically. The mean TEC for the period is approximately 11 TECU. Figure 11 shows the distribution of the daily mean TEC during the same period. From this data set we choose 3 TECU and 25 TECU for representative values for the lower 5% and higher 95% respectively.
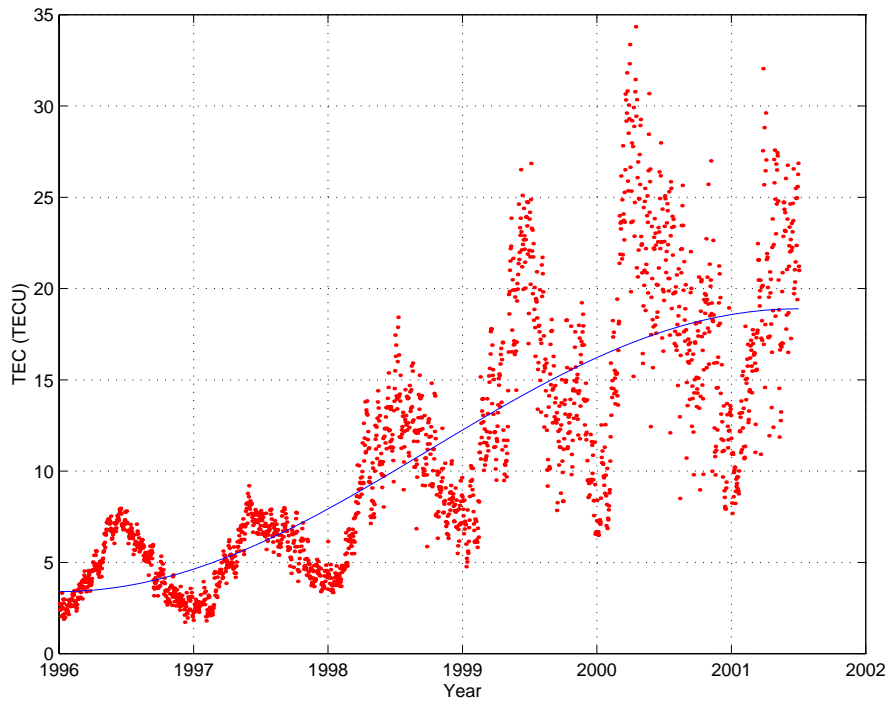
Figure 10   **Daily mean vertical TEC during half a solar cycle for a typical Swedish location.**
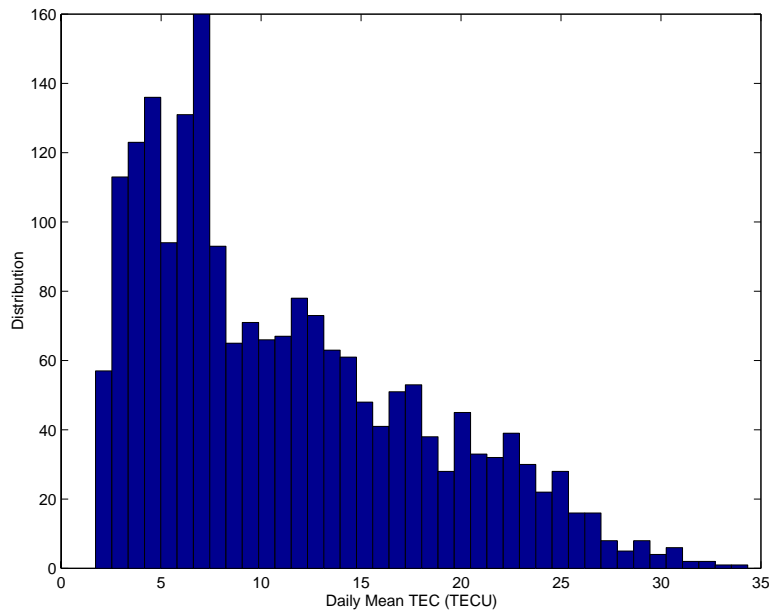
Figure 11   **Number of days with specified daily mean TEC during half a solar cycle.**

Figure 12 shows the ionospheric delay variance as a function of distance between the reference stations. We estimate the ionospheric delay in Borås using three sets of reference stations. The straight line shows a lest squares fit of a straight line to the data points. We use this model for scaling the ionospheric errors to different distances between reference stations.
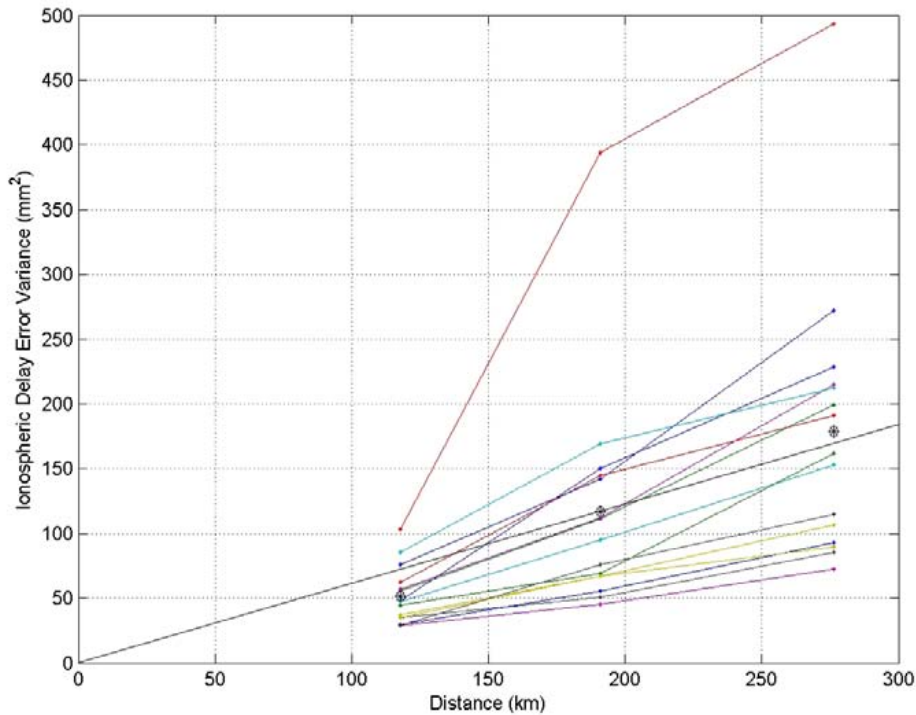
Figure 12   Ionospheric delay error variance as a function of distance between reference stations.

Based on the information above, we can make statistics on the ionospheric influence on measured GNSS observations. Table 1 shows the summary of the ionosphere statistics and its effect on range interpolation error for the nominal reference network with distance between reference stations of typically 70 km.

Table 1 Summary of ionosphere statistics and its effect on range interpolation error

	Nominal	5%	95%
TEC (TECU)	11.1	3	25
Interpolation Error (mm)	7.2	2.0	16.3

2.2.6   Troposphere

The troposphere is the lower part of the atmosphere, usually below 10 km, see Figure 13. For simulation purposes we divide the contribution from the troposphere into two parts, namely a hydrostatic part and a wet part, that is the troposphere component due to water vapor.

Hydrostatic delay

The hydrostatic delay is greater than the wet delay. It is approximately 2 m in the zenith direction. It is, however, relatively easy to suppress due to very strong horizontal spatial correlation. The vertical hydrostatic delay is a function of the local atmospheric pressure. [e.g., *Saastamoinen*, 1972]. A pressure gradient of 4 mbar over a distance of 100 km results in a difference in the zenith delay of 10 mm over the same 100 km reference network. This delay gradient is relatively smooth as it follows the pressure gradient. Hence, a linear combination, such as (3), cancels this effect almost completely.

The hydrostatic delay is height dependent. When the reference stations and the rover or a virtual reference station are at different heights, the hydrostatic delay has to be adjusted to the correct height. As an example does a 1 m height difference result in a 0.3 mm correction of the hydrostatic delay. If the temperature changes by 20 K this correction model is wrong by approximately 10%. Hence the hydrostatic delay is wrong by 0.03 mm in delay. The resulting error in the estimate of the vertical component of this delay error of 0.03 mm is approximately 0.1 mm. We have not included this effect further in the analysis in this report. However, for geographical areas with large topographical variations this effect should be taken into consideration.

Wet delay
The wet delay is much smaller than the hydrostatic delay, typically below 30 cm in the Nordic countries. However, because of its relatively high spatial and temporal variability it is usually a more serious error source in GPS applications.

The spatial variations in the zenith wet delay, l_w, are often described statistically using a function, D, of the distance d

$$D_w(d) = Var[\ell_w(r+d) - \ell_w(r)] \tag{12}$$

A common model for D is

$$D_w(d) = C \cdot d^\alpha \tag{13}$$

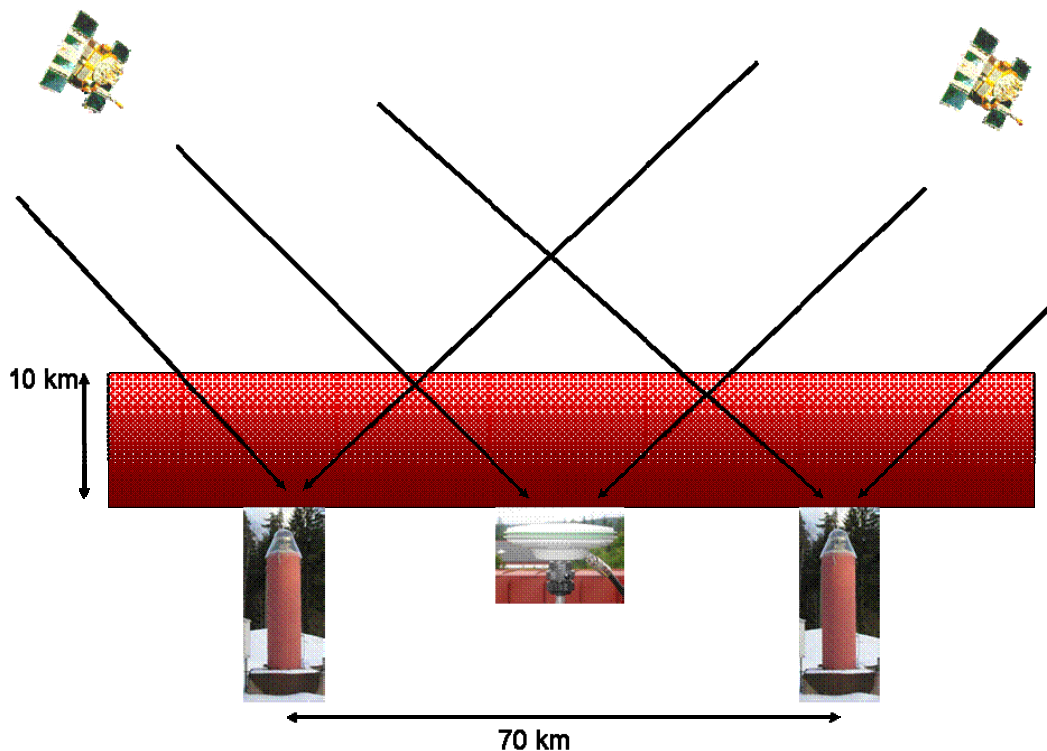[e.g., *Treuhaft and Lanyi*, 1987, *Jarlemark*, 1997, *Nilsson*, 2007]

Figure 13   **Observational geometry for the troposphere.**

The constant *C* changes with time with grater values during summer conditions. In this study, we choose α=0.9 according to *Nilsson* [2007]. And the statistics of *C* is taken from *Treuhaft and Lanyi*, [1987] and *Jarlemark* [1997]. We have chosen the *C* values for $5.57 \cdot 10^{-9}$ m$^{1.1}$, $6.18 \cdot 10^{-10}$ m$^{1.1}$, and $1.55 \cdot 10^{-8}$ m$^{1.1}$ respectively representing the nominal situation, the lower 5% and the upper 95%. Using these values and the equations 12 and 13, we can calculate the expected zenith wet delay errors when using a single reference station. Figure 14 shows these errors as a function of distance between the reference and rover locations. The solid line in the figure represent the nominal situation and the shaded area represents the expected delay error within 5 - 95% of the time.

For network-RTK the influence is reduced by the interpolation of the measurements at the reference sites. Using different weights in the interpolation results in varying sizes of the tropospheric influence on the errors. Figure 15 shows the resulting expected error for the standard network constellation, described in Figure 5, and a nominal troposphere error contribution. In the figure the choice of weights as described in the previous chapter is marked as "Our Choice". We can also see the results when choosing equal weights on all six reference stations and by using the inner triangle only.
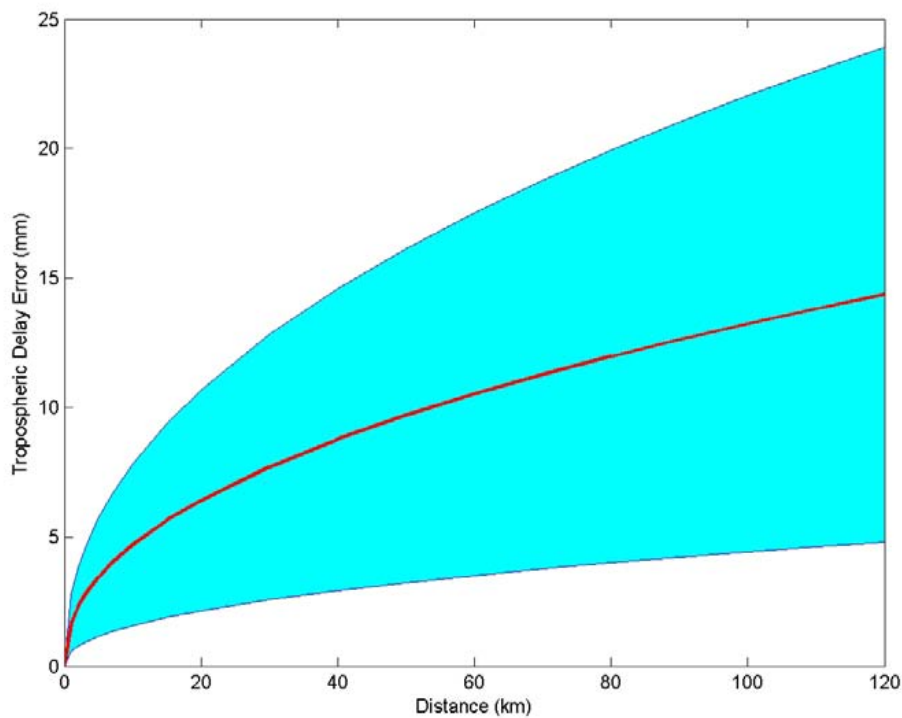

Figure 14   **Tropospheric delay error in zenith, as a function of distance between reference station and rover. The solid line represent the nominal situation and the shaded area represents the expected delay error within 5 - 95% of the time.**
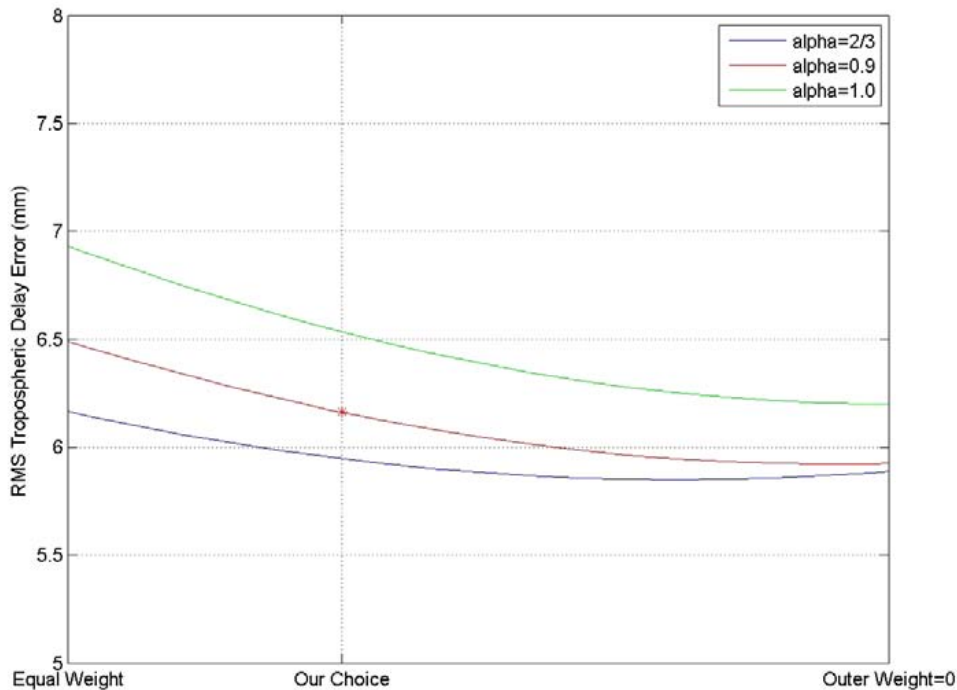
Figure 15   **Tropospheric delay error as a function of the weighting of the reference stations. The three curves represents three values on the parameter α**

Similarly to this analysis, we can perform interpolation based on the 5% and 95% situations. Table 2 shows the resulting tropospheric effects on the range interpolation errors.

Table 2 Tropospheric effect on range interpolation error

	Nominal	5%	95%
Interpolation Error (mm)	6.2	2.1	10.3

The mapping function to a satellite at lower elevation angles is not perfectly linear with geography(latitude and longitude). A systematic second order effect mainly due to the curvature of the earth remains after a linear interpolation as is performed in network-RTK. However, if an a priori atmosphere with a proper mapping function is subtracted from the reference stations observations (and later added to back to the virtual reference station), we can treat the troposphere statistical as linear mapping. See Appendix I for a more thorough derivation of the troposphere error contribution.

2.2.7   Antenna

In order to develop models for the local environmental effects on the network-RTK estimates of vertical and horizontal positions, we setup two experiments. These two experiments was designed to estimate the local environmental effects in two very different environments. A Leica AX1202 GG antenna was used as rover antenna in both cases. Figure 16 shows the setup for the experiment for the characterization of signal multipath in a relatively noise free environment. Figure 17 shows the setup for the characterization of signal multipath in a difficult environment. The residuals are shown in Figure 20. Both the locations used for the experiment are relatively close, i.e., within 50 m, to a reference antenna at a well determined position. Based on the relative measurements to these reference sites, we can, by removing the known distance between

the antennas and by assuming the troposphere and ionosphere contribution are identical due to the relative closeness of the antennas, determine the contribution from the local environment. Figure 18, Figure 19, and Figure 20 shows the remaining variations, i.e., the residuals, in the received phase after removing the known effects. The figures show the variations in L1 for the less noisy environment, L2 for the less noisy environment, and L1 for the noisy environment respectively. The size of these residuals are much greater for the noisy environment, especially for elevation angles up to 50°.

Figure 21 shows the rms of the residuals for the measurements between a Leica AX1202 GG antenna as a rover and a Dorne Margolin choke ring antenna as a reference antenna. The figure shows the local environmental effects when using a rover in a relatively noise free environment. The three different curves shows the results for L1 (blue), L2 (red), and L3 (black) respectively. Figure 22 shows the rms of the residuals for measurements between two Dorne Margolin choke ring antenna. This measurement is necessary in order to separate the noise contributions from the rover and reference antennas.

Figure 23 shows the model fit to the measurements of the rms of the residuals of measurements between the Leica AX1202 GG and Dorne Margolin antennas. Curves have been fitted to the L1 and L2 residuals. The function we used is *a/sin(elevation)*, where we estimated the parameter *a*. The values for *a* is 2.4 for L1 data and 2.9 for L2 data. Performing the same procedure for the measurements between the two Dorne Margolin antennas, we can estimate the parameters *a* for this setup as well.

Figure 16   **Antenna setup for the characterization of signal multipath in a relatively noise free environment.**

Figure 17   **Antenna setup for the characterization of signal multipath in a difficult environment.**
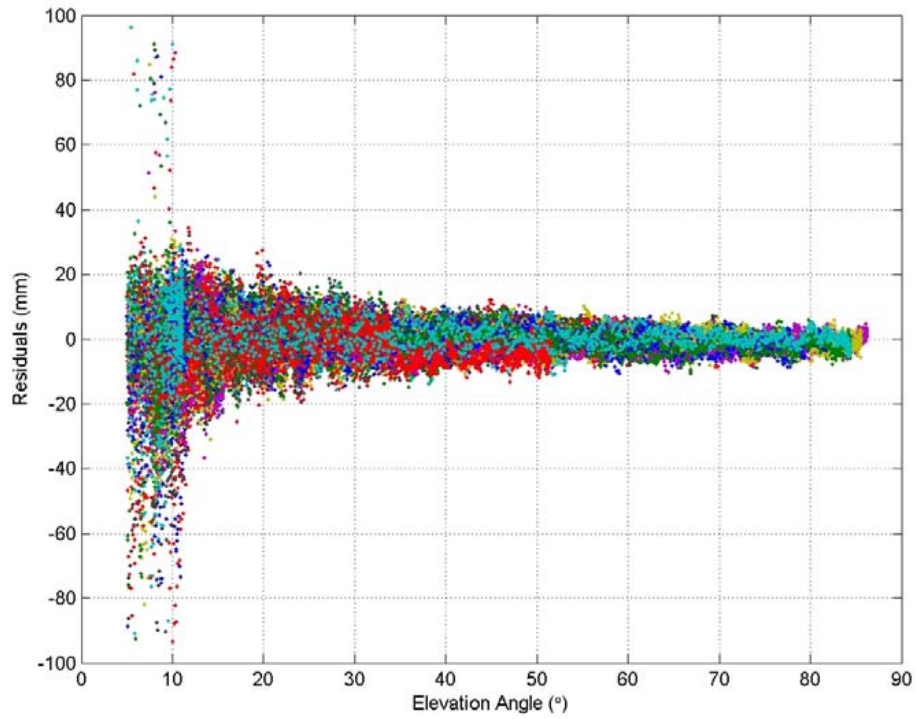
Figure 18   **Residuals for L1 phase observables. A Leica AX1202 GG antenna was used in a relatively noise free environment.**
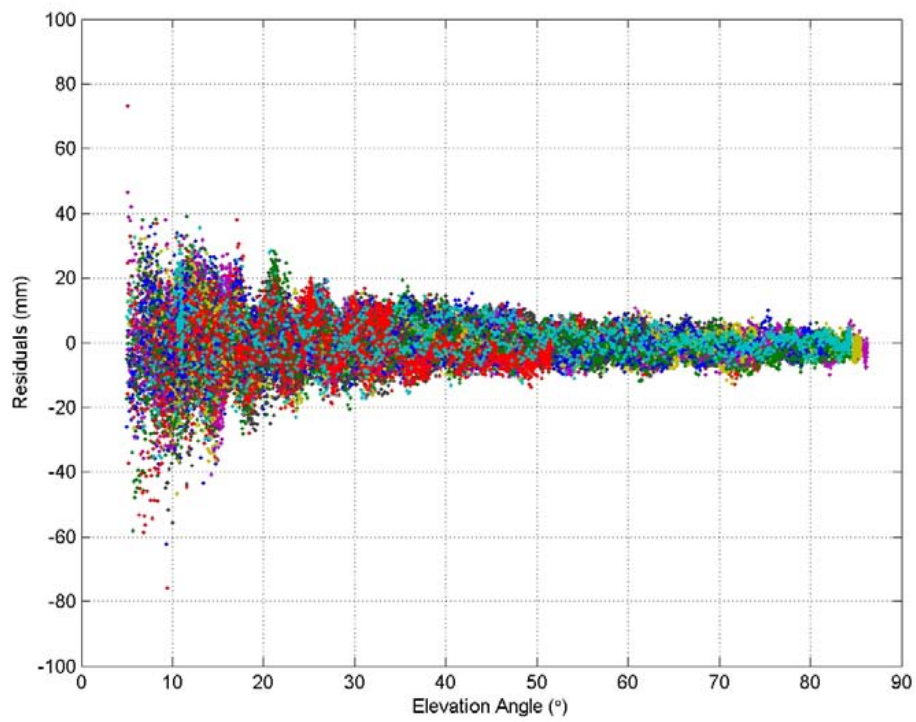
Figure 19   **Residuals for L2 phase observables. A Leica AX1202 GG antenna was used in a relatively noise free environment.**
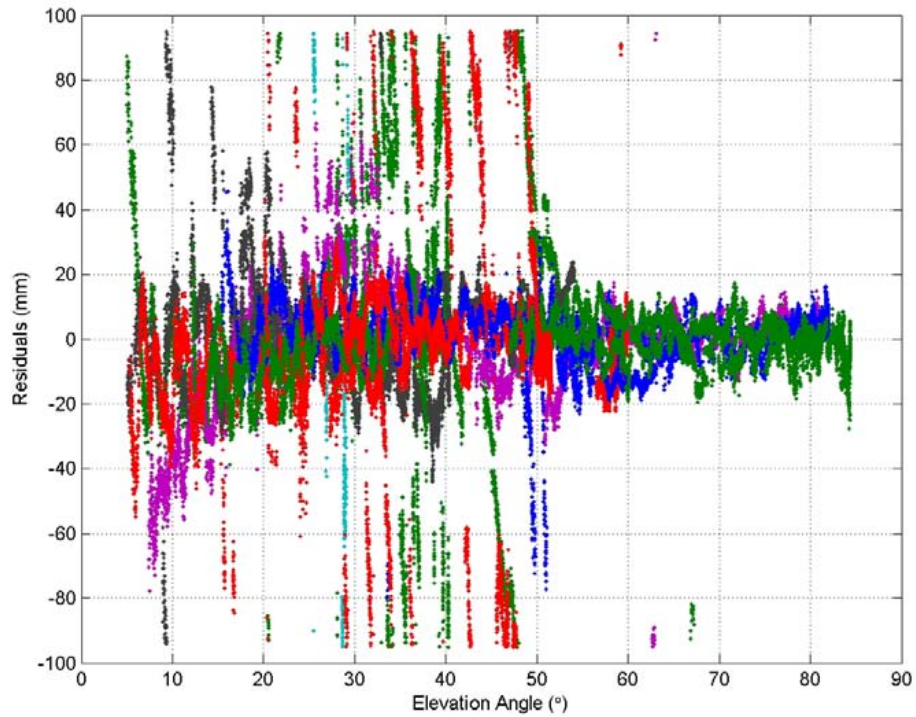
Figure 20 **Residuals for L1 phase observables for the difficult conditions. A Leica AX1202 GG antenna was used.**
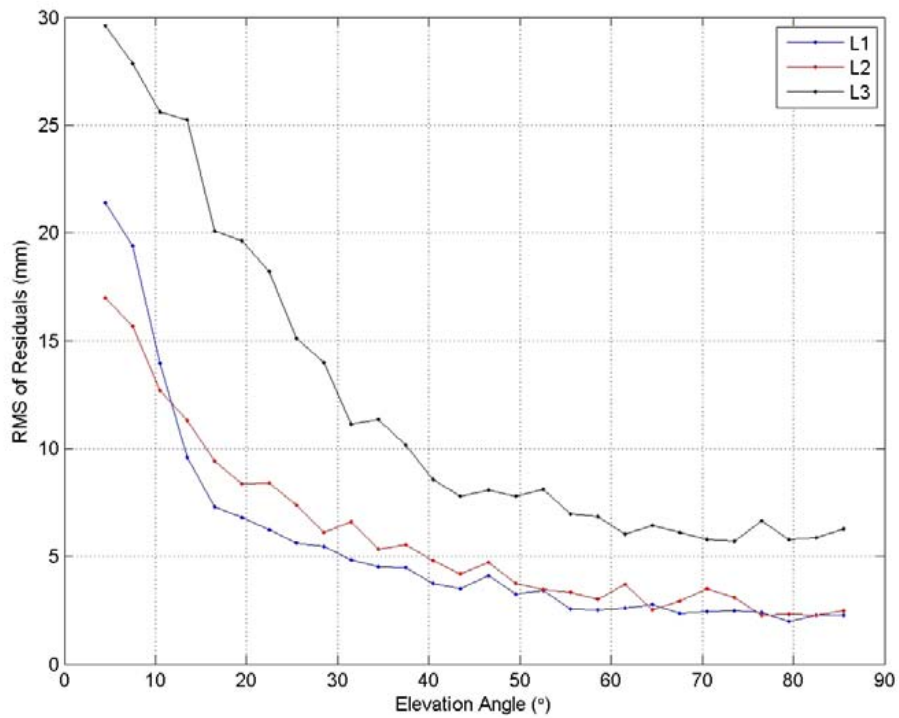
Figure 21 **RMS of the residuals for the local environmental effects for the rover for the relatively noise free environment. The three different curves shows the results for L1 (blue), L2(red), and L3(black) respectively.**
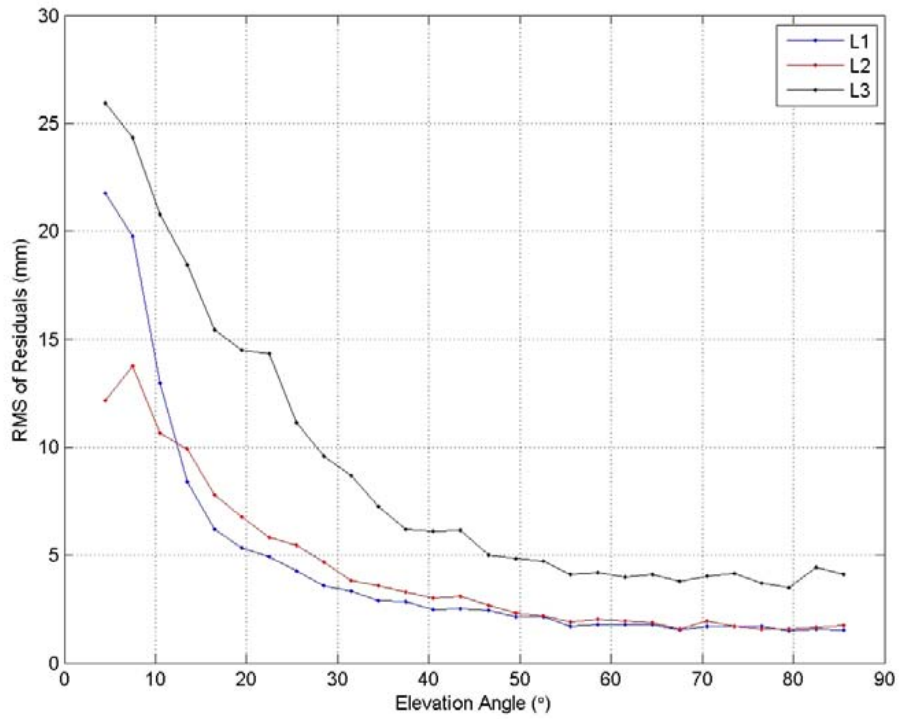
Figure 22 RMS of the residuals for the local environmental effects for the reference station for the relatively noise free environment. The three different curves shows the results for L1 (blue), L2(red), and L3(black) respectively.
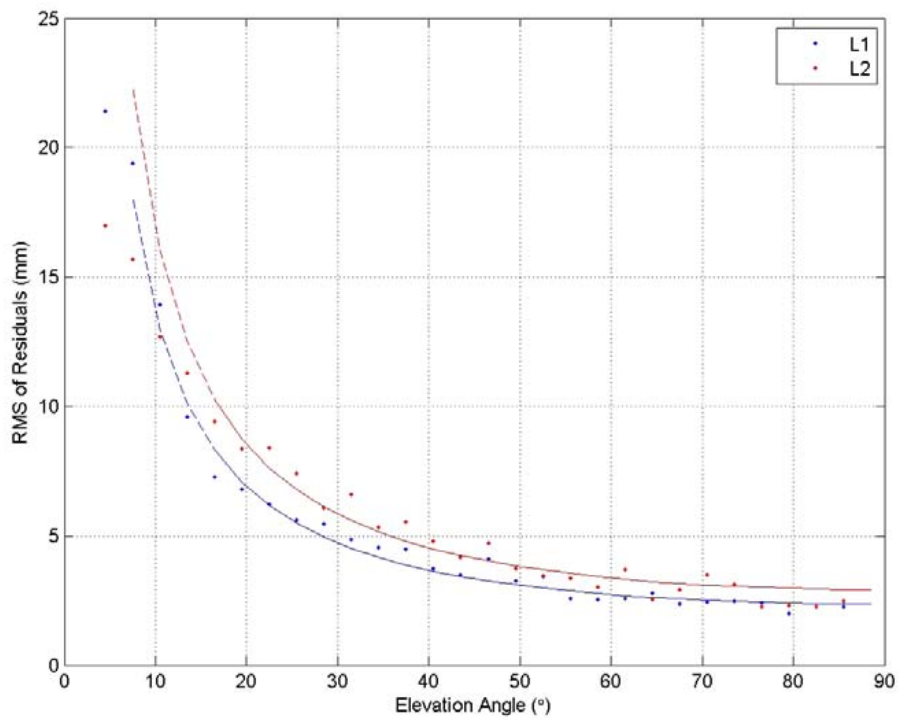
Figure 23 Model fitted to the residuals of the local environmental effects.

Figure 24 shows the auto correlation of the local environmental effects for L1 and L2 respectively using the data in Figure 18 and Figure 19. It can be seen in the figure that each curve consist of two components. One white noise component visible at zero time lag representing the instrumental measurement noise and one slowly decaying curve representing the signal interference due to the environment. In the figure are also models fitted to these data points.
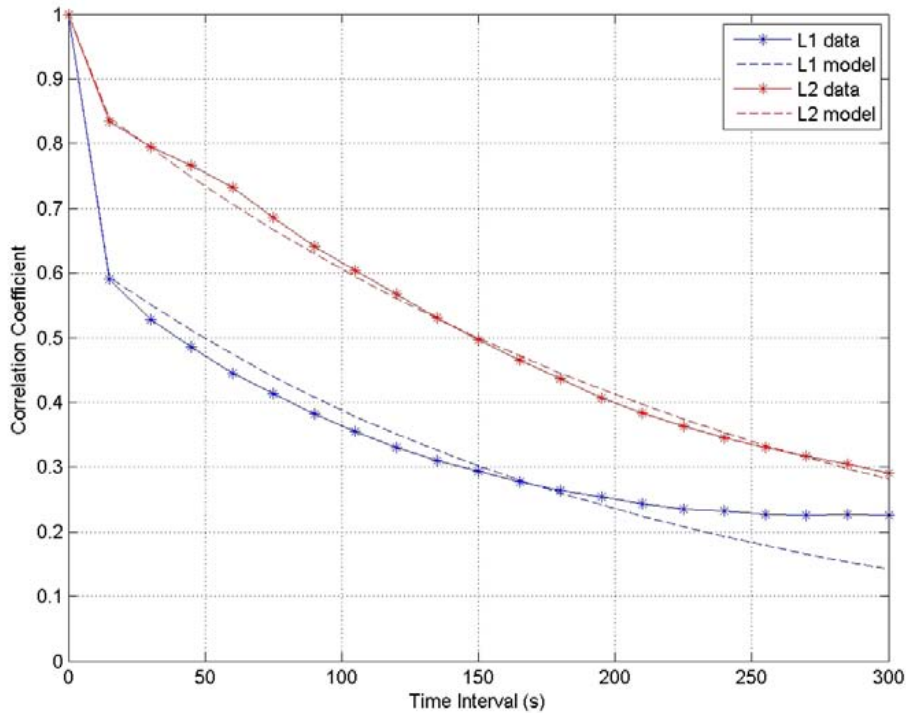
Figure 24   Auto correlation of receiver noise and local environmental signal effects for L1(blue) and L2(red). In the figure are also models fitted to these data points.

Based on the analysis described above, we have estimated the error contribution from local effects. These are based on the fit to the rms of the residuals for the measurements between the different antenna types. For the measurement between the Leica AX1202 GG and Dorne Margolin antennas, which we hereafter refer to as between a rover and reference antenna, we found parameter values of 2.4 and 2.9 for L1 and L2 respectively. Similarly, we found values for the measurements between two Dorne Margolin antennas, which we hereafter refer to as between two reference antennas. These values are summarized in Table 3. Based on these numbers, we can estimate the contribution from the single reference and rover antennas assuming that the contributions from the reference stations and rover are uncorrelated.

Table 3 Error contribution to the phase observables from the local effects on L1 and L2 respectively.

Setup	L1 (mm)	L2 (mm)
rover-ref	2.4	2.9
ref-ref	1.7	2.1
single ref	1.2	1.5
single rover	2.0	2.5

A linear combination, L_a, formed in order to reduce the local antenna and environmental effects can be written as [*Emardson and Jarlemark,* 2009]

$$L_a = 0.61 L_1 + 0.39 L_2 \qquad (14)$$

The weighting of the observables L1 and L2 are chosen so that this combined observable L_a can be useful when the contribution from the ionosphere is relatively small and the local effects are relatively large.

2.2.8 Summary

We can now summarize and quantify the different error sources affecting the quality of network-RTK measurements. Table 4 summarises the results given in Table 1, Table 2, Table 3. These results are based on the contribution from the different error sources on the measured phase in the zenith direction.

Table 4 Summary of the contribution from different error sources. The table specifies the errors in interpolated phase values for an equivalent zenith direction.

Error source		Error Nominal (mm)	Error 5% (mm)	Error 95% (mm)
Satellite clocks		0	0	0
Satellite orbits		0	0	0
Ionosphere		7.2	2.0	16.3
Troposphere		6.2	2.1	10.3
Local effects	Rover	2.0	1.2	4.0
	Reference	1.2	1.2	1.2

The different error sources described in the previous sections will affect the vertical and horizontal position estimates as the differenced phase errors will map into different vertical and horizontal positions errors depending on primarily their elevation dependence. In order to determine how much the different error sources contribute to the position errors we use the model

$$z = Hx + v$$

Here the vector z contains the measurement errors from Table 4. This vector can be formed as different combinations of the observables at the L1 and L2 frequencies. In this report, we have used L1 only for the basic scenario. We have also used the combinations L3 and La from (10) and (14) respectively. The vector x contains the parameters we want to estimate. These are three dimensional rover position e_E, e_N, e_V, and a receiver clock offset l_o. The matrix H contains the partial derivatives matching the estimates with the measurement errors. H depend primarily on the satellite constellation used. In this study, we have used a satellite constellation based on GPS and GLONASS during two weeks, from GPS week 1491 and 1492. This is the time period from August 3, 2008 to August 16, 2008. We have processed the data with 1 minutes interval except for the troposphere that we update once per hour. We have used an elevation cutoff angle of 13° and the observations are weighted with $w=sin(elevation)$. Using this weighting, we form W as a diagonal matrix with values w on the diagonal. Using this modelling, we could generate random errors based on the statistically representation of the errors given in Table 4. We have chosen, however, to calculate the errors in the estimated parameters as:

$$Cov(\hat{x}) = \left(H^T W H\right)^{-1} H^T W \cdot Cov(z) \cdot W^T H \left(H^T W H\right) \qquad (15)$$

Table 5 and Table 6 shows the vertical and horizontal errors respectively as we can expect statistically from equation 15. In the tables below, we have specified the different contributions from the different error sources described earlier. Each table also contains values for a nominal situation, one column containing values for a situation when contributions are relatively small and one column with values when the contributions are relatively large. The latter corresponds to approximately an upper 95% level. The probability that all error sources are on the 5% or at the 95% level at the same time is very low. Hence, we have not specified any summation of those values in order not to give the impression that the situation is worse than it actually is.

In addition to the sizes of the contribution from the different error sources to the estimated parameters, we also in the table specify the de-correlation times of the different error sources. The de-correlation times are estimated by modelling the autocorrelation of each error source

$$A(\tau) = E\left[\varphi_D(t+\tau)\varphi_D(t)\right] \tag{16}$$

as

$$A(\tau) = A_0 e^{-\tau/t_c} \tag{17}$$

In the table we specify estimates of the values t_C for the different error sources. For the local effects, we have specified two different values 0 and 260 seconds. These represents the receiver noise part and the multipath part respectively.

Table 5   **Vertical error**

Error source		Error Nominal situation(mm)	Error 5% (mm)	Error 95% (mm)	Time (s)
Satellite clocks		0	0	0	
Satellite orbits		0	0	0	
Ionosphere		16.6	4.5	37.4	1000
Troposphere		20.9	7.0	34.9	6700
Local Effects	Rover	5.6	3.3	11.1	0/260
	Reference sites	1.4	1.4	1.4	0/260
Total (rms)		27.3	-	-	-

Table 6   **Horizontal error**

Error source		Error Nominal situation(mm)	Error 5% (mm)	Error 95% (mm)	Time (s)
Satellite clocks		0	0	0	
Satellite orbits		0	0	0	
Ionosphere		10.7	2.9	24.2	1000
Troposphere		3.9	1.3	6.5	6700
Local Effects	Rover	3.5	2.1	7.0	0/260
	Reference sites	0.9	0.9	0.9	0/260
Total (rms)		12.0	-	-	-

2.3 Comparison between measurements and simulation

2.3.1 Measurement setup

In order to evaluate the simulations, we compare those with measurements with state-of-the art RTK equipment using the SWEPOS® Network RTK service. Here Trimble R8 was used. In the measurement setup, a rover was positioned at a point with a well determined position, a so called SWEREF point. The horizontal mask was good allowing for observations down to low elevation angles. The rover used an elevation cutoff angle of 13 degrees in the processing using both GPS and GLONASS observations. Measured coordinates were collected during 24 hours, with coordinate estimates every 15 seconds. The experiment was repeated for two different locations for the rover. We used the site 128746, and site 147138 for rover position. We refer to these as rover 1 and rover 2 respectively. Figure 25 shows the positions of the rovers and the reference stations.

Figure 25   **Illustration of the locations of the two rovers and the corresponding reference stations used in network-RTK.**

Rover 1

Rover 1 was located at the location 127378, see Figure 25. Measurements were conducted during 24 hours starting the 18 of October 2008 with one estimated coordinate every 15 seconds. The mean distance between the reference stations in an inner triangle is approximately 43 km. The mean vertical TEC during the 24 hours was 4.5 TECU. Analysis of data from one location in northern Sweden (Vilhelmina) and one in the southern part (Hässleholm) for the days 18-19 October gave a troposphere variability That was 12% greater than the nominal value. This was applied to the troposphere values in the simulations. For the measurements, we calculated the measurement errors as the difference between the estimated and the known position. Figure 26 and Figure 27 show the vertical and horizontal measurement errors during the 24 hour long measurement period.
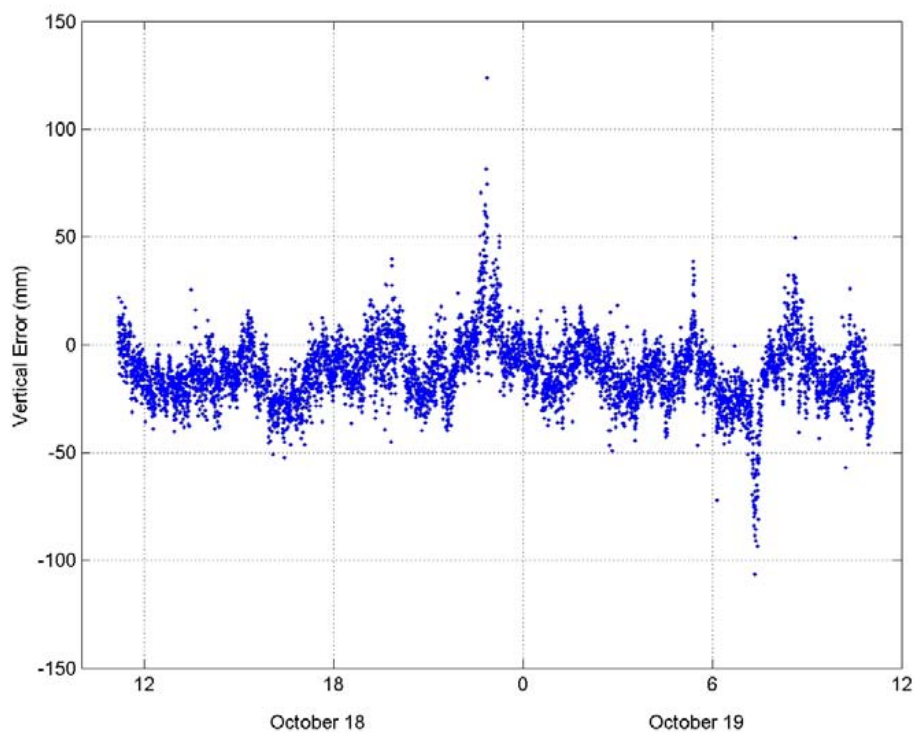

Figure 26   **Vertical measurement errors during the 24 hour for rover 1.**
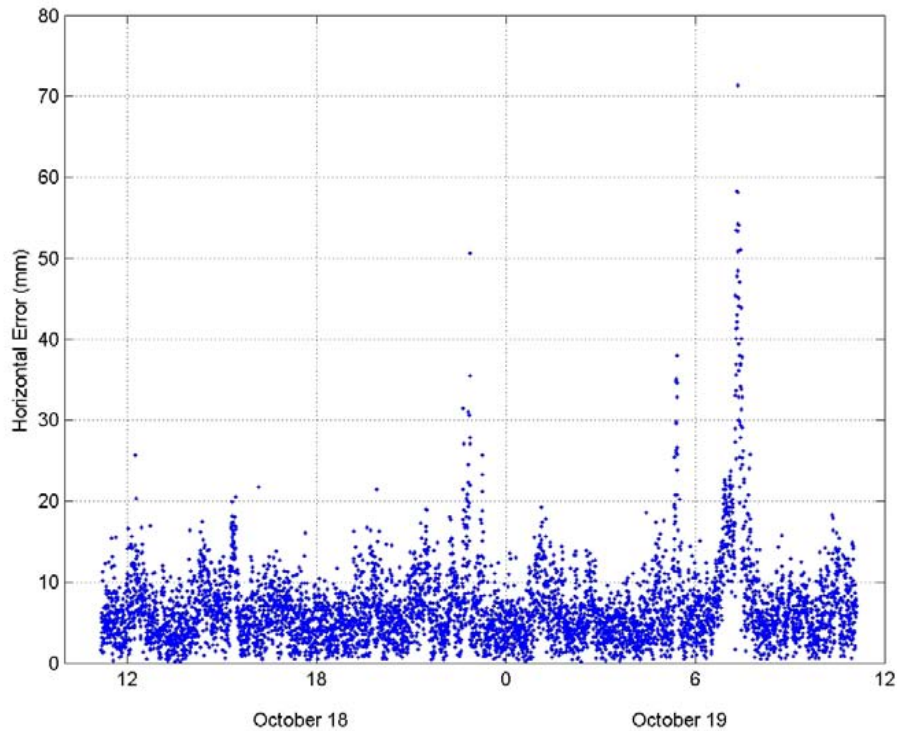
Figure 27   Horizontal measurement errors during the 24 hour for rover 1.

Table 7 shows the measured and simulated vertical and horizontal errors for rover 1. The simulated results are slightly lower than the measured for the vertical component 17.8 mm compared to 19.3 mm. For the horizontal errors, the measured errors are slightly larger 8.6 mm compared to 6.6 for the simulated.

Table 7 Measured and simulated vertical and horizontal errors for rover 1.

Error source		Measured(mm)	Simulated(mm)	Measured(mm)	Simulated(mm)
		Vertical		Horizontal	
Satellite clocks		-	0	-	
Satellite orbits		-	0	-	
Ionosphere		-	5.3	-	3.4
Troposphere		-	15.9	-	4.2
Local Effects	Rover	-	5.6	-	3.5
	Reference sites	-	1.9	-	1.2
			-		
Total (rms)		19.3	17.8	8.6	6.6

Rover 2

Rover 2 was located at the location 147138, see the map Figure. Measurements were conducted during approximately 24 hours during the 10 and 11 of February 2009. The mean distance between the reference stations in an inner triangle is approximately 75 km. The mean vertical TEC during the 24 hours was 4.0 TECU. We assumed a troposphere variability that corresponds to the 5% lower value as specified in Table 4. This value was applied to the troposphere values in the simulations. Figure 28 and Figure 29 show the vertical and horizontal measurement errors during the measurement period.
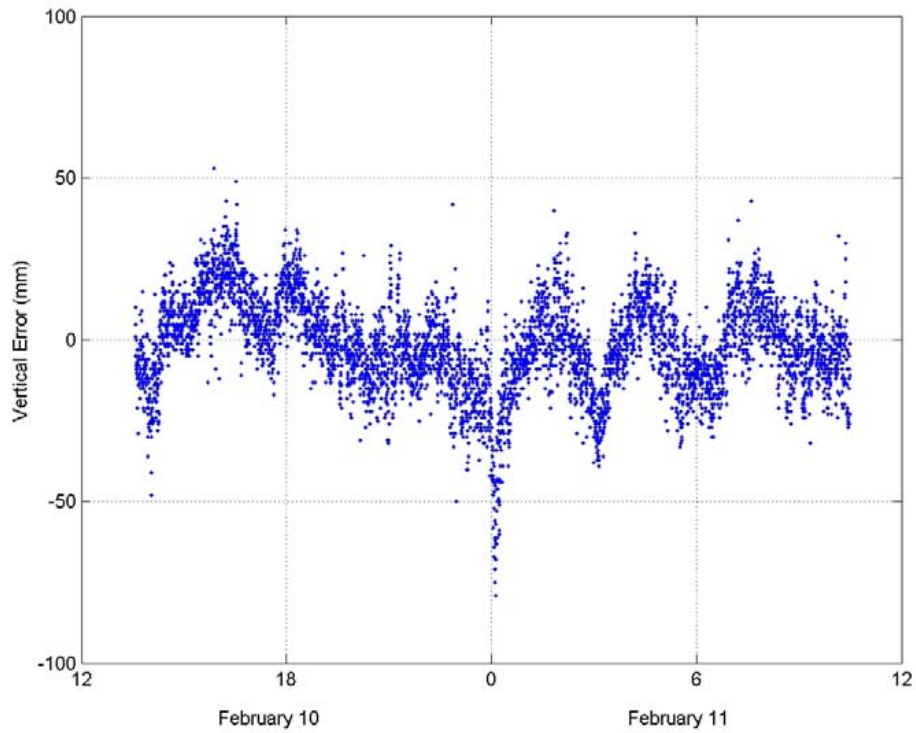
Figure 28   **Vertical measurement errors during the measurement period for rover 2.**
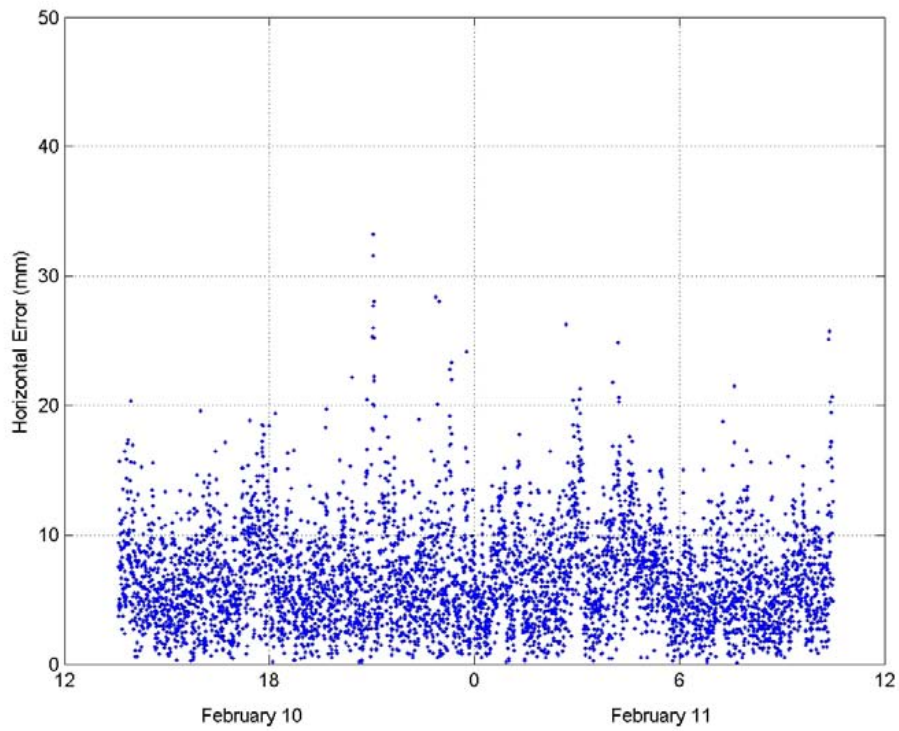

Figure 29   **Horizontal measurement errors during the measurement period for rover 2.**

Table 8 shows the measured and simulated vertical and horizontal errors for rover 2. The measured results are clearly higher than the simulated for the vertical component 14.3

mm compared to 9.6 mm. This can partly be due to high variability in the troposphere during the 24-hour measurement period compared to the chosen value for the simulations. The contribution from the troposphere is 5.9 mm in the simulation. The actual measurements were taken during parts of the 24-hour period and the variability during this period may have been higher. For the horizontal errors, the measured errors are slightly larger 7.6 mm compared to 5.0 for the simulated.

Table 8 Measured and simulated vertical and horizontal errors for rover 2.

Error source		Measured(mm)	Simulated(mm)	Measured(mm)	Simulated(mm)
		Vertical		Horizontal	
Satellite clocks		-	0	-	
Satellite orbits		-	0	-	
Ionosphere		-	4.8	-	3.1
Troposphere		-	5.9	-	1.3
Local Effects	Rover	-	5.6	-	3.5
	Reference sites	-	1.7	-	1.1
			-		
Total (rms)		14.3	9.6	7.6	5.0

It is important to note that the simulations are in no way modified to agree with the results from the measurements described above.

3   **Work Package 2**

Work package 2 deals with the future quality of network-RTK. In the first section, we investigate the future quality under the assumption that the reference network is kept without changes compared to the current situation. The improvements seen in the position estimate errors are due to the increased amount of satellites available when the systems currently under development are deployed. In the second section, we take into account in addition to the development of new GNSS systems also possible changes in the network infrastructure. The availability of observations from these new satellite systems will heavily affect the number of visible satellites above different elevation angles. In section 3.2 we can see the results of this increased amount of possible observations. Below, we will refer to the current constellation as the constellation of GPS and GLONASS during the fall 2008 and the future constellation as the full constellation of GPS, GLONASS, Galileo, and Compass.
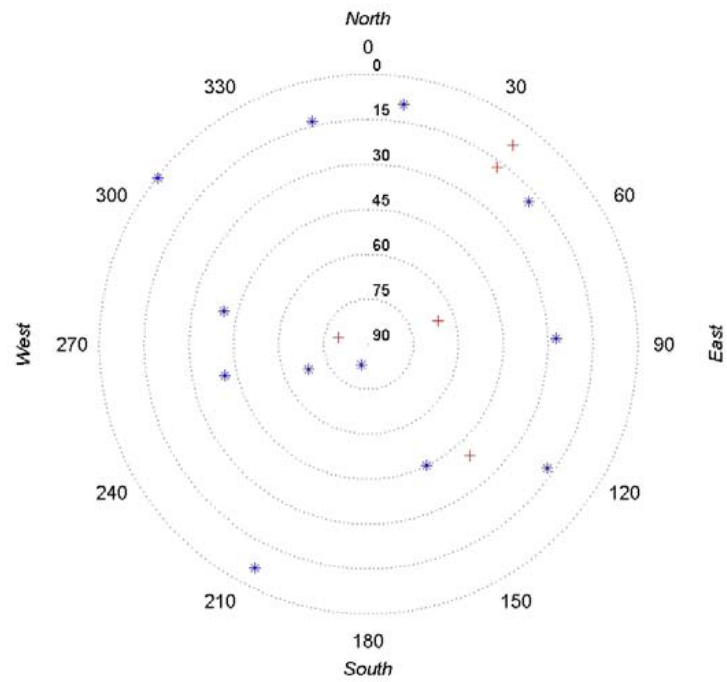
Figure 30 **Skyplot for observed GPS (blue stars) and GLONASS (red plus signs) satellites using the constellation during the fall 2008.**
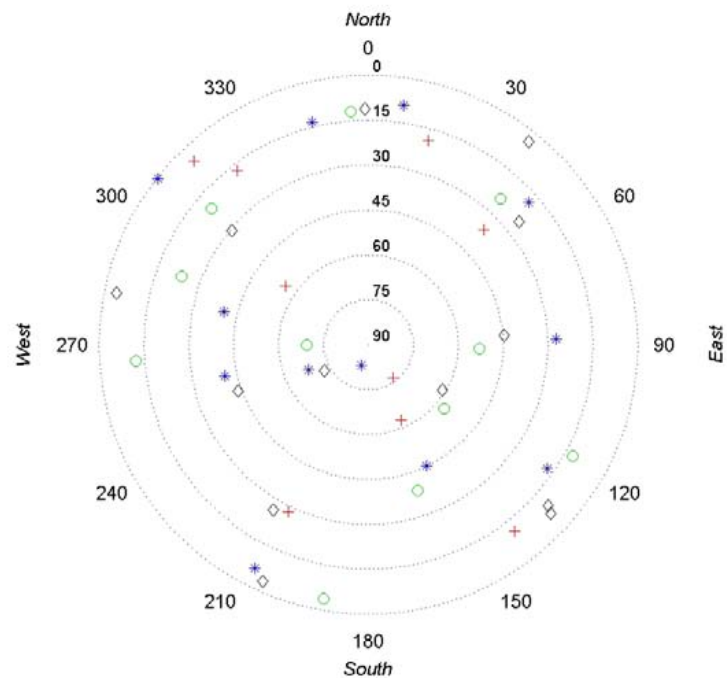
Figure 31 **Skyplot for observed GPS (blue stars), GLONASS (red plus signs) Galileo() and Compass() satellites a future.**
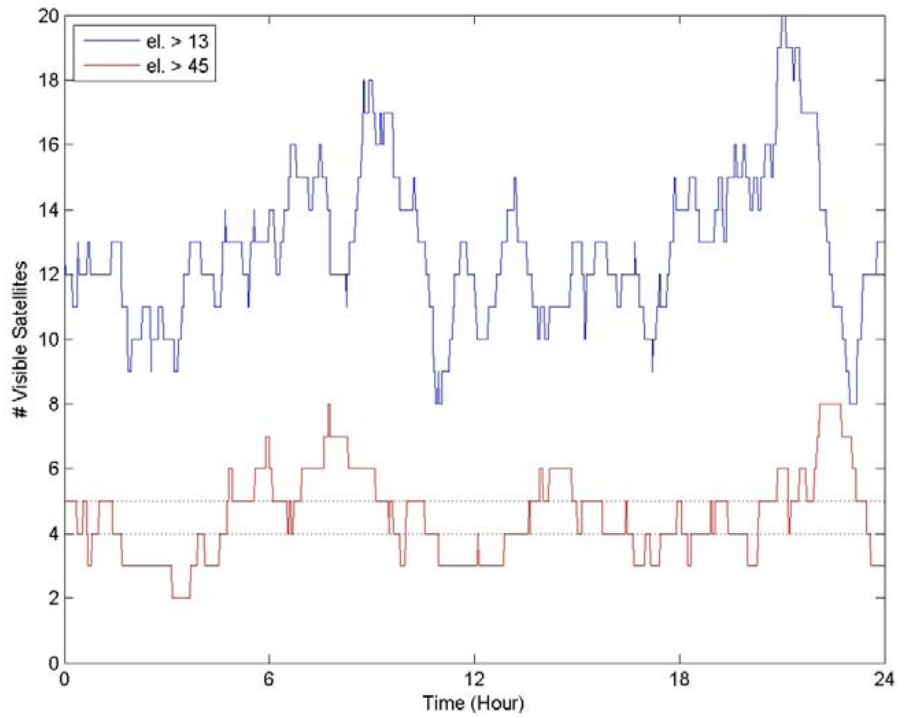
Figure 32   **Number of visible satellites during 24 hours using the GPS and GLONASS constellations of the fall 2008 with an elevation cutoff angle of 13 degrees (blue) and 45 degrees (red) respectively.**
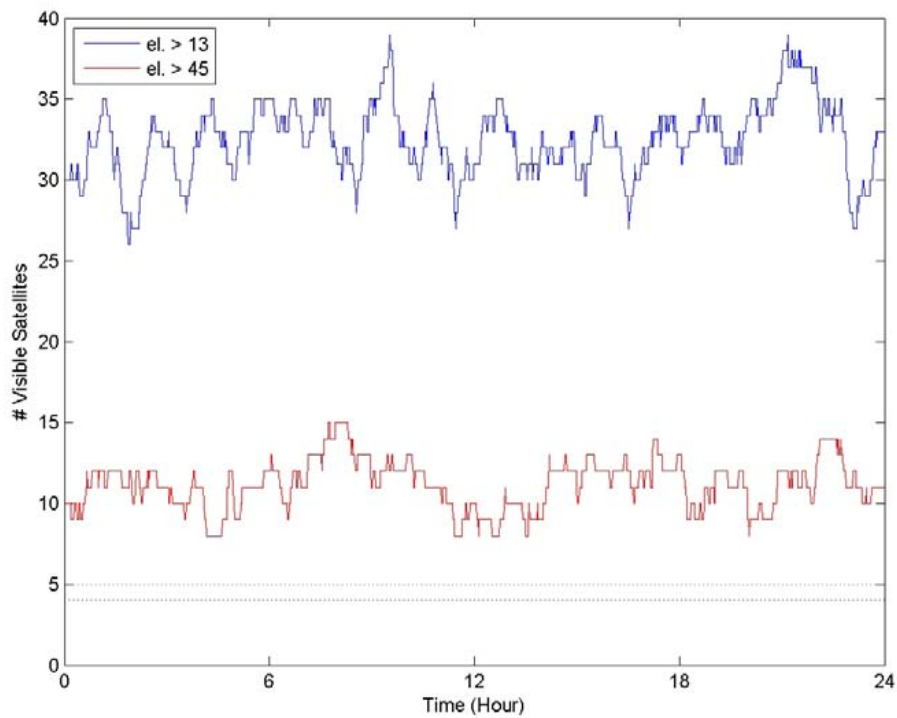
Figure 33   **Number of visible satellites during 24 hours using the future constellations of GPS, GLONASS, Galileo, and Compass with an elevation cutoff angle of 13 degrees (blue) and 45 degrees (red) respectively.**

3.1 Future quality using the current Swedish infrastructure

In this work we investigate the future quality under the assumption that the reference network is kept without changes compared to the current situation. We assume that there exist full constellations for the systems GPS, GLONASS, Galileo, and Beijdou/Compass. Table 9 shows the vertical and horizontal errors for the current and a future satellite constellation. The values for the current constellation are identical to those presented in Table 5 and Table 6.

Table 9   **Vertical and horizontal errors for the current and a future satellite constellation.**

Error source		Vertical Error (mm)		Horizontal Error (mm)	
		Current	Future	Current	Future
Ionosphere		16.6	9.3	10.7	6.2
Troposphere		20.9	20.8	3.9	3.8
Local Effects	Rover	5.6	3.2	3.5	2.1
	Reference sites	1.4	0.8	0.9	0.5
Total (rms)		27.3	23.0	12.0	7.5

Figure 34 shows the errors for the vertical and horizontal coordinates using the currents and future satellite constellation. The RMS error decreases when more observations are available. The decrease, however, is not more than typically 5 mm in both the vertical and horizontal component. It is noticeable that for the current constellation the minimum for the vertical error occurs for an elevation cutoff angle of approximately 15 degrees, which is relatively close to the cutoff angle of 13 degrees which is a standard for RTK-processing. For the future constellation, however, the minimum for the vertical error occurs for an elevation cutoff angle of approximately 25 degrees. For the horizontal component the error is not as dependent on elevation cutoff angle, especially not for the future constellation. In more detail the minimum is found for the four curves at 8, 13, 16, and 23 degrees respectively for the horizontal component and current constellation, the horizontal component and future constellation, the vertical component and current constellation, and the vertical component and future constellation.
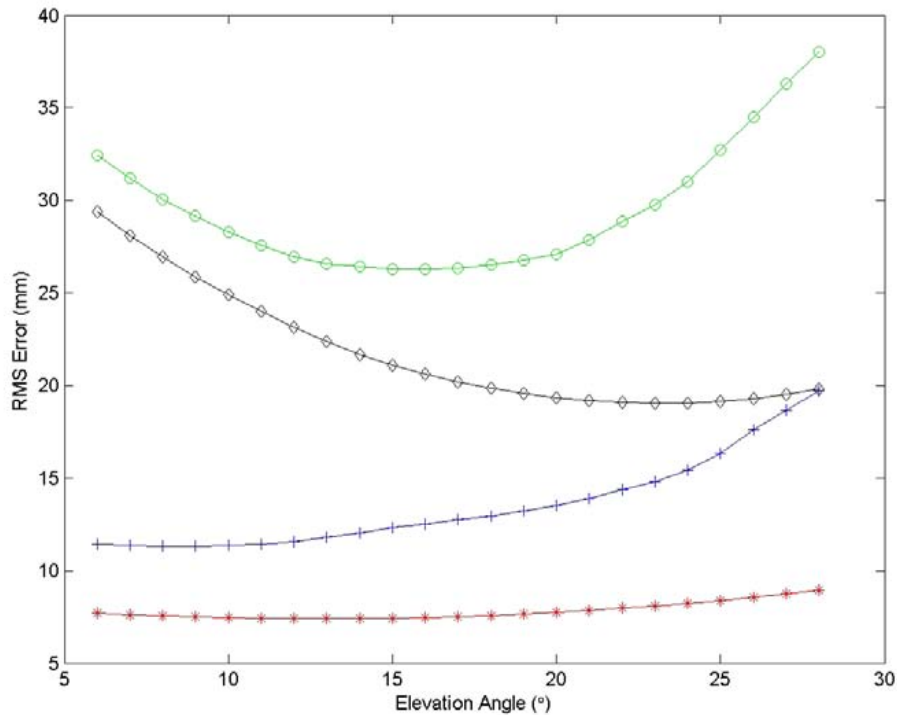
Figure 34 **RMS error as a function of elevation angle for the vertical and horizontal components. The curves represent from the top: vertical coordinate error using the current satellite constellation (green circles), vertical coordinate error using a future satellite constellation (black triangles), horizontal coordinate error using the current satellite constellation (blue plus signs), and horizontal coordinate error using a future satellite constellation (red stars).**

Based on the elevation cutoff studies, we can re-compute the contribution from the different error sources for the future constellation given that we use the elevation angle of 24 degrees instead of that of 13 degrees. Table 10 shows the results for the current and future constellation.

Table 10 **Vertical and horizontal errors for the current and a future satellite constellation. The results for the future constellation is based on an elevation cutoff angle of 24 degrees. The results for the current constellation is based on an elevation cutoff angle of 13 degrees.**

Error source		Vertical Error (mm)		Horizontal Error (mm)	
		Current	Future	Current	Future
Ionosphere		16.6	13.0	10.7	7.6
Troposphere		20.9	14.3	3.9	2.7
Local Effects	Rover	5.6	3.9	3.5	2.3
	Reference sites	1.4	1.0	0.9	0.6
Total (rms)		27.3	19.7	12.0	8.4

3.1.1 L3 processing

For longer distances, it may be preferable to use the L3 combination instead of L1 for the positioning as described in section 2.2.5. Figure 35 shows the errors for the vertical and horizontal coordinates using the currents and future satellite constellation using L3 combinations. The result is similar to that of L1 in Figure 34 with higher optimal values for the cutoff angle for the future constellation than for that of the current constellation.
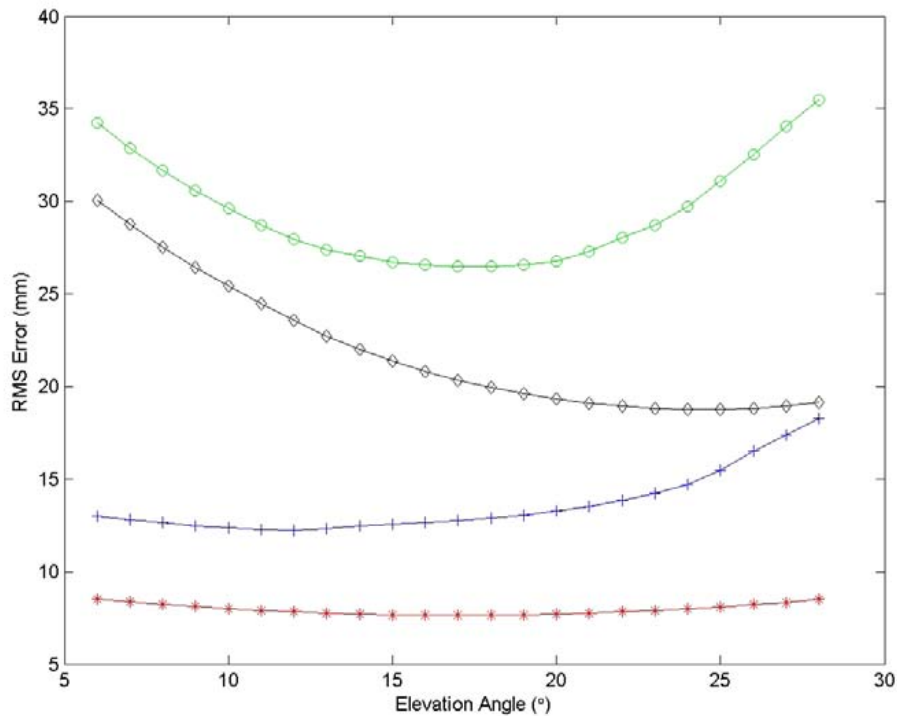

Figure 35   RMS error as a function of elevation angle for the vertical and horizontal components. All results are produced with the L3 combination. The curves represent from the top: vertical coordinate error using the current satellite constellation (green circles), vertical coordinate error using a future satellite constellation (black triangles), horizontal coordinate error using the current satellite constellation (blue plus signs), and horizontal coordinate error using a future satellite constellation (red stars).

Table 11 shows the vertical and horizontal errors for L1 compared to L3 processing using the current constellation and the currently used cutoff angle of 13 degrees. The results using the different observables are similar in total rms error both for the vertical and horizontal components. For the L3 processing, the ionosphere contribution is zero. On the other hand the contribution from the local effects is significantly larger than those for the L1 processing. Hence, for this nominal setup, the use of the L3 combination compared to L1 does not reduce the uncertainty. This setup, however, includes a standard ionosphere variability. For times with a high spatial variability in the ionosphere, on the other hand, the L3 combination will be preferable. See for example the ionosphere contribution in Table 5. Table 11 shows the vertical and horizontal errors for current constellation compared to the future constellation using the currently used cutoff angle of 13 and 24 degrees respectively and the L3 observable.

Table 11   **Vertical and horizontal errors for L1 compared to L3 processing using the current constellation and the currently used cutoff angle of 13 degrees.**

Error source		Vertical Error (mm)		Horizontal Error (mm)	
		L1	L3	L1	L3
Ionosphere		16.6	0.0	10.7	0.0
Troposphere		20.9	20.9	3.9	3.9
Local Effects	Rover	5.6	17.8	3.5	11.2
	Reference sites	1.4	4.6	0.9	2.9
Total (rms)		27.3	27.8	12.0	12.2

Table 12   **Vertical and horizontal errors for current constellation compared to the future constellation using the currently used cutoff angle of 13 and 24 degrees respectively and the L3 observable.**

Error source		Vertical Error (mm)		Horizontal Error (mm)	
		Current	Future	Current	Future
Ionosphere		0.0	0.0	0.0	0.0
Troposphere		20.9	14.3	3.9	2.7
Local Effects	Rover	17.8	12.4	11.2	7.2
	Reference sites	4.6	3.2	2.9	1.9
Total (rms)		27.8	19.2	12.2	7.9

3.1.2   La processing

In some cases, it may be preferable to use the La combination as described in 2.2.7 instead of L1 for the positioning. This combination can be useful for periods with low spatial variability in the ionosphere or difficult local environments. Figure 36 shows the errors for the vertical and horizontal coordinates using the currents and future satellite constellation using the La combinations. The result is similar to that of L1 in Figure 34 and L3 in Figure 35 with higher optimal values for the cutoff angle for the future constellation than for that of the current constellation.
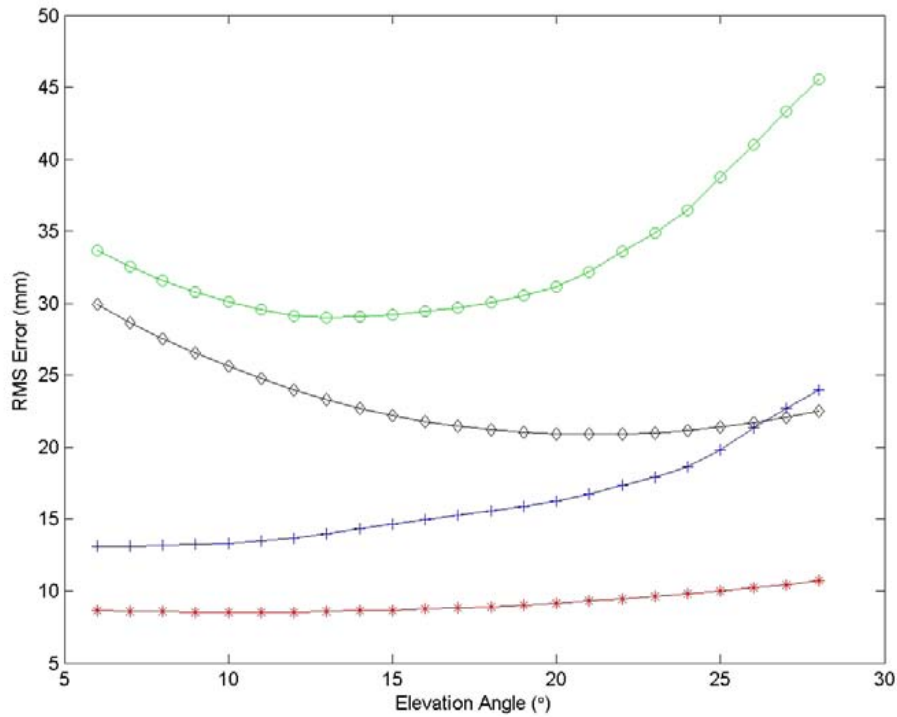
Figure 36 **RMS error as a function of elevation angle for the vertical and horizontal components. All results are produced with the La combination. The curves represent from the top: vertical coordinate error using the current satellite constellation (green circles), vertical coordinate error using a future satellite constellation (black triangles), horizontal coordinate error using the current satellite constellation (blue plus signs), and horizontal coordinate error using a future satellite constellation (red stars).**

Table 13 **Vertical and horizontal errors for L1 compared to La processing using the current constellation and the currently used cutoff angle of 13 degrees.**

Error source		Vertical Error (mm)		Horizontal Error (mm)	
		L1	La	L1	La
Ionosphere		16.6	20.8	10.7	13.4
Troposphere		20.9	20.9	3.9	3.9
Local Effects	Rover	5.6	4.3	3.5	2.7
	Reference sites	1.4	1.1	0.9	0.7
Total (rms)		27.3	29.8	12.0	14.3

Table 14 **Vertical and horizontal errors for current constellation compared to the future constellation using the currently used cutoff angle of 13 and 24 degrees respectively and the La observable.**

Error source		Vertical Error (mm)		Horizontal Error (mm)	
		Current	Future	Current	Future
Ionosphere		20.8	16.3	13.4	9.5
Troposphere		20.9	14.3	3.9	2.7
Local Effects	Rover	4.3	3.0	2.7	1.8
	Reference sites	1.1	0.8	0.7	0.5
Total (rms)		29.8	21.9	14.3	10.1

3.2 Future quality using a densified Swedish infrastructure

In this section we study the effect of a densified reference network compared to the distance of 70 km between reference stations that we have used for the simulations in the previous section. Table 15 shows vertical and horizontal errors for current distance between reference stations (70 km) and a densified network with 35 km between reference stations.

Table 15 **Vertical and horizontal errors for current distance between reference stations (70 km) and a densified network with 35 km between reference stations.**

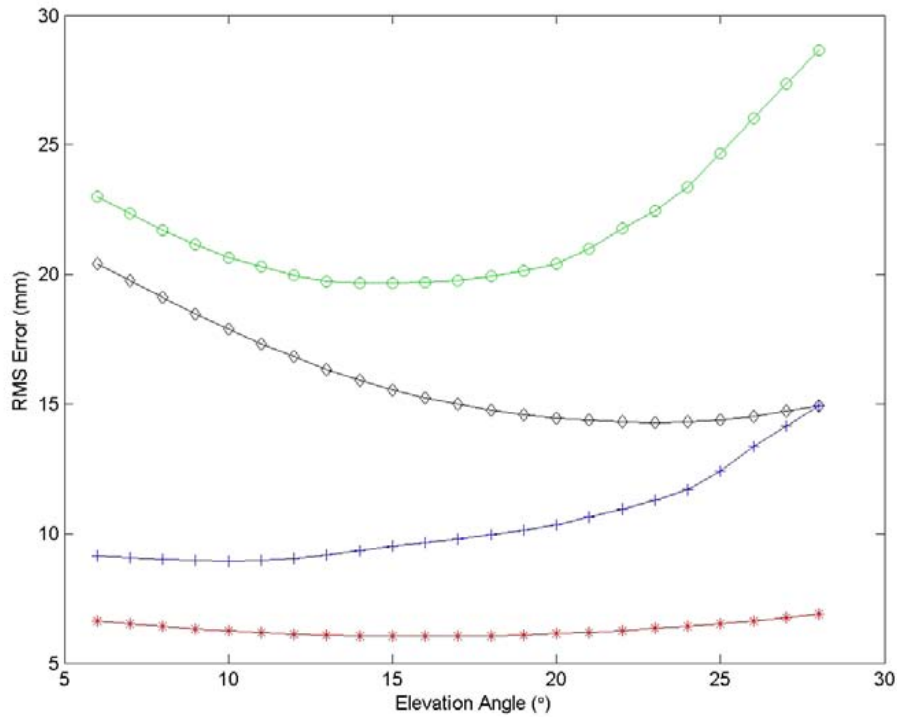| **Error source**		Vertical Error (mm)		Horizontal Error (mm)	
		70 km	35 km	70 km	35 km
Ionosphere		16.6	11.7	10.7	7.6
Troposphere		20.9	14.8	3.9	3.7
Local Effects	Rover	5.6	5.6	3.5	3.5
	Reference sites	1.4	1.4	0.9	0.9
Total (rms)		27.3	19.7	12.0	9.2

Figure 37 **RMS error as a function of elevation angle for the vertical and horizontal components for a reference network with 35 km distance between the reference stations. The curves represent from the top: vertical coordinate error using the current satellite constellation (green circles), vertical coordinate error using a future satellite constellation (black triangles), horizontal coordinate error using the current satellite constellation (blue plus signs), and horizontal coordinate error using a future satellite constellation (red stars).**

Table 16 **Vertical and horizontal errors for current constellation compared to the future constellation using the currently used cutoff angle of 13 and 24 degrees respectively for a network densified to 35 km.**

Error source		Vertical Error (mm)		Horizontal Error (mm)	
		Current	Future	Current	Future
Ionosphere		11.7	9.2	7.6	5.4
Troposphere		14.8	10.2	3.7	2.6
Local Effects	Rover	5.6	3.9	3.5	2.3
	Reference sites	1.4	1.0	0.9	0.6
Total (rms)		19.7	14.3	9.2	6.4

3.2.1 L3 processing and densified network (35 km)

Table 17 shows the errors for the densified network when processing using the L3 observable compared to the L1 observable.

Table 17   **Vertical and horizontal errors for L1 compared to L3 processing using the current constellation and the currently used cutoff angle of 13 degrees and a network densified to 35km.**

Error source		Vertical Error (mm)		Horizontal Error (mm)	
		L1	L3	L1	L3
Ionosphere		11.7	0.0	7.6	0.0
Troposphere		14.8	14.8	3.7	3.7
Local Effects	Rover	5.6	17.8	3.5	11.2
	Reference sites	1.4	4.6	0.9	2.9
Total (rms)		19.7	23.6	9.2	12.2

Figure 38 shows the rms error as a function of elevation angle for the vertical and horizontal components for a reference network with 35 km distance between the reference stations. All results are produced with the L3 combination. The optimal values are similar for those found for the L1 combination.
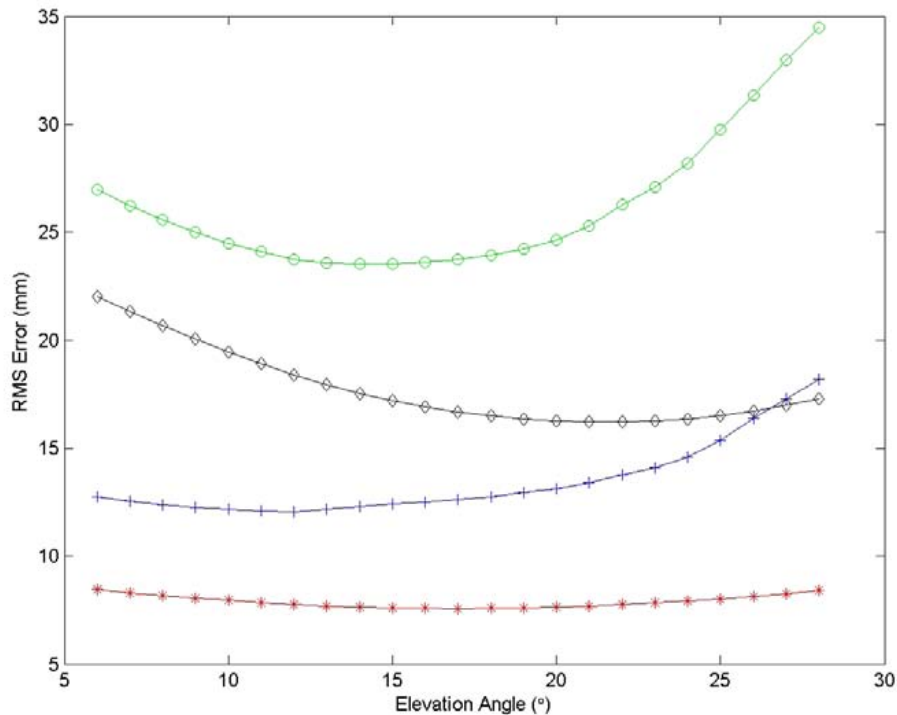

Figure 38   **RMS error as a function of elevation angle for the vertical and horizontal components for a reference network with 35 km distance between the reference stations. All results are produced with the L3 combination. The curves represent from the top: vertical coordinate error using the current satellite constellation (green circles), vertical coordinate error using a future satellite constellation (black triangles), horizontal coordinate error using the current satellite constellation (blue plus signs), and horizontal coordinate error using a future satellite constellation (red stars).**

Table 18 shows the vertical and horizontal errors for current constellation compared to the future constellation using the currently used cutoff angle of 13 and 24 degrees respectively and the L3 observable for a densified network. The total errors using the L3 observable is slightly larger than when using L1 only.

Table 18   **Vertical and horizontal errors for current constellation compared to the future constellation using the currently used cutoff angle of 13 and 24 degrees respectively and the L3 observable and a network densified to 35km.**

Error source		Vertical Error (mm)		Horizontal Error (mm)	
		Current	Future	Current	Future
Ionosphere		0.0	0.0	0.0	0.0
Troposphere		14.8	10.2	3.7	2.6
Local Effects	Rover	17.8	12.4	11.2	7.2
	Reference sites	4.6	3.2	2.9	1.9
Total (rms)		23.6	16.4	12.2	7.9

3.2.2   La processing and densified network (35 km)

Table 19 shows the errors for the densified network when processing using the La observable compared to the L1 observable.

Table 19   **Vertical and horizontal errors for L1 compared to La processing using the current constellation and the currently used cutoff angle of 13 degrees and a network densified to 35km.**

Error source		Vertical Error (mm)		Horizontal Error (mm)	
		L1	La	L1	La
Ionosphere		11.7	14.7	7.6	9.5
Troposphere		14.8	14.8	3.7	3.7
Local Effects	Rover	5.6	4.3	3.5	2.7
	Reference sites	1.4	1.1	0.9	0.7
Total (rms)		19.7	21.3	9.2	10.6

Figure 39 shows the rms error as a function of elevation angle for the vertical and horizontal components for a reference network with 35 km distance between the reference stations. All results are produced with the La combination. The optimal values are similar for those found for the L1.
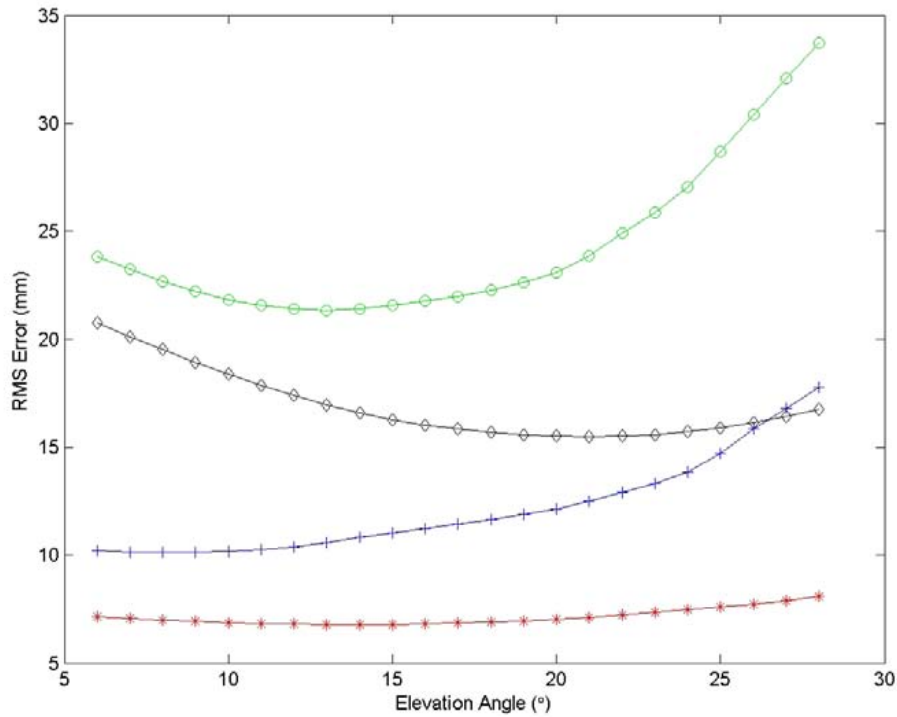
Figure 39   RMS error as a function of elevation angle for the vertical and horizontal components for a reference network with 35 km distance between the reference stations. All results are produced with the La combination. The curves represent from the top: vertical coordinate error using the current satellite constellation (green circles), vertical coordinate error using a future satellite constellation (black triangles), horizontal coordinate error using the current satellite constellation (blue plus signs), and horizontal coordinate error using a future satellite constellation (red stars).

Table 20 shows the Vertical and horizontal errors for current constellation compared to the future constellation using the currently used cutoff angle of 13 and 24 degrees respectively and the L3 observable for a densified network. The total errors using the La observable is slightly larger than when using L1 only.

Table 20   Vertical and horizontal errors for current constellation compared to the future constellation using the currently used cutoff angle of 13 and 24 degrees respectively and the La observable and a network densified to 35km.

Error source		Vertical Error (mm)		Horizontal Error (mm)	
		Current	Future	Current	Future
Ionosphere		14.7	11.5	9.5	6.7
Troposphere		14.8	10.2	3.7	2.6
Local Effects	Rover	4.3	3.0	2.7	1.8
	Reference sites	1.1	0.8	0.7	0.5
Total (rms)		21.3	15.7	10.6	7.5

3.3   Future quality using a densified Swedish infrastructure- 20 km and 10 km

In this section we study the effect of a densified reference network compared to the distance of 70 km and 35 km between reference stations that we have used for the simulations in the previous sections. The densified network in this section has distances between reference stations of 10 km and 20 km. This corresponds to the local areas where the RTK service is specially designed for specific projects.

3.3.1   20 km between reference stations

Table 21 shows vertical and horizontal errors for current distance between reference stations (70 km) and a densified network with 20 km between reference stations.

Table 21   **Vertical and horizontal errors for current distance between reference stations (70 km) and a densified network with 20 km between reference stations.**

Error source		Vertical Error (mm)		Horizontal Error (mm)	
		70 km	20 km	70 km	20 km
Ionosphere		16.6	8.9	10.7	5.7
Troposphere		20.9	10.9	3.9	3.5
Local Effects	Rover	5.6	5.6	3.5	3.5
	Reference sites	1.4	1.4	0.9	0.9
Total (rms)		27.3	15.2	12.0	7.6

Figure 40 shows rms error as a function of elevation angle for the vertical and horizontal components for a reference network with 20 km distance between the reference stations. The curves represent from the top: vertical coordinate error using the current satellite constellation (green circles), vertical coordinate error using a future satellite constellation (black triangles), horizontal coordinate error using the current satellite constellation (blue plus signs), and horizontal coordinate error using a future satellite constellation (red stars).
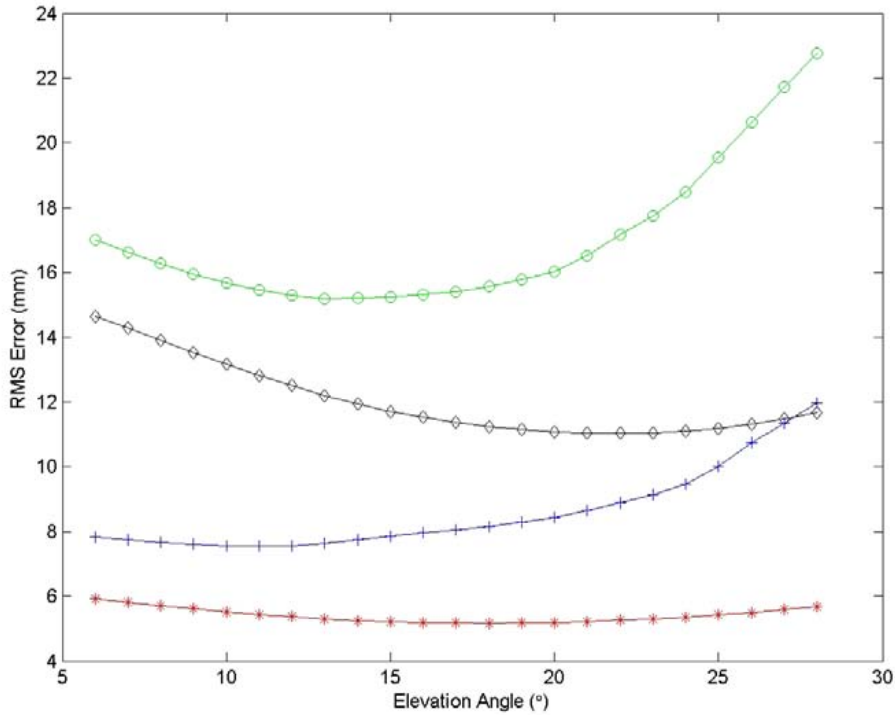
Figure 40 **RMS error as a function of elevation angle for the vertical and horizontal components for a reference network with 20 km distance between the reference stations. The curves represent from the top: vertical coordinate error using the current satellite constellation (green circles), vertical coordinate error using a future satellite constellation (black triangles), horizontal coordinate error using the current satellite constellation (blue plus signs), and horizontal coordinate error using a future satellite constellation (red stars).**

Table 23 shows the Vertical and horizontal errors for current constellation compared to the future constellation using the currently used cutoff angle of 13 and 24 degrees respectively

Table 22 **Vertical and horizontal errors for current constellation compared to the future constellation using the currently used cutoff angle of 13 and 24 degrees respectively for a densified network (20 km between reference stations).**

Error source		Vertical Error (mm)		Horizontal Error (mm)	
		Current	Future	Current	Future
Ionosphere		8.9	7.0	5.7	4.1
Troposphere		10.9	7.7	3.5	2.6
Local Effects	Rover	5.6	3.9	3.5	2.3
	Reference sites	1.4	1.0	0.9	0.6
Total (rms)		15.2	11.1	7.6	5.4

L3 Processing

Table 23 shows the vertical and horizontal errors for L1 compared to L3 processing using the current constellation and the currently used cutoff angle of 13 degrees. For such dense

networks as 20 km between the reference station the use of the L3 observable does not improve the results. The L3 observable increases the error contribution from the local effects while reducing the effect from the ionosphere to zero. For such dense networks as with 20 km between the reference stations, the contribution from the ionosphere is already relatively small.

Table 23   **Vertical and horizontal errors for L1 compared to L3 processing using the current constellation and the currently used cutoff angle of 13 degrees and a network densified to 20 km.**

Error source		Vertical Error (mm)		Horizontal Error (mm)	
		L1	L3	L1	L3
Ionosphere		8.9	0.0	5.7	0.0
Troposphere		10.9	10.9	3.5	3.5
Local Effects	Rover	5.6	17.8	3.5	11.2
	Reference sites	1.4	4.6	0.9	2.9
Total (rms)		15.2	21.3	7.6	12.1

Figure 41 shows the rms error as a function of elevation angle for the vertical and horizontal components for the reference network with 20 km distance between the reference stations. All results are produced with the L3 combination.
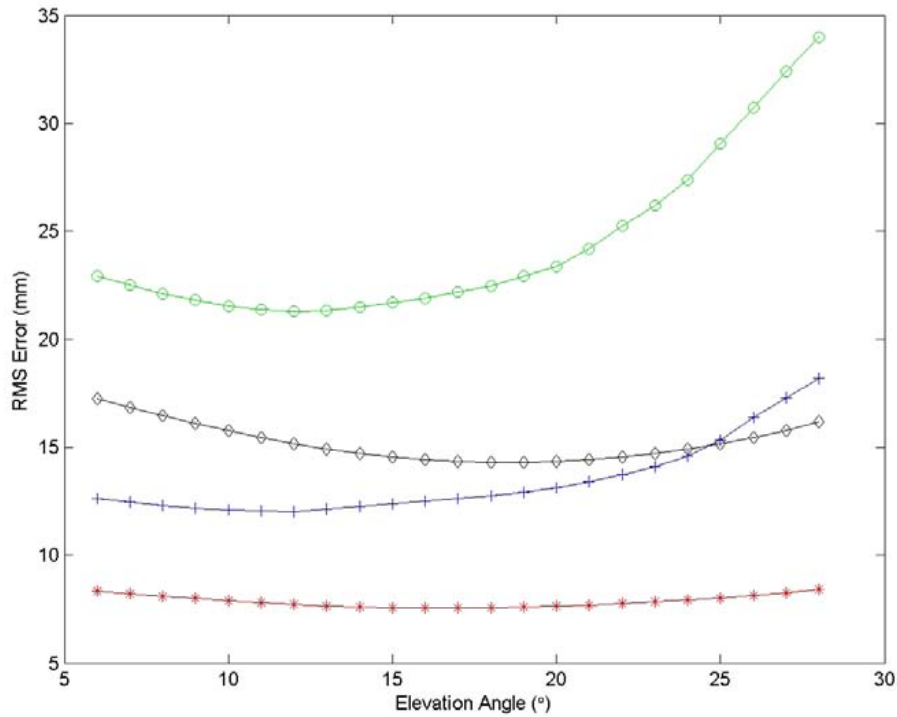
Figure 41 **RMS error as a function of elevation angle for the vertical and horizontal components for a reference network with 20 km distance between the reference stations. All results are produced with the L3 combination. The curves represent from the top: vertical coordinate error using the current satellite constellation (green circles), vertical coordinate error using a future satellite constellation (black triangles), horizontal coordinate error using the current satellite constellation (blue plus signs), and horizontal coordinate error using a future satellite constellation (red stars).**

Table 24 shows the vertical and horizontal errors for current constellation compared to the future constellation using the currently used cutoff angle of 13 and 24 degrees respectively.

Table 24 **Vertical and horizontal errors for current constellation compared to the future constellation using the currently used cutoff angle of 13 and 24 degrees respectively and the L3 observable for a densified network (20 km between reference stations).**

Error source		Vertical Error (mm)		Horizontal Error (mm)	
		Current	Future	Current	Future
Ionosphere		0.0	0.0	0.0	0.0
Troposphere		10.9	7.7	3.5	2.6
Local Effects	Rover	17.8	12.4	11.2	7.2
	Reference sites	4.6	3.2	2.9	1.9
Total (rms)		21.3	14.9	12.1	7.9

La Processing

Processing using the La observable can be helpful for dense networks. Table 25 shows the vertical and horizontal errors for L1 compared to La processing using the current constellation and the currently used cutoff angle of 13 degrees. The results using L1 and La are relatively similar in the total error budget. The La combination increases the ionosphere contribution while it reduces the contribution from the local effects.

Table 25   **Vertical and horizontal errors for L1 compared to La processing using the current constellation and the currently used cutoff angle of 13 degrees and a network densified to 20 km.**

Error source		Vertical Error (mm)		Horizontal Error (mm)	
		L1	La	L1	La
Ionosphere		8.9	11.1	5.7	7.2
Troposphere		10.9	10.9	3.5	3.5
Local Effects	Rover	5.6	4.3	3.5	2.7
	Reference sites	1.4	1.1	0.9	0.7
Total (rms)		15.2	16.2	7.6	8.5

Figure 42 shows the rms error as a function of elevation angle for the vertical and horizontal components for a reference network with 20 km distance between the reference stations. All results are produced with the La combination.
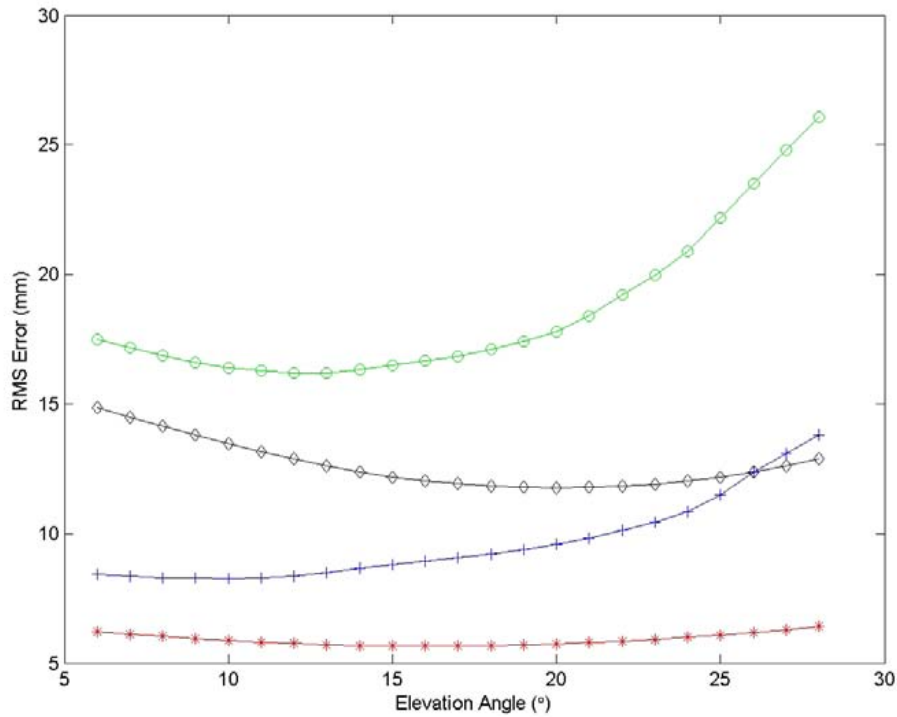
Figure 42 **RMS error as a function of elevation angle for the vertical and horizontal components for a reference network with 20 km distance between the reference stations. All results are produced with the La combination. The curves represent from the top: vertical coordinate error using the current satellite constellation (green circles), vertical coordinate error using a future satellite constellation (black triangles), horizontal coordinate error using the current satellite constellation (blue plus signs), and horizontal coordinate error using a future satellite constellation (red stars).**

Table 26 shows the vertical and horizontal errors for current constellation compared to the future constellation using the currently used cutoff angle of 13 and 24 degrees respectively and the La observable.

Table 26 **Vertical and horizontal errors for current constellation compared to the future constellation using the currently used cutoff angle of 13 and 24 degrees respectively and the La observable for a densified network (20 km between reference stations).**

Error source		Vertical Error (mm)		Horizontal Error (mm)	
		Current	Future	Current	Future
Ionosphere		11.1	8.7	7.2	5.1
Troposphere		10.9	7.7	3.5	2.6
Local Effects	Rover	4.3	3.0	2.7	1.8
	Reference sites	1.1	0.8	0.7	0.5
Total (rms)		16.2	12.0	8.5	6.0

3.3.2   10 km between reference stations

Table 27 shows the vertical and horizontal errors for current distance between reference stations (70 km) and a densified network with 10 km between reference stations. The densification reduces both the vertical and horizontal errors to about half their original sizes.

Table 27   **Vertical and horizontal errors for current distance between reference stations (70 km) and a densified network with 10 km between reference stations.**

Error source		Vertical Error (mm)		Horizontal Error (mm)	
		70 km	10 km	70 km	10 km
Ionosphere		16.6	6.3	10.7	4.1
Troposphere		20.9	7.1	3.9	3.3
Local Effects	Rover	5.6	5.6	3.5	3.5
	Reference sites	1.4	1.4	0.9	0.9
Total (rms)		27.3	11.1	12.0	6.4

Figure 43 shows the rms error as a function of elevation angle for the vertical and horizontal components for a reference network with 10 km distance between the reference stations.
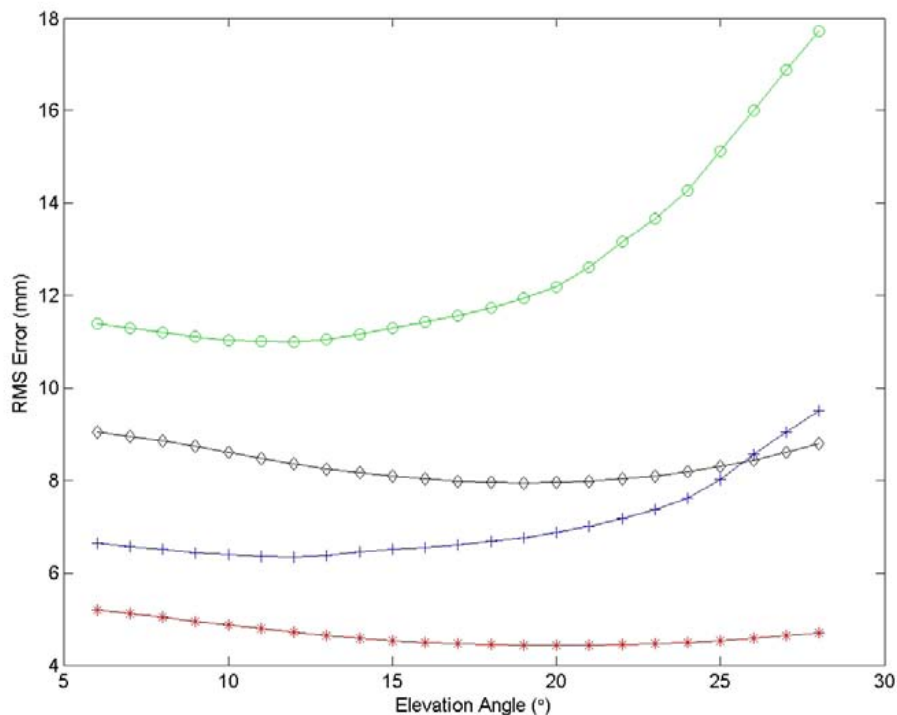

Figure 43   **RMS error as a function of elevation angle for the vertical and horizontal components for a reference network with 10 km distance between the reference stations. The curves represent from the top: vertical coordinate error using the current satellite constellation (green circles), vertical coordinate error using a future satellite constellation (black triangles), horizontal coordinate error using the current satellite constellation (blue plus signs), and horizontal coordinate error using a future satellite constellation (red stars).**

Table 28 shows the vertical and horizontal errors for current constellation compared to the future constellation using the currently used cutoff angle of 13 and 24 degrees respectively

Table 28   **Vertical and horizontal errors for current constellation compared to the future constellation using the currently used cutoff angle of 13 and 24 degrees respectively for a densified network (10 km between reference stations).**

Error source		Vertical Error (mm)		Horizontal Error (mm)	
		Current	Future	Current	Future
Ionosphere		6.3	4.9	4.1	2.9
Troposphere		7.1	5.2	3.3	2.5
Local Effects	Rover	5.6	3.9	3.5	2.3
	Reference sites	1.4	1.0	0.9	0.6
Total (rms)		11.1	8.2	6.4	4.5

L3 Processing

Table 29 shows the vertical and horizontal errors for L1 compared to L3 processing using the current constellation and the currently used cutoff angle of 13 degrees. Similar to the previous shown results, the use of the L3 observable does not improve the results for such a dense network.

Table 29   **Vertical and horizontal errors for L1 compared to L3 processing using the current constellation and the currently used cutoff angle of 13 degrees and a network densified to 10 km.**

Error source		Vertical Error (mm)		Horizontal Error (mm)	
		L1	L3	L1	L3
Ionosphere		6.3	0.0	4.1	0.0
Troposphere		7.1	7.1	3.3	3.3
Local Effects	Rover	5.6	17.8	3.5	11.2
	Reference sites	1.4	4.6	0.9	2.9
Total (rms)		11.1	19.6	6.4	12.1

Figure 44 shows the rms error as a function of elevation angle for the vertical and horizontal components for a reference network with 10 km distance between the reference stations. All results are produced with the L3 combination.
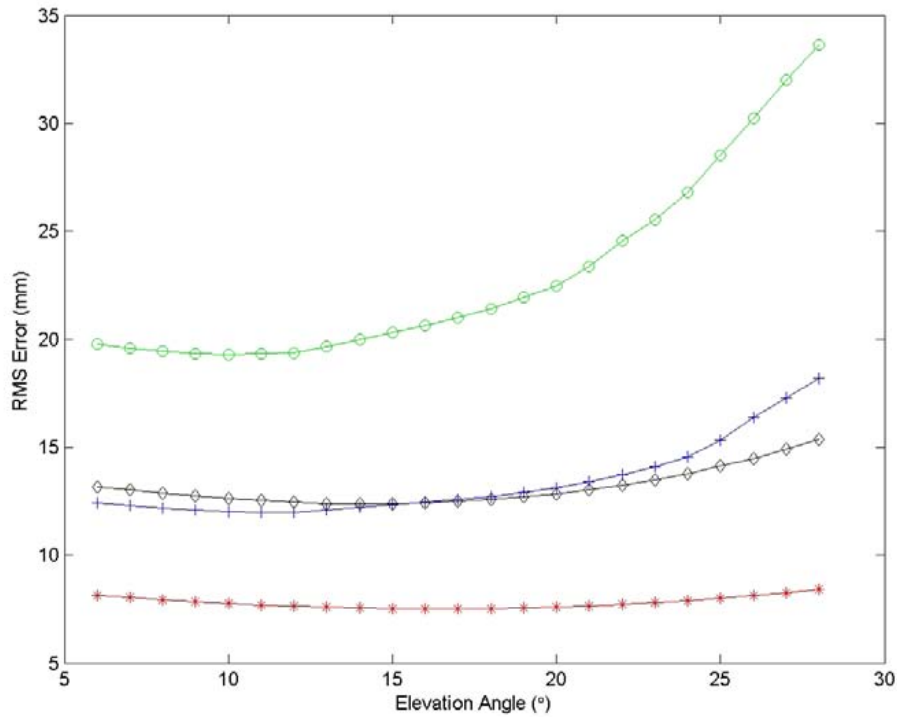
Figure 44   RMS error as a function of elevation angle for the vertical and horizontal components for a reference network with 10 km distance between the reference stations. All results are produced with the L3 combination. The curves represent from the top: vertical coordinate error using the current satellite constellation (green circles), vertical coordinate error using a future satellite constellation (black triangles), horizontal coordinate error using the current satellite constellation (blue plus signs), and horizontal coordinate error using a future satellite constellation (red stars).

Table 30 shows the Vertical and horizontal errors for current constellation compared to the future constellation using the currently used cutoff angle of 13 and 24 degrees respectively. We have chosen to specify the results using a cutoff angle of 24 degrees in order to simplify comparison with previous results using a future constellation.

Table 30   Vertical and horizontal errors for current constellation compared to the future constellation using the currently used cutoff angle of 13 and 24 degrees respectively and the L3 observable for a densified network (10 km between reference stations).

Error source		Vertical Error (mm)		Horizontal Error (mm)	
		Current	Future	Current	Future
Ionosphere		0.0	0.0	0.0	0.0
Troposphere		7.1	5.2	3.3	2.5
Local Effects	Rover	17.8	12.4	11.2	7.2
	Reference sites	4.6	3.2	2.9	1.9
Total (rms)		19.6	13.8	12.1	7.9

La Processing

Table 31 shows the vertical and horizontal errors for L1 compared to La processing using the current constellation and the currently used cutoff angle of 13 degrees. The results using L1 and La are very similar both for the vertical and horizontal component.

Table 31   Vertical and horizontal errors for L1 compared to La processing using the current constellation and the currently used cutoff angle of 13 degrees and a network densified to 10 km.

Error source		Vertical Error (mm)		Horizontal Error (mm)	
		L1	La	L1	La
Ionosphere		6.3	7.9	4.1	5.1
Troposphere		7.1	7.1	3.3	3.3
Local Effects	Rover	5.6	4.3	3.5	2.7
	Reference sites	1.4	1.1	0.9	0.7
Total (rms)		11.1	11.5	6.4	6.7

Figure 45 shows the rms error as a function of elevation angle for the vertical and horizontal components for a reference network with 10 km distance between the reference stations. All results are produced with the La combination.
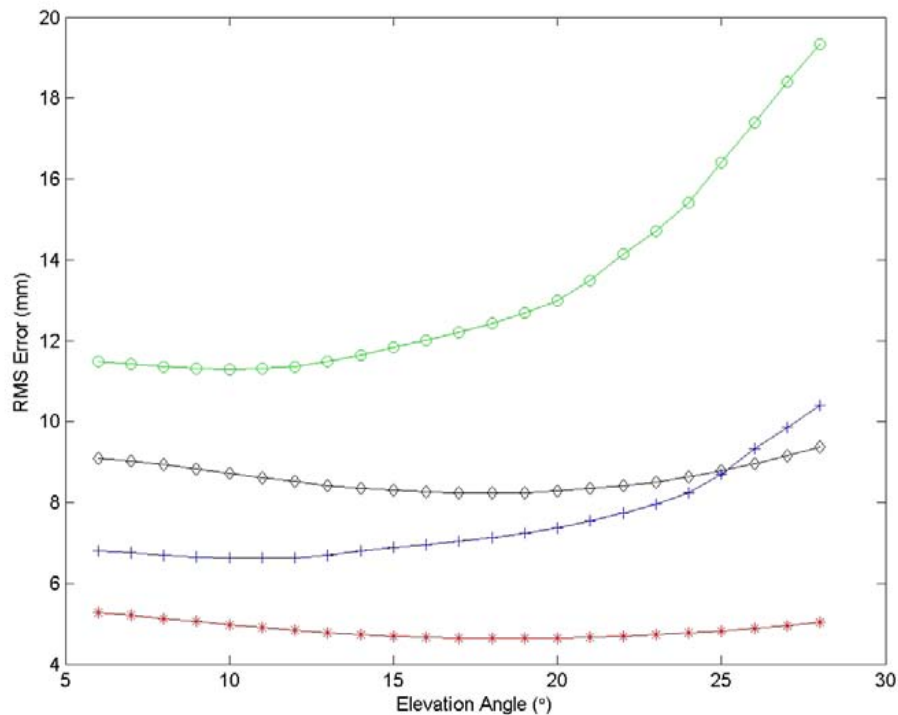

Figure 45   RMS error as a function of elevation angle for the vertical and horizontal components for a reference network with 10 km distance between the reference stations. All results are produced with the La combination. The curves represent from the top: vertical coordinate error using the current satellite constellation (green circles), vertical coordinate error using a future satellite constellation (black triangles), horizontal coordinate error using the current satellite constellation (blue plus signs), and horizontal coordinate error using a future satellite constellation (red stars).

Table 32 shows the vertical and horizontal errors for current constellation compared to the future constellation using the currently used cutoff angle of 13 and 24 degrees respectively.

Table 32   **Vertical and horizontal errors for current constellation compared to the future constellation using the currently used cutoff angle of 13 and 24 degrees respectively and the La observable for a densified network (10 km between reference stations).**

Error source		Vertical Error (mm)		Horizontal Error (mm)	
		Current	Future	Current	Future
Ionosphere		7.9	6.2	5.1	3.6
Troposphere		7.1	5.2	3.3	2.5
Local Effects	Rover	4.3	3.0	2.7	1.8
	Reference sites	1.1	0.8	0.7	0.5
Total (rms)		11.5	8.6	6.7	4.8

3.4   Summary

When the future satellite systems Galileo, Compass are complete and can be used in RTK-processing, the optimal choice of elevation cutoff angle changes from approximately 13 degrees today to approximately 25 degrees. The vertical error is reduced from 27 mm to 20 mm for our nominal setup when these future systems can be used. The use of the L3 combination compared to L1 does not reduce the uncertainty for the nominal setup. This setup, however, includes a standard ionosphere variability. Hence for times with a high spatial variability in the ionosphere, the L3 combination will be preferable. See for example the ionosphere contribution in Table 5. This conclusion holds for both the current constellation and the future. A densified network with 35 km between the reference stations results in a similar improvement as the contribution of the new satellite systems. The error in the vertical coordinate is reduced from 27 mm to 20 mm for our nominal setup. Using both a densified network and the new satellite systems reduces the error in the vertical component further down to 14 mm. For dense network, such as distance between the reference stations around 10 km, the vertical error is 11 mm and down to 8 mm for the full future satellite constellation. For such dense network the La combination can be useful for periods with low spatial variability in the ionosphere. Other combinations including several observables may also be of interest.

4   Work Package 3

4.1   Introduction

In this work package, we study methods that can improve the future quality of network-RTK. In the first part of this work, we study different possibilities for forming linear combinations of the GNSS observables at different frequencies. We then go on to study approaches in the estimation technique. First, we investigate the potential benefits with estimating a local troposphere delay above the rover position.

Secondly, we investigate the possibility to estimate the Zenith Wet Delay (ZWD) above one location from a number of measurements of the ZWD at reference stations around that location. Finally, we study the possibility of incorporating external information about weather conditions in order to improve the results.

4.2 Linear combination of observables

In order to find useful linear combinations of the observables at the different GNSS frequencies, we write the linear combination as

$$\hat{\ell} = a\ell_1 + b\ell_2 + c\ell_3 \tag{18}$$

Here, we want to find values for the weights *a* and *b*. We seek *a* and *b* so that the expected difference between the combined observable and the true geometrical range to the satellite *l* is equal to zero.

$$E\left[\hat{\ell} - \ell\right] = 0 \tag{19}$$

We also want the variance of $\hat{\ell} - \ell$

$$Var\left[\hat{\ell} - \ell\right] \tag{20}$$

To be minimized. Assuming that the expected contribution from the ionosphere, the neutral atmosphere, and the receiver measurement noise to the observed signal is identical for both the rover and reference station, we obtain the condition *a+b=1*. We can now solve for the parameters *a* and *b* that minimizes the variance of $\hat{\ell} - \ell$. The solution, see Appendix II, to this equation is:

$$a = \frac{\varsigma_2^2 g + \sigma_2^2 - \varsigma_1\varsigma_2 g + \sigma_1\sigma_2\chi}{\varsigma_1^2 g + \sigma_1^2 + \varsigma_2^2 g + \sigma_2^2 - 2\varsigma_1\varsigma_2 g + 2\sigma_1\sigma_2\chi} \tag{21}$$

and

$$b = 1 - \frac{\varsigma_2^2 g + \sigma_2^2 - \varsigma_1\varsigma_2 g + \sigma_1\sigma_2\chi}{\varsigma_1^2 g + \sigma_1^2 + \varsigma_2^2 g + \sigma_2^2 - 2\varsigma_1\varsigma_2 g + 2\sigma_1\sigma_2\chi} \tag{22}$$

We can now make a few assumptions in order to calculate *a* and *b*. We assume measurement values for the noise parameters as $\sigma_1 = \sigma_{0,1} / \sin(elevation)$ and $\sigma_2 = \sigma_{0,2} / \sin(elevation)$ where $\sigma_{0,1}$ and $\sigma_{0,2}$ is equal to 2.4mm and 2.9 mm respectively, see Table 2. We also assume zero correlation between the measurements noise on the two frequencies, $\chi = 0$. By now using the Klobuchar model [*Klobuchar*, 1996] for the ionosphere variation with distance and assuming a first order ionospheric effect on the received GPS signals, we can calculate *a* as a function of distance between the GNSS antennas for a certain satellite constellation.

Figure 46 shows *a* as a function of distance between the antennas for observations with three different elevation angles to the satellite. In the figure is also shown the ionospheric effect on the L1 frequency calculated using the Klobuchar model for December 17, 2007 for the location 60° North and 15° East.
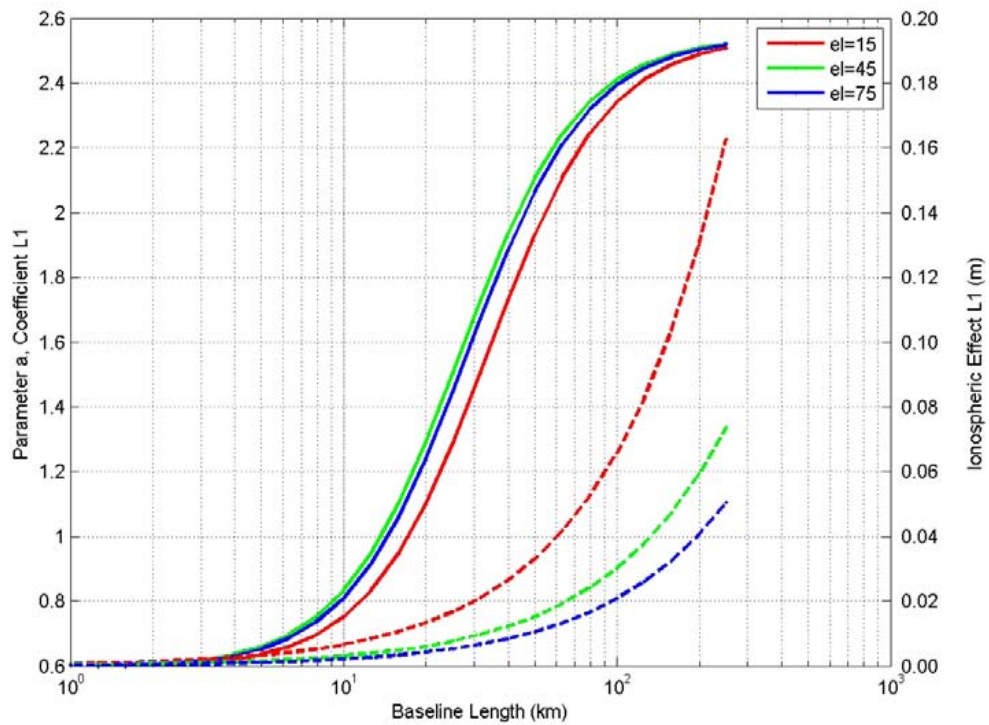
Figure 46   **Values for the parameter a together with the ionospheric effect on L1. The values are presented for three different choices of elevation angles, namely 15, 45, and 75 degrees in south direction.**

The figure clearly shows that for short baselines, i.e., distances less than or equal to 1 km, we should chose $a=0.61$ and $b=0.39$. For such short distances, the contribution from the ionosphere is negligible. For long baselines, i.e., distances larger than 100 km, the parameters approach $a=2.55$ and $b=-1.55$ which is the standard linear combination of the observables on L1 and L2 forming the ionosphere independent L3 combination. For intermediate baselines, i.e., between 1 and 100 km, there is a smooth transition between the reported values. Interesting to note is that for baselines of about 15 km, the optimal solution for a is equal to one. As a consequence the value for b is zero. Hence the optimal solution is to use only the L1 observable in the parameter estimation process.

We can now use the results obtained in order to study the effect on the estimated position. Under the same assumptions as before on receiver noise and ionospheric and neutral atmospheric variability together with satellite constellation, we can estimate position error as function of baseline length. We used the satellite constellation for December 17, 2007 at noon as seen from for the location 60° North and 15° East. The horizontal and vertical position error was calculated, see Figure 47 and Figure 48. The calculation was performed for different baseline lengths between the rover and reference station. For each baseline optimal a and b parameters were derived. These parameters were calculated, for each baseline, as mean values of the individual a and b parameters for each observation.
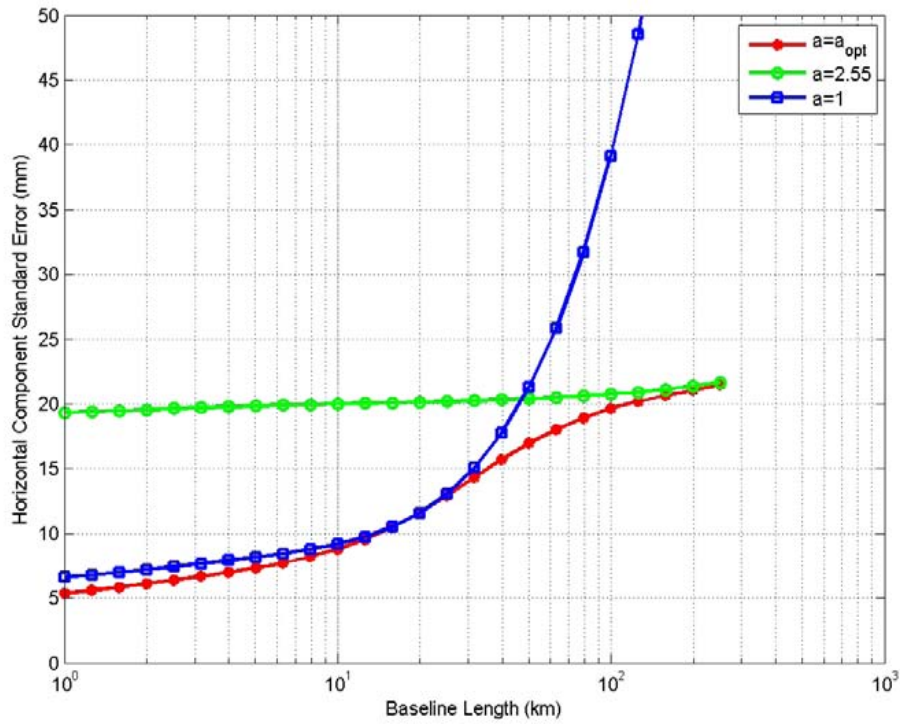
Figure 47   **Estimated position error in the horizontal component as function of baseline length.**
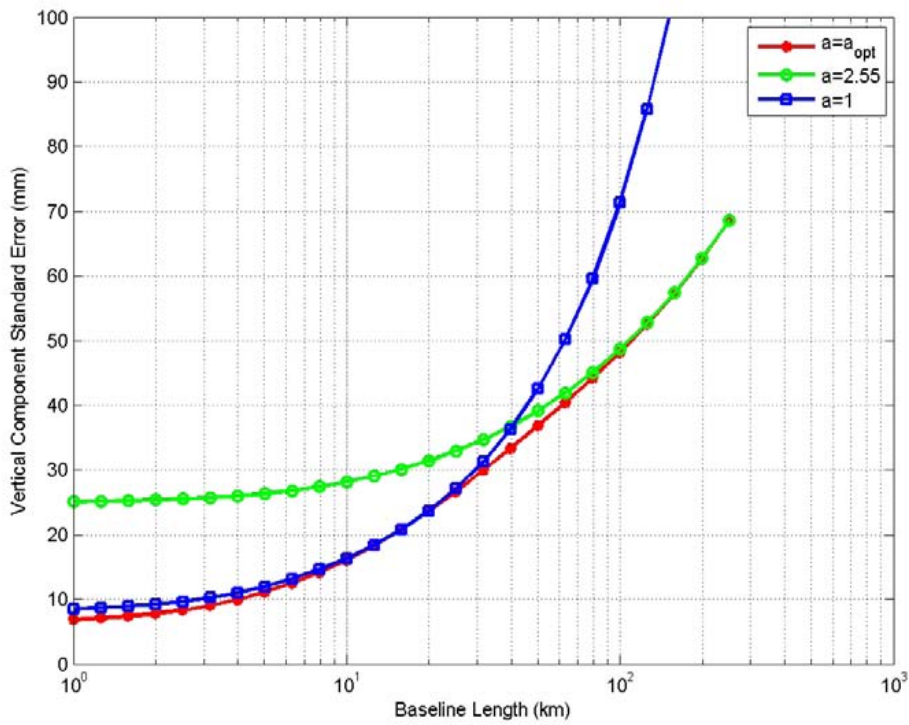

Figure 48   **Estimated position error in the vertical component as function of baseline length.**

The optimal solution agrees well with the L1 only solution for baselines around 10 km and with the L3 combination for baselines longer than 100 km. For distances between 10 and 100 km we can have an improvement of almost 15% in the horizontal component when choosing the combination presented in this paper compared to the more appropriate of the two others. The improvement is less significant for the vertical component.

In analogy with the procedure for the two-frequency linear combination, it is possible to extend the calculation also to the three-frequency situation. We can then calculate optimal values for the weight parameters a, b and c. Expressions for these estimates are given in Appendix II.

We calculate a, b and c as a function of baseline distance in analogy with the parameter determination for the two-frequency case. In addition to the measurement values for the noise parameters $\sigma_1 = \sigma_{0,1}/\sin(elevation)$ and $\sigma_2 = \sigma_{0,2}/\sin(elevation)$ where $\sigma_{0,1}$ and $\sigma_{0,2}$ is equal to 2.4mm and 2.9 mm respectively, we assume $\sigma_{0,3} = 2.4$ mm and the same elevation dependence. We also assume zero correlation between the measurements noise on all frequencies, $\chi_1 = \chi_2 = \chi_3 = 0$. We use the Klobuchar model [*Klobuchar*, 1996] for the ionosphere variation with distance, see Figure 63, and assume a first order ionospheric effect on the received GNSS signals. Figure 49, Figure 50, and Figure 51 shows a, b, $and c$ as functions of distance between the GNSS antennas for observations with three different elevation angles to the satellite. In the Figure 49 is also shown the ionospheric effect on the L1 frequency calculated using the Klobuchar model for December 17, 2007 for the location 60° North and 15° East.
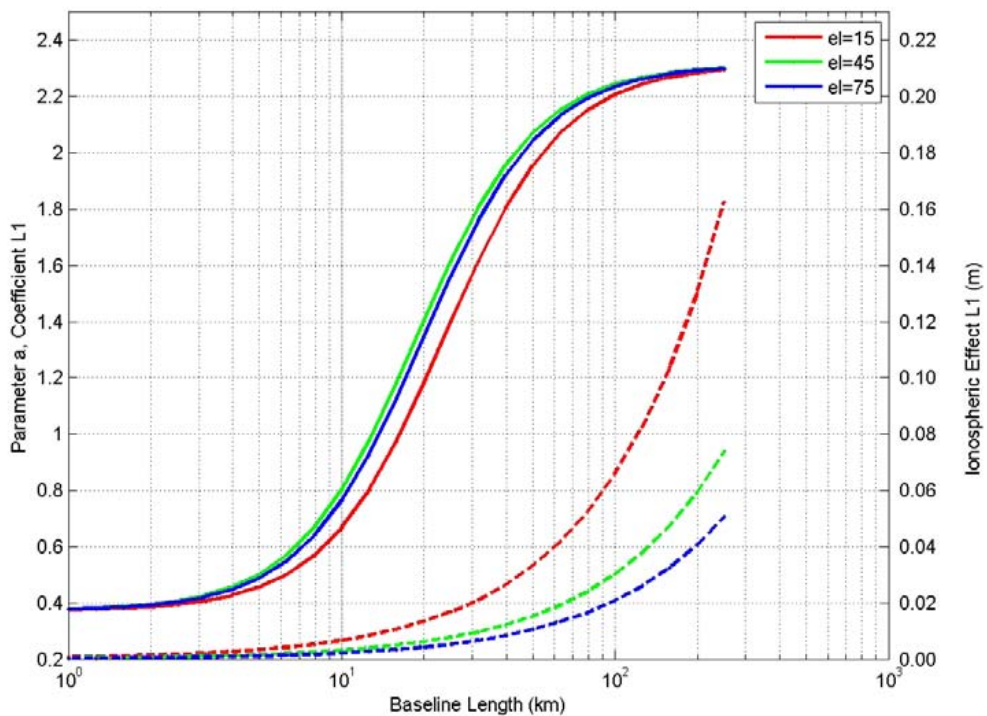

Figure 49   **Values for the parameter a together with the ionospheric effect on L1. The values are presented for three different choices of elevation angles, namely 15, 45, and 75 degrees.**
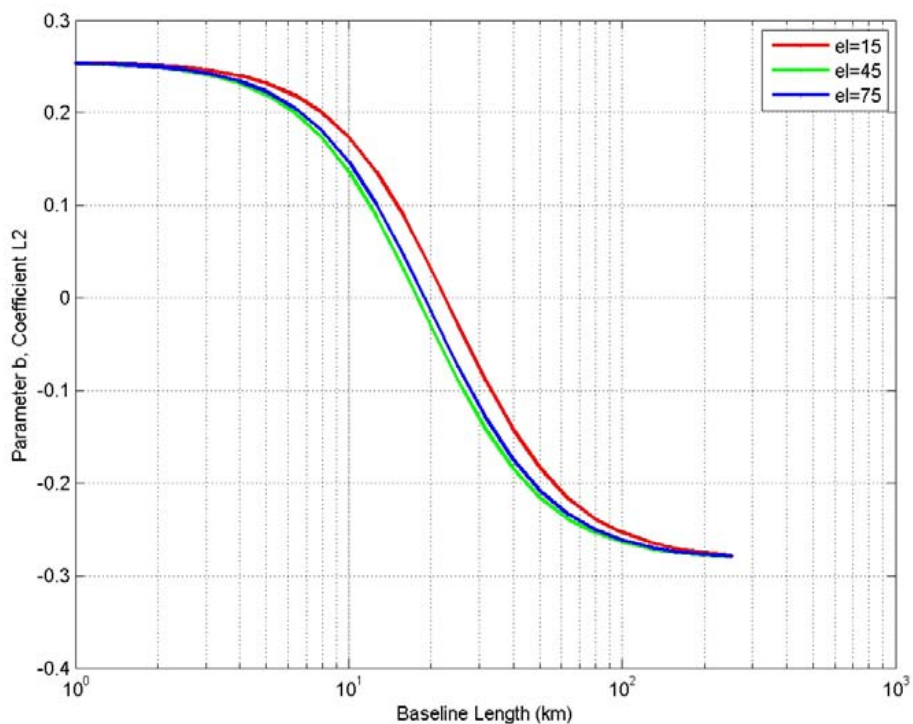
Figure 50   **Values for the parameter b on L2. The values are presented for three different choices of elevation angles, namely 15, 45, and 75 degrees.**
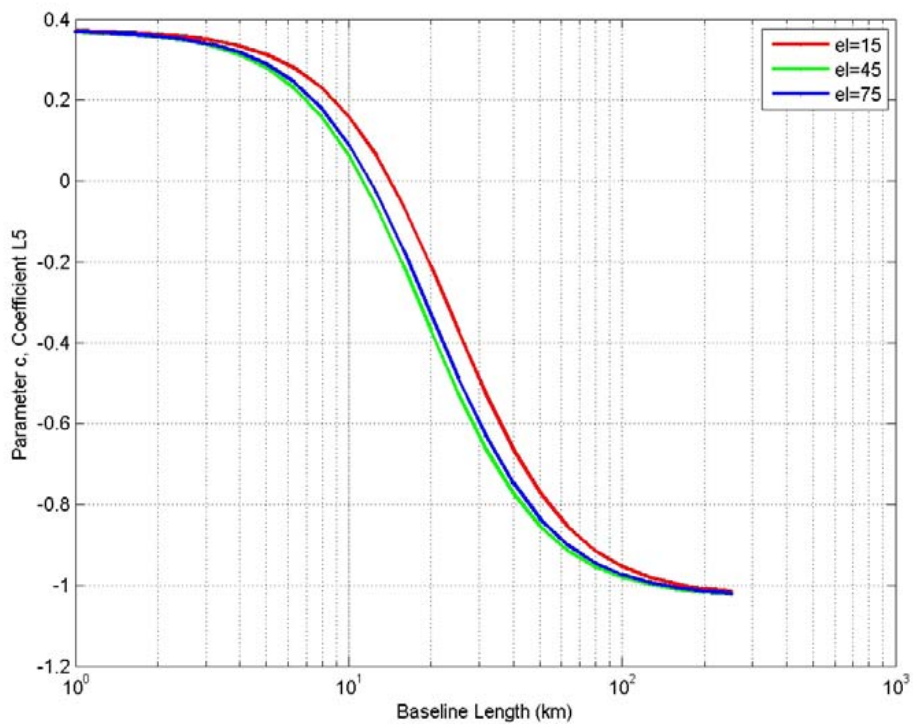

Figure 51   **Values for the parameter c on L5. The values are presented for three different choices of elevation angles, namely 15, 45, and 75 degrees.**

4.3 Estimation of a local troposphere

Normally in network-RTK processing, four parameters are estimated for the rover. These are the three coordinate components plus the rover receiver clock error. The other components affecting the received signal are to a large extent cancelled by the interpolation performed in the network-RTK concept. If however, the remaining contribution from the troposphere as specified in the two previous work package descriptions are relatively large there may be an advantage by estimating this effects in order to cancel its effect.

4.3.1 Nominal GNSS

Table 33 shows the vertical and Horizontal errors for the current satellite constellation when using the standard network-RTK processing and when estimating a local troposphere component. For this satellite constellation there is no advantage with estimating a local troposphere component.

Table 33 **Vertical and Horizontal errors for the current satellite constellation when using the standard network-RTK processing and when estimating a local troposphere component. A 13 degree cutoff angle is used.**

Error source		Vertical Error (mm)		Horizontal Error (mm)	
		Standard	Local Trop	Standard	Local Trop
Ionosphere		16.6	51.0	10.7	11.4
Troposphere		20.9	5.3	3.9	2.3
Local Effects	Rover	5.6	17.2	3.5	3.8
	Reference sites	1.4	4.4	0.9	1.0
Total (rms)		27.3	54.3	12.0	12.3

Figure 52 shows rms error as a function of elevation angle for the vertical and horizontal components. When estimating a local troposphere is an advantage to use a low elevation cutoff angle. Both for the vertical and horizontal components we find the best results for the lowest elevation cutoff angle in the study. However, using such a low elevation cutoff angle may not be suitable for many practical purposes so in the following we will use an elevation cutoff angle of 10 degrees as the optimal choice when performing estimating of a local troposphere.
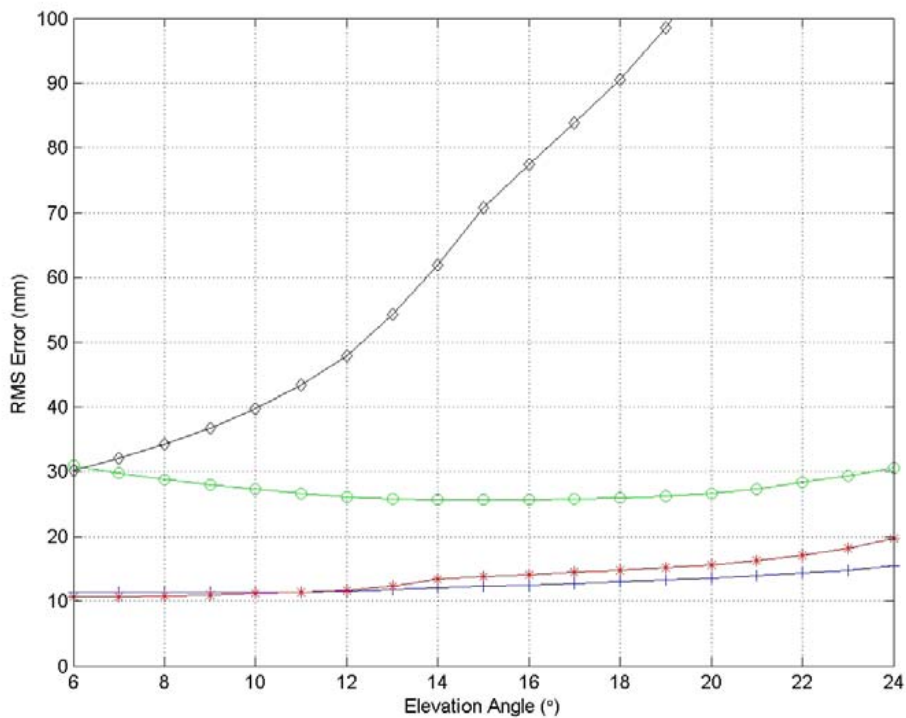
Figure 52   **RMS error as a function of elevation angle for the vertical and horizontal components for a reference network with 70 km distance between the reference stations and the current satellite constellation. All results are produced with the L1 combination. The curves represent from the top: vertical coordinate error when estimating a local troposphere (black triangles), vertical coordinate error using a standard processing (green circles), horizontal coordinate error using standard processing (blue plus signs), and horizontal coordinate error when estimating a local troposphere (red stars).**

Table 34 shows the vertical and horizontal errors for the current satellite constellation when using the standard network-RTK processing and when estimating a local troposphere component. In this table the elevation cutoff angle of 10 degrees when estimating a local troposphere is chosen according to Figure 52 . This results in an improvement in the results. However, standard processing is still performing better. Notable is that the results in the horizontal component are slightly improved when estimating a local troposphere, 11.2 mm compared to 12.0 mm.

Table 34 **Vertical and Horizontal errors for the current satellite constellation when using the standard network-RTK processing and when estimating a local troposphere component. The elevation cutoff angle is 13 and 10 degrees respectively.**

Error source		Vertical Error (mm)		Horizontal Error (mm)	
		Standard	Local Trop	Standard	Local Trop
Ionosphere		16.6	36.8	10.7	10.2
Troposphere		20.9	5.2	3.9	2.6
Local Effects	Rover	5.6	13.4	3.5	3.6
	Reference sites	1.4	3.5	0.9	0.9
Total (rms)		27.3	39.7	12.0	11.2

4.3.2   Future GNSS

Table 35 shows the vertical and horizontal errors for the future satellite constellation when using the standard network-RTK processing and when estimating a local troposphere component. The results in the table are produced using an elevation cutoff angle of 13 degree. Figure 53 shows the rms error as a function of the chosen elevation cutoff angle. We can see from the figure as in Figure 52 that when estimating a local troposphere component lower cutoff angles are preferable.

Table 35 **Vertical and Horizontal errors for the future satellite constellation when using the standard network-RTK processing and when estimating a local troposphere component. The elevation cutoff angle is 13 degrees.**

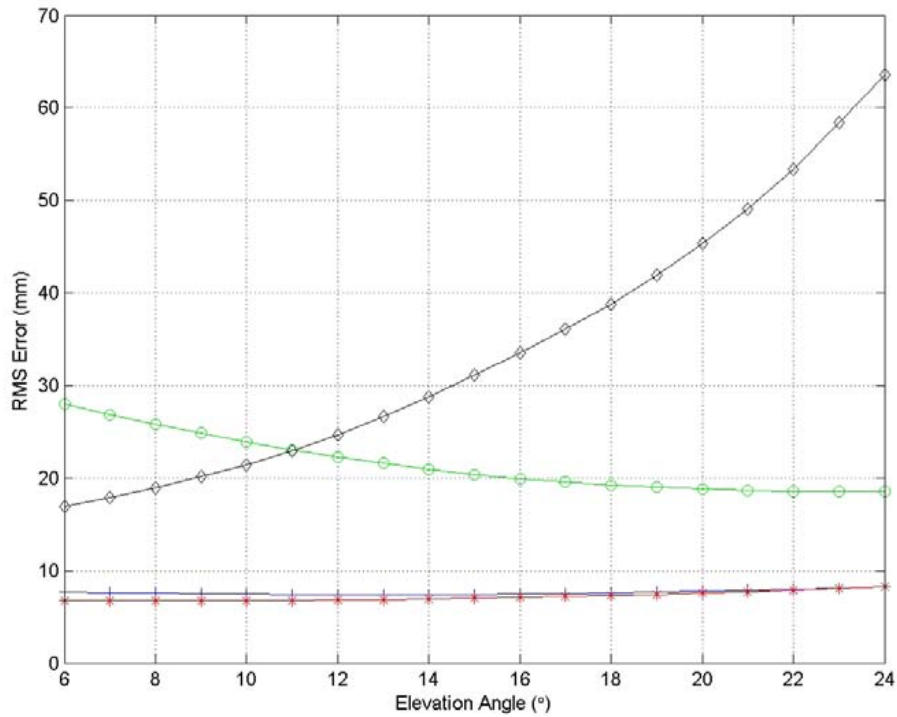| Error source		Vertical Error (mm)		Horizontal Error (mm)	
		Standard	Local Trop	Standard	Local Trop
Satellite clocks		0	0	0	0
Satellite orbits		0	0	0	0
Ionosphere		9.3	24.8	6.2	6.1
Troposphere		20.8	3.8	3.8	2.2
Local Effects	Rover	3.2	8.7	2.1	2.1
	Reference sites	0.8	2.2	0.5	0.5
Total (rms)		23.0	26.6	7.5	6.9

Figure 53   **RMS error as a function of elevation angle for the vertical and horizontal components for a reference network with 70 km distance between the reference stations and the future satellite constellation. All results are produced with the L1 combination. The curves represent from the top: vertical coordinate error when estimating a local troposphere (black triangles), vertical coordinate error using a standard processing (green circles), horizontal coordinate error using the standard processing (blue plus signs), and horizontal coordinate error when estimating a local troposphere (red stars).**

Table 36 shows the vertical and horizontal errors for the future satellite constellation when using the standard network-RTK processing and when estimating a local troposphere component. The elevation cutoff angle here is 24 and 10 degrees respectively, that is the optimal choice for the two processing strategies. Also in this case the only improvement when estimating a local troposphere is in the horizontal component. However, we can see from the table that estimating a local troposphere may be advantage for sparser networks than those used in this study, that is with a distance of 70 km between the reference networks.

Table 36   **Vertical and Horizontal errors for the future satellite constellation when using the standard network-RTK processing and when estimating a local troposphere component. The elevation cutoff angle is 24 and 10 degrees respectively.**

Error source		Vertical Error (mm)		Horizontal Error (mm)	
		Standard	Local Trop	Standard	Local Trop
Ionosphere		13.0	19.7	7.6	5.9
Troposphere		14.3	3.8	2.7	2.6
Local Effects	Rover	3.9	7.4	2.3	2.1
	Reference sites	1.0	1.9	0.6	0.5
Total (rms)		19.7	21.4	8.4	6.7

4.4   Propagation through a Network

The accuracy of interpolation of the ZWD was investigated by *Emardson and Johansson* [1998]. They however only considered using the spatial information, i.e. only data from the epoch being estimated was used in the interpolation. However, there might also be a benefit of including data from epochs before (and after, although this is not possible for a real-time system) the estimated epoch. Especially, this could be a benefit during passages of weather fronts when there is a clear pattern in the ZWD occurring moving across the area. *Emardson and Webb* [2002] showed that the motion of water vapour can be estimated from time-series of GPS derived ZWD data from a local network. They also suggested that the technique could be used for the interpolation of the ZWD.
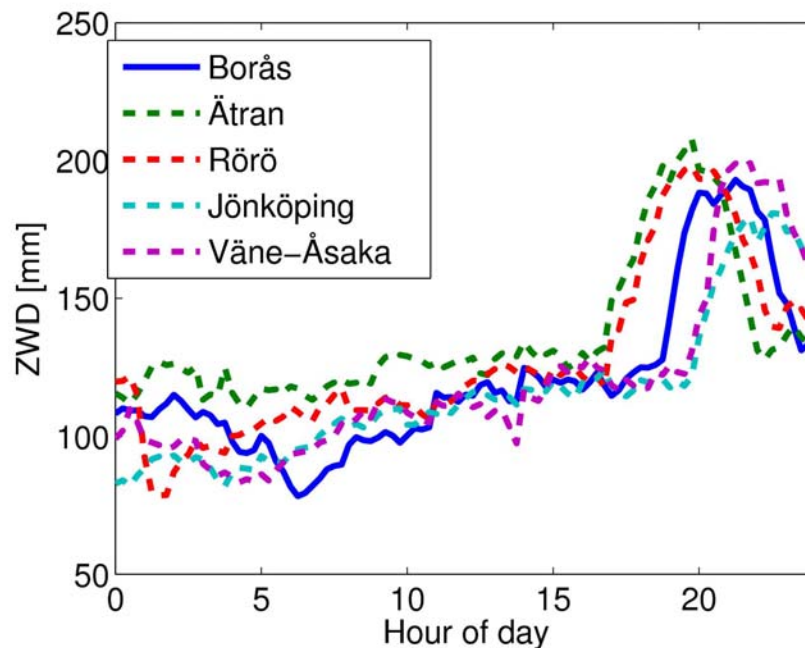

Figure 54   **ZWD estimated from GPS data for the Borås, Ätran, Rörö, Jönköping, and Väne-Åsaka stations on July 10, 2008.**

We begin of an example of a day when it possibly could be a benefit of using temporal as well as spatial information when interpolating the ZWD. Figure 54 shows the ZWD on July 10, 2008, estimated from GPS data at the station Borås, as well as the surrounding stations Ätran, Rörö, Jönköping, and Väne-Åsaka. As seen there is a peak in the ZWD occurring at Borås at the end of the day. The same peak is seen in the time series for the surrounding stations also, however shifted in time. The peak is seen about 1.5-2 hours earlier at the Ätran (to the South of Borås) and Rörö (to the West) stations, while the peak occurs 1-1.5 hour later at Jönköping (East) and Väne-Åsaka (North-North-West). Hence, it would seem that when estimating the ZWD at Borås for this day using data from the surrounding stations, there should be a benefit of using the information about the temporal variations in the ZWD as well as the spatial variations.

In this work we will consider three different Minimum mean square error (MMSE) estimators. See Appendix III for derivations of the estimators and theory on atmospheric turbulence. The first estimator, called Estimator A, only uses data from the epoch being estimated. Hence this estimator does not need any information about the wind. The other two also uses information about the temporal variations of the ZWD at the references stations. Theses also include data from a period of few hours (in most cases five) prior to the estimated epoch. These of course will require knowledge of the wind velocity. Estimator B estimate the wind using an ML estimator (equation C9), while with Estimator B1 assumes the wind velocity to be known. Estimator B1 will only be used in the simulations since in reality the wind will not be known precisely.

4.4.1   Simulations

The MMSE estimators are first tested through simulations. In order to simulate ZWD data an approach similar to what is presented in *Nilsson et al.* [2007] is used. We use a covariance matrix C to describe the relationship between the ZWD at different locations and different times. See Appendix III for description of C. By making a decomposition of C on the form $C = DD^T$, simulated values of network variations $\boldsymbol{\delta l}$ and the local variations $\delta \ell_e$ of ZWD can be obtained by:

$$\begin{bmatrix} \boldsymbol{\delta l} \\ \delta \ell_e \end{bmatrix} = D\mathbf{r} \qquad\qquad (23)$$

where $\mathbf{r}$ is a vector of $n+1$ independent zero-mean Gaussian random numbers with variance 1.
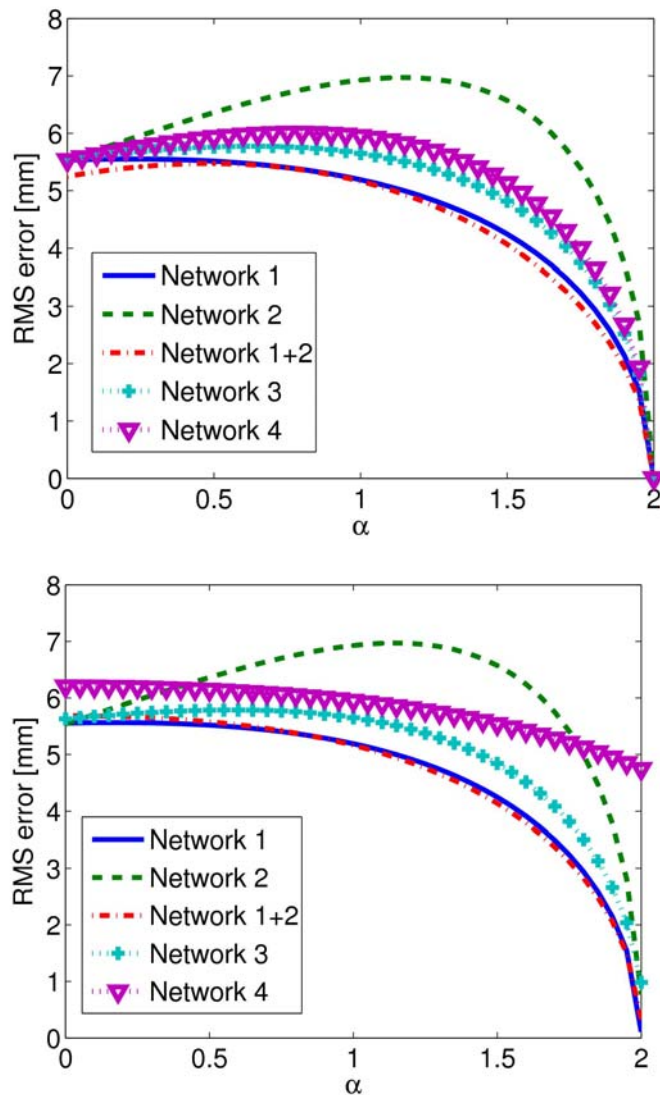
Figure 55   The accuracy of Estimator A as function of α for five different networks (see text). In the upper panel, the true α is known while in the lower panel, $\alpha = 1$ is assumed in the estimator.

We first investigate the accuracy of Estimator A. Figure 55 shows the expected accuracy when predicting the ZWD at the Borås station using data from different networks of reference stations. Network 1 consist of four stations distributed relatively symmetric around Borås: Rörö, Ätran, Jönköping, and Väne-Åsaka. Network 2 also consist of four stations located relatively symmetric around Borås but at larger distances: Kållandsö, Skagen, Knäred, and Aneby. Network 3 consist of four station distributed less symmetrically around Borås: Falköping, Väne-Åsaka, Aneby, and Falkenberg. Finally Network 4 consist of four stations all located to the north of Borås: Kållandsö, Falköping, Väne-Åsaka, and Tjurholmen. The accuracy is investigated as function of α. Two cases are considered: on case where the true value of α is known in the estimator and one case where $\alpha = 1$ is assumed in the estimator. The parameter k^2 is chosen such that the RMS ZWD variations over a 50 km baseline is 7 mm.

As seen in Figure 55 we can see that the accuracy is much better when using Network 1 compared to Network 2, which is not surprising given that the stations in Network 2 is located further away from Borås. We can also see that there is hardly any improvement in using both Networks 1 and 2 compared to only using Network 1. This shows that the

stations further away do not contain any additional information on the ZWD in Borås. We can also note that there is hardly any decrease in the accuracy when assuming $\alpha = 1$ in the estimator, expect for Network 4. Hence, unless the network of reference stations is asymmetric and all stations are located more or less in the same direction, we do not need to know α precisely but can assume $\alpha = 1$ in the estimator without causing any large errors.
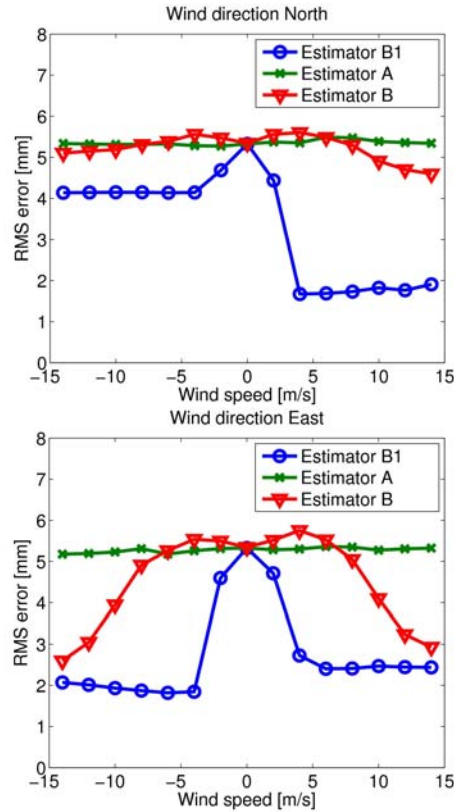

Figure 56   **Accuracy of the MMSE estimators as function of the wind speed as estimated by simulations. Shown are the RMS uncertainty for the three different MMSE estimators.**

We now consider also the accuracy of Estimators B1 and B. For this we investigate the accuracy of the estimated ZWD for stations Borås. The reference Network 1 was used (Ätran, Rörö, Jönköping, and Väne-Åsaka). For the Estimators B1 and B, simulated data from a five hour period (sampled every 15 minutes) prior to the estimated epoch was used. In these simulations we used $k^2 = 1$ mm^2/km and $\alpha = 1$.

Figure 56 shows the result of these simulations. The estimated RMS differences between the ZWD obtained from the MMSE estimators and what was simulated for Borås are plotted as function of the wind velocity. As seen, for wind speeds close to zero there is not much gain in using the temporal information. The reason is that when the wind speed is low the air is not moving very much during five hours. In the case of using Estimator B, the results actually get worse compared to when using Estimator A. For large wind speeds, however, the results are improved compared to Estimator A. The improvement is largest when the wind velocity is known since the wind estimated from the ML estimator will contain errors. We can also see that there is not as much improvement when the wind is blowing in the south direction, compared to when its blowing in north, east or west directions. The reason is that none of the stations are located exactly in the north of Borås, Väne-Åsaka is towards North-North-West. For the other investigated cases there is a station more or less in the up-wind direction from Borås. We can also see that there is

not much improvement when using Estimator B and the wind is towards the North. The reason is probably that the wind estimation is uncertain since we do not have two reference stations on exactly a North-South baseline.
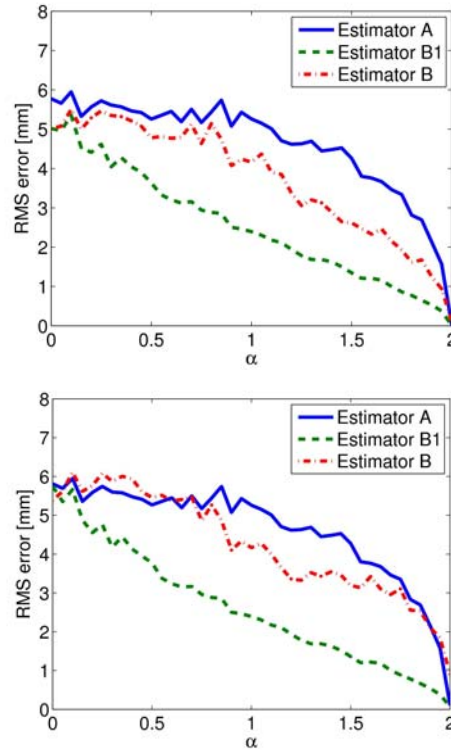

Figure 57   **Accuracy of the three estimators as function of α, when wind is 10 m/s towards east. In the upper panel, the true value of α was used in the estimators, while the lower panel shows the case when $\alpha = 1$ was assumed in the estimators.**

The same network and setup were used in simulations where the value of α was varied. In these simulations the wind was set to 10 m/s in the East direction, and k^2 was chosen such that the RMS ZWD variations over a 50 km baseline is 7 mm (which approximately gives $k^2 = 1$ mm^2/km for $\alpha = 1$). The results can be seen in Figure 57. We show both the case when the true value of alpha is known in the estimators, and the case when the true value is not known and $\alpha = 1$ is assumed. As seen there is not much difference between these two cases for Estimators A and B1. This is in agreement with the results in Figure 55, i.e as long the reference stations are not all in the same direction, assuming $\alpha = 1$ in the estimators will not give any large errors. However, we can see that there is clearly an increase in the error for Estimator B when assuming $\alpha = 1$ compared to knowing the true value. The likely reason for this is that the ML estimation of the wind velocity will be more uncertain if the wrong α value is assumed.
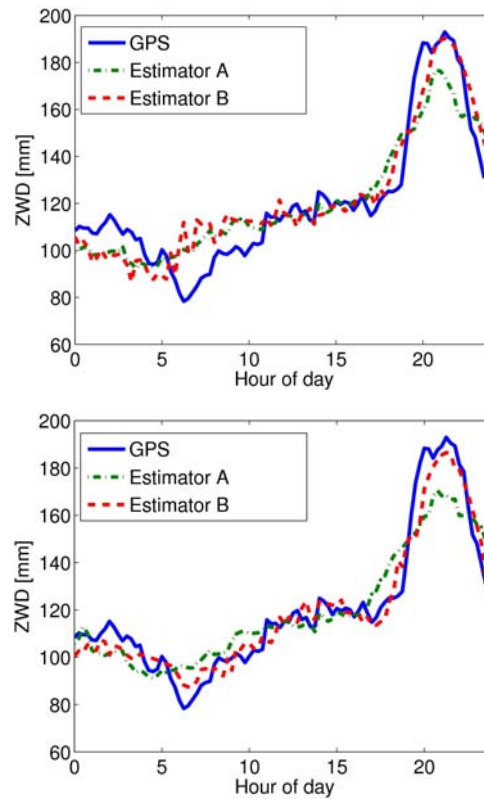
4.4.2   Results

Figure 58   **ZWD on July 10, 2008 for the Borås stations estimated from GPS data from Borås station (GPS), estimated by Estimator A, and estimated by Estimator B. Shown are the results for using data from four (upper) and nine (lower) stations in the MMSE estimators (see text).**

Figure 58 (upper) shows the ZWD for July 10, 2008 (same day as in Figure 54) for the Borås station estimated using GPS data from Borås as well as by MMSE estimators using data from the four surrounding stations Ätran, Rörö, Jönköping, and Väne-Åsaka. We have used both Estimators A and B. Due to the symmetric location of the surrounding stations, Estimator A will more or less estimate the ZWD at Borås as the mean of the ZWD at the surrounding stations. Estimator B includes data from the previous five hours prior to the estimated epoch (sampled every 15 minutes). As seen, the peak at the end of the day is not completely resolved using the Estimator A. When using Estimator B the peak is clearly resolved better. For the earlier epochs of the day the performance of the two estimators are similar. The RMS difference between the MMSE estimators and the ZWD estimated from the GPS data from Borås is 12.3 mm for Estimator A and 11.5 for Estimator B.

Using data from more stations in the estimators may improve the accuracy. In Figure 58 (lower) the results when also including data from the Onsala, Falkenberg, Falköping, Hillerstorp, and Smögen stations. As seen, the peak at the end of the day is still not completely retrieved when using Estimator A, while in the case using Estimator B also the ZWD estimates between 5:00 and 10:00 is improved. The RMS difference between the estimators and the ZWD from the Borås GPS data is now 11.5 mm for Estimator A and 6.9 mm for Estimator B.
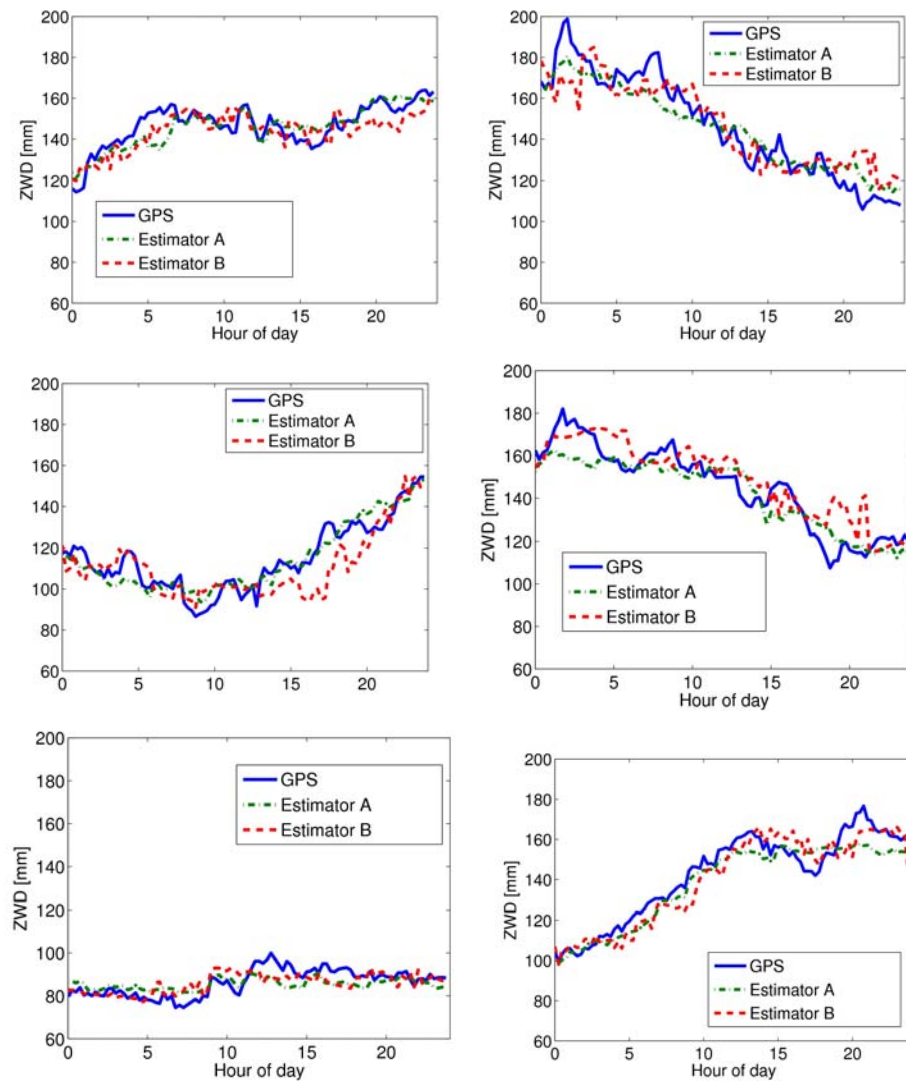
Figure 59   **ZWD for the Borås stations estimated from GPS data from Borås station (GPS), estimated by Estimator A, and by Estimator B using data from. Shown are the results for six days in 2008: July 18 (top, left), 20 (top,right), 21 (right, left), and 22 (middle, right), and August 18 (bottom, left), and 22 (bottom, right).**

Figure 59 shows the accuracy of the estimators for four different days in July 2008 when estimating the ZWD for Borås from the nine surrounding stations. As seen there is typically only small differences between using Estimators A and B. Occasionally there is improvements when using Estimator B, however there are also occasions when Estimator A performs better.
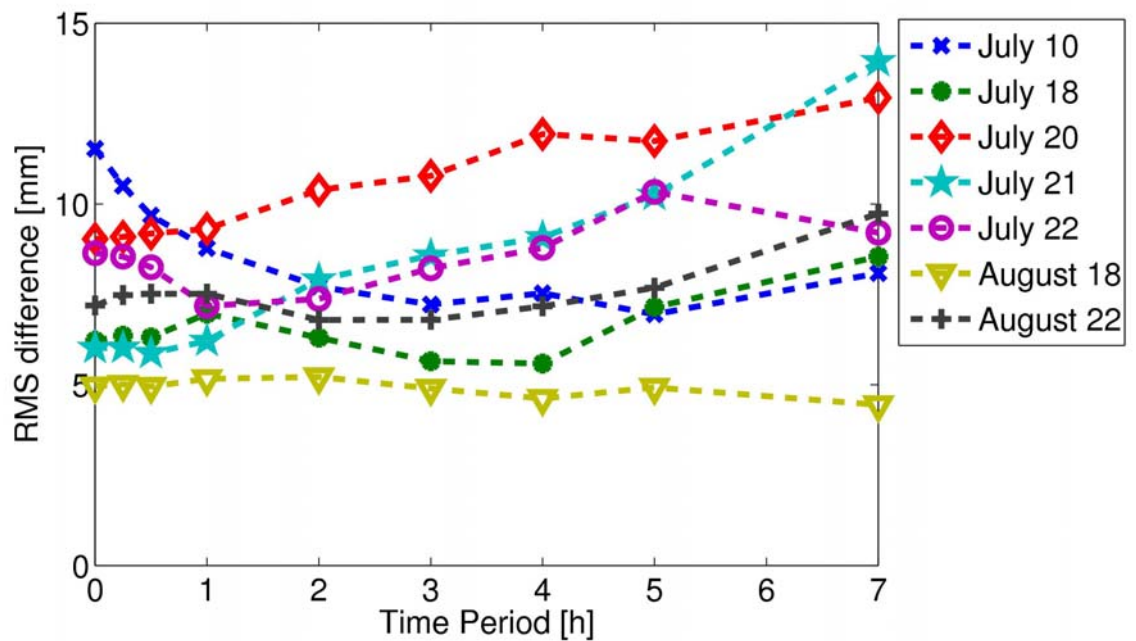
Figure 60   **Accuracy of Estimator B as function of the length of the time period covered by the data from the reference stations. Shown are the results for the same dates as shown in Figure 58 and Figure 59.**

The accuracy of Estimator B will depend upon how long time period the data from the reference stations covers. For short time periods we may not expect that Estimator B performs much better than Estimator A, in fact Estimator B may be less accurate since the estimation of the wind will be very uncertain. Using longer time periods the wind will be estimated more accurately and there will be enough time for the air to move from one station to another, hence we can expect the results to improve. However, for long time periods there may be significant variations in the wind velocity, thus the assumption of constant wind will not hold and Estimator B can not be expected to give accurate results. Figure 60 shows the RMS difference in the ZWD estimated by Estimator B and from GPS data from Borås as function of the length of the time period used. Using a time period of zero hours is equivalent of using Estimator A. As seen, there exist a time period for which Estimator B improves over Estimator A (except for July 20 and 21), however these are different for different days. The reason for this is that the variability of the wind velocity is different for different days.
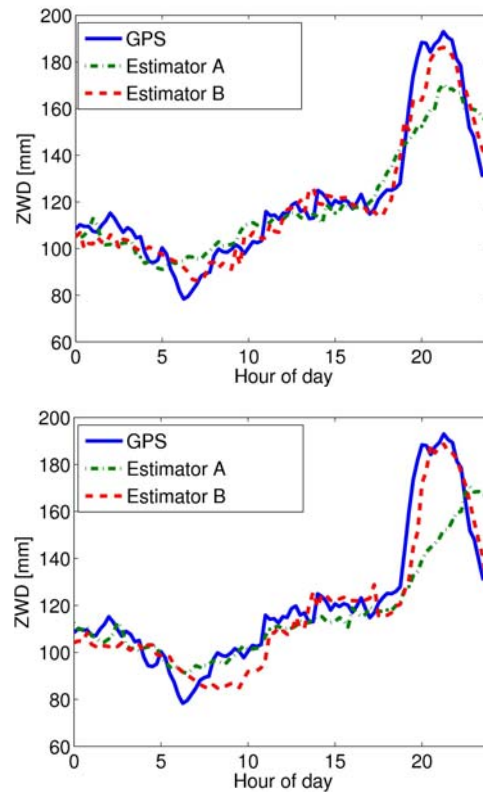
Figure 61   **Same as Figure 58 (lower), but using only data from 30 minutes (upper) and 2 hours (right) prior to the epoch being estimated.**

When using Estimator B it is possible to estimate the ZWD at an epoch different where no data is available from the reference stations. This could be useful in many situations. For example, for real time usage the ZWD from the reference stations may not available in real time, but with a time delay of several minutes up to a few hours. Figure 61 shows the estimation of the ZWD for Borås on July 10, 2008, when using the same 9 reference station as before but assuming that the data from the reference station is available with a delay of 30 minutes (upper panel) and 2 hours (lower panel). Estimator A will in this case estimate the ZWD as the the estimate at last epoch where there is data available. As could be expected, the accuracy of the Estimator A is decreased compared to having the data from the reference stations available in real time, especially when the delay of the data availability is large. The same is true when using the Estimator B, however the degradation of the accuracy is not as large in this case. We can for example see that the peak in the ZWD towards the end of the day still is retrieved relatively well.

4.4.3   Summary
As we have seen, using both temporal and spatial information about the variability of the ZWD can improve the ZWD interpolation compared to when we use only spatial information. The improvement is most clear when there is a clear structure in the ZWD moving across the considered area, like it is in Figure 58. When this is not the case there is no significant improvement to also include temporal variations, in fact the accuracy can even go down in these cases. There are several reasons for this. Firstly, as we have seen in the simulations the accuracy will go down when the wind velocity is low due to uncertainties in the estimation of the wind. Secondly, we assumed that the wind is constant in time, with height and horizontal location, and this assumption may not always be true.

4.5   Contribution using external information

In the previous section, we studied the influence on the results of using temporal information from surrounding reference stations in addition to the spatial information that is normally used in network-RTK. In this section, we study the addition of external information from sensors outside the GPS network. Such information could come from, for example, numerical weather prediction models. Figure 62 shows one example of the effect of including such information in the processing. The figure shows the vertical rms error as a function of the error in the external information used. In the figure is also a straight line showing the vertical error for standard network-RTK processing. For the information to be useful, i.e., to improve the quality of the solution, the error in the troposphere delay information should, hence, be below 6 mm relative the reference stations. Obtaining such accuracy in the external data may be difficult. It is also worth to notice that ground measurements of the humidity will not significantly improve the results due to the low correlation between values measured at the ground and values integrated through the atmosphere.
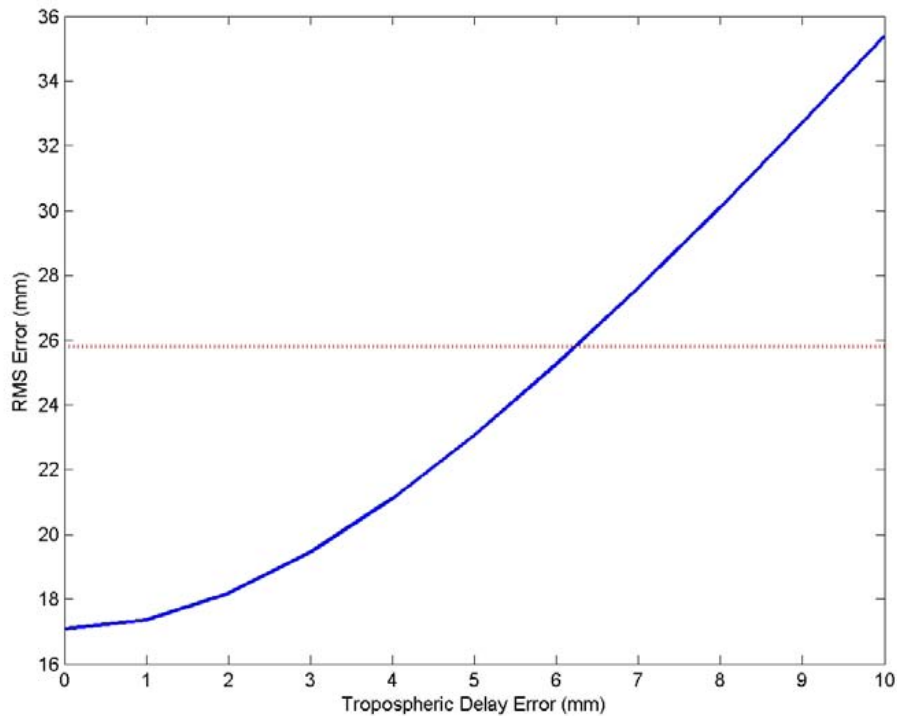

Figure 62   **Vertical rms error as a function of the error in the external information used (blue). Also in the figure (red) is the vertical error for the standard network-RTK processing.**

5   Conclusion

When the future satellite systems Galileo, Compass are complete and can be used in RTK-processing, the optimal choice of elevation cutoff angle changes from approximately 13 degrees today to approximately 25 degrees. The vertical error is reduced from 27 mm to 20 mm for our nominal setup when these future systems can be used. The results using L1 and L3 is relatively similar under nominal conditions. However, for times with a high spatial variability in the ionosphere, the L3 combination will be preferable. A densified network with 35 km between the reference stations results in a similar improvement as the contribution of the new satellite systems. The error in the vertical coordinate is reduced from 27 mm to 20 mm for our nominal setup. Using both a densified network and the new satellite systems reduces the error in the vertical component further down to 14 mm. For dense network, such as distance between the reference stations around 10 km, the vertical error is 11 mm and down to 8 mm for the full future satellite constellation. For such dense network linear combinations of observables at different frequencies can be useful especially for periods with low spatial variability in the ionosphere. Estimation of a local troposphere parameter is, in general, not an advantage for networks with distances between the reference stations of 70 km or less.

Using both temporal and spatial information about the variability of the troposphere can improve the interpolation compared to when we use only spatial information. The improvement is most clear when there is a clear structure in the tropospheric signal moving across the considered area

6   References

Alves P., I. Geisler, N. Brown, J. Wirth, and H.-J. Euler, Introduction of a geometry based network RTK quality indicator, *Proceedings of ION GNSS 2005*, pp. 2552–2563, 2005.
http://www.leica-geosystems.com/corporate/en/downloads/lgs_page_catalog.htm?cid=5272

Brown N., R. Keenan, B. Richter, and L. Troyer, Advances in ambiguity resolution for RTK applications using the new RTCM V3.0 Master-Auxiliary messages, *Proceedings of ION GNSS 2005*.
http://www.leica-geosystems.com/corporate/en/downloads/lgs_page_catalog.htm?cid=5271

Brown N., I. Geisler, and L. Troyer, RTK Rover Performance using the Master Auxiliary Concept, *Journal of Global Positioning Systems, 5 (1-2)*, pp. 135–144, 2006.
http://www.gmat.unsw.edu.au/wang/jgps/v5n12/v5n12p21.pdf

Chen X., H. Landau, and U. Vollath, New tools for Network RTK Integrity monitoring, *Proceedings of ION,* 2003.
http://www.trimble.com/survey_wp.asp?Nav=Collection-27601

Emardson T.R., and J.M. Johansson, Spatial interpolation of the atmospheric water vapor content between sites in a ground-based GPS network, *Geophys. Res. Lett., 25 (17)*, pp. 3347–3350, 1998.
doi:10.1029/98GL02504.

Emardson T.R., and F.H. Webb, Estimating the motion of atmospheric water vapor using the Global Positioning System, *GPS Solutions, 6*, pp. 58–64, 2002.
doi:10.1007/s10291-002-0012-8.

Emardson T.R., and P.O.J. Jarlemark, Optimal linear combinations of GNSS observables, *in preparation*, 2009.

Euler H.-J., Reference Station Network Information Distribution, *IAG Working Group 4.5.1: Network RTK*, 2008.
http://www.network-rtk.info

Goad C., and L. Goodman, A modified Hopfield Tropospheric Refraction Correction Model, *Proceedings of AGU Fall Meeting*, 1974.

GUM, JCGM WG1 GUM – Guide to the Expression of Uncertainty in Measurement, JCGM 100:2008.
http://www.bipm.org/en/publications/guides/gum.html.

Hoffman-Wellenhof B., H. Lichtenegger, and J. Collins, GPS: Theory and practice, *Springer Verlag, New York,* 1994.

IGS
http://igscb.jpl.nasa.gov/components/prods.html

Jarlemark P.O.J., Analysis of temporal and spatial variation in atmospheric water vapour using microwave radiometry, *PhD thesis, Chalmers Univ. of Tech.*, 1997.

Johnsson F., and M. Wallerström, A network-RTK comparison between GPS and GPS/GLONASS, En nätverks-RTK-jämförelse mellan GPS och GPS/GLONASS, (in Swedish), *LMV-rapport 2007:1*, 2007.
http://www.lantmateriet.se/templates/LMV_Page.aspx?id=2688

Kay S.M., Fundamentals of Statistical Signal Processing: Estimation Theory, *Prentice Hall, New Jersey,* 1993.

Klobuchar J.A., Ionospheric Effects on GPS, in *Global Positioning System: Theory and Applications*, *1*, eds: B. W. Parkinson and J. J. Spilker, pp. 485-514, 1996.

Kolb P.F., X. Chen, and U. Vollath, A new method to model the ionosphere across local area networks, 2005.
http://www.trimble.com/survey_wp.asp?Nav=Collection-37457

Landau H., U. Vollath, and X. Chen, Virtual reference stations versus broadcast solutions in network RTK- advantages and limitations, *Proceedings of GNSS 2003*.
http://www.trimble.com/survey_wp.asp?Nav=Collection-27603

Nilsson T., L. Gradinarsky, and G. Elgered, Correlations between slant wet delays measured by microwave radiometry, IEEE Trans. Geosci. Remote Sensing, 43 (5), pp. 1028–1035, 2005.
doi:10.1109/TGRS.2004.840659.

Nilsson T., R. Haas, and G. Elgered, Simulations of atmospheric path delays using turbulence models, in *Proc. of the 18th EVGA Working Meeting*, eds: J. Böhm, A. Pany, and H. Schuh, pp. 175–180, 2007.

Nilsson T., Measuring and modelling variations in the distribution of atmospheric water vapour using GPS, *PhD thesis, Chalmers Univ of Tech.*, 2008.

Takac F., and W. Lienhart, SmartRTK: A Novel Method of Processing Standardised RTCM Network RTK Information for High Precision Positioning, *ENC GNSS*, 2008.
http://www.leica-geosystems.com/corporate/en/downloads/lgs_page_catalog.htm?cid=9568

Treuhaft R.N., and G.E. Lanyi, The effects of the dynamic wet tropophereon radio interferometic measurements, *Radio Sci., 22*, pp. 251-265, 1987.

Saastamoinen J., Atmospheric corrections for the troposphereand stratospherein radio ranging of satellites, *The use of artificial satellites for Geodesy, Geophys. Monogr. Seriesvol 15*, ed: S. W. Henriksen et al, pp. 247-251, AGU, Washington, D. C., 1972.

Topcon, TopSURV Controller Software, 2007.
http://www.topconeurope.com/index.asp?pageid=c77f48949b804c4dbc81bf32f3036099

Trimble, Support of Network Formats by Trimble GPSNet Network RTK Solution, 2005.
http://www.trimble.com/survey_wp_scalable.asp?Nav=Collection-33413

VIM 2008 International vocabulary of metrology - Basic and general concepts and associated terms (VIM), Joint *Committee on Guides in Metrology (JCGM)*, 2008.
http://www.bipm.org/en/publications/guides/vim.html,
http://www.bipm.org/utils/common/documents/jcgm/JCGM_200_2008.pdf

7 Appendix I

7.1 Part A1.1

In order to quantify the network RTK wet delay modelling error (see A1.2) we need to derive an expression for the covariances of the wet delay differences. This can be done by expressing the wet delay as integral of the wet refractivity, χ. The structure function for the wet refractivity at two locations r_a and r_b is

$$D_\chi(r_a, r_b) = [def] = E\{(\chi(r_a) - \chi(r_b))^2\} \tag{A1}$$

For this quantity established models exist.

We now write the slant wet delay as an integral of the wet refractivity:

$$l_1^i = \int \chi(r_1^i(l))dl = m^i \int \chi(r_1^i(v))dv \tag{A2}$$

where we have parameterized the position vector, r, along the vertical, v, using the wet delay mapping function, m, as scaling between the differentials. The east, north and vertical components of the position vector is then

$$r_1^i(v) = [v \cdot \sin\phi_1^i / \tan\varepsilon_1^i, v \cdot \cos\phi_1^i / \tan\varepsilon_1^i, v] \tag{A3}$$

where ϕ is the azimuth angle and ε the elevation angle.

Let $l_1^i - l_2^i$ be the slant wet delay difference between two sites, *1* and *2*, (e.g. a rover and a reference station) along the paths towards satellite *i*.

The slant wet delay differences to satellite *i* and *j* has the following relation:

$$
\begin{aligned}
&(l_1^i - l_2^i) \cdot (l_1^j - l_2^j) = \\
&m^i \cdot \int (\chi(r_1^i(v)) - \chi(r_2^i(v)))dv \cdot m^j \cdot \int (\chi(r_1^j(v')) - \chi(r_2^j(v')))dv' = \\
&m^i m^j \cdot \iint (\chi(r_1^i(v)) - \chi(r_2^i(v))) \cdot (\chi(r_1^j(v')) - \chi(r_2^j(v')))dvdv' = \\
&= [see\_below] = \\
&\tfrac{1}{2}m^i m^j \iint [-(\chi(r_1^i(v)) - \chi(r_1^j(v')))^2 + (\chi(r_1^i(v)) - \chi(r_2^j(v')))^2 + \\
&+ (\chi(r_2^i(v)) - \chi(r_1^j(v')))^2 - (\chi(r_2^i(v)) - \chi(r_2^j(v')))^2]dvdv'
\end{aligned}
\tag{A4}
$$

where we used the following equation:

$$(a-b) \cdot (c-d) = \tfrac{1}{2} \cdot [-(a-c)^2 + (a-d)^2 + (b-c)^2 - (b-d)^2] \tag{A5}$$

We can now write the covariances of the slant wet delay differences as:

$$E\{(l_1^i - l_2^i) \cdot (l_1^j - l_2^j)\} =$$

$$\tfrac{1}{2}m^i m^j E\{\iint[-(\chi(r_1^i(v)) - \chi(r_1^j(v')))^2 + (\chi(r_1^i(v)) - \chi(r_2^j(v')))^2 +$$

$$+ (\chi(r_2^i(v)) - \chi(r_1^j(v')))^2 - (\chi(r_2^i(v)) - \chi(r_2^j(v')))^2]dvdv'\} =$$

$$= [f_\chi \in nice] =$$

$$\tfrac{1}{2}m^i m^j \iint E\{-(\chi(r_1^i(v)) - \chi(r_1^j(v')))^2 + (\chi(r_1^i(v)) - \chi(r_2^j(v')))^2 + \quad\quad\quad\text{(A6)}$$

$$+ (\chi(r_2^i(v)) - \chi(r_1^j(v')))^2 - (\chi(r_2^i(v)) - \chi(r_2^j(v')))^2 \}dvdv' =$$

$$= [def] =$$

$$\tfrac{1}{2}m^i m^j \iint[-D_\chi(r_1^i(v), r_1^j(v')) + D_\chi(r_1^i(v), r_2^j(v')) +$$

$$+ D_\chi(r_2^i(v), r_1^j(v')) - D_\chi(r_2^i(v), r_2^j(v'))]dvdv'$$

where we have used the knowledge that the distribution function of the wet refractivity is "nice" enough that we can change order between taking the expectation value and vertical integration. We have also used the definition of the wet refractivity structure function D_χ :

$$D_\chi(r_a, r_b) = [def] = E\{(\chi(r_a) - \chi(r_b))^2\} \quad\quad\quad\text{(A8)}$$

We model D_χ as only dependant on the distance $d_{ab} = |\ r_a - r_b\ |$:

$$D_\chi(r_a, r_b) = C_\chi^2 \cdot d_{ab}^\alpha \quad\quad\quad\text{(A9)}$$

when the vertical components v_a and v_b are both < 1000 m. $D_\chi = 0$ otherwise.

We use $\alpha = 0.9$ and $C_\chi^2 = 5.57 \cdot 10^{-15} m^{-0.9}$

7.2   Part A1.2

In network RTK we use, l_n^i, a weighted sum of the slant wet delays of the network reference stations

$$l_n^i = \sum w_p \, l_p^i \tag{A10}$$

to model the rover slant wet delay, l_r^i, in the direction of satellite i. $\sum w_p = 1$.

The model error can be written as

$$l_r^i - l_n^i = \sum_p w_p (l_r^i - l_p^i) \tag{A11}$$

To write the wet delay error covariance we start by multiplying errors:

$$(l_r^i - {}_n^i) \cdot (l_r^j - {}_n^j) = \sum_p \sum_q w_p w_q \cdot (l_r^i - l_p^i) \cdot (l_r^j - {}_q^j) =$$

$$[change\_summation\_order] =$$

$$\sum_p \sum_q w_p w_q \cdot (l_r^i - l_q^i) \cdot (l_r^j - {}_p^j) = \tag{A12}$$

$$[combine\_the\_two\_summations] =$$

$$\tfrac{1}{2} \cdot \sum_p \sum_q w_p w_q \cdot [(l_r^i - l_p^i) \cdot (l_r^j - {}_q^j) + (l_r^i - l_q^i) \cdot (l_r^j - {}_p^j)]$$

By rewriting the expression in brackets:

$$[(l_r^i - l_p^i) \cdot (l_r^j - {}_q^j) + (l_r^i - l_q^i) \cdot (l_r^j - {}_p^j)] =$$

$$[(l_r^i - l_p^i) \cdot (l_r^j - {}_p^j) + (l_r^i - l_q^i) \cdot (l_r^j - {}_q^j) - (l_p^i - l_q^i) \cdot (l_p^j - {}_q^j)] \tag{A13}$$

we obtain

$$(l_r^i - {}_n^i) \cdot (l_r^j - {}_n^j) = \tfrac{1}{2} \sum_p \sum_q w_p w_q \cdot (l_r^i - l_p^i) \cdot (l_r^j - {}_p^j) +$$

$$\tfrac{1}{2} \sum_p \sum_q w_p w_q \cdot (l_r^i - l_q^i) \cdot (l_r^j - {}_q^j) - \tfrac{1}{2} \sum_p \sum_q w_p w_q \cdot (l_p^i - l_q^i) \cdot (l_p^j - {}_q^j) =$$

$$\tfrac{1}{2} \sum_p w_p \cdot (l_r^i - l_p^i) \cdot (l_r^j - {}_p^j) + \tag{A14}$$

$$\tfrac{1}{2} \sum_q w_q \cdot (l_r^i - l_q^i) \cdot (l_r^j - {}_q^j) - \tfrac{1}{2} \sum_p \sum_q w_p w_q \cdot (l_p^i - l_q^i) \cdot (l_p^j - {}_q^j) =$$

$$\sum_p w_p \cdot (l_r^i - l_p^i) \cdot (l_r^j - {}_p^j) - \tfrac{1}{2} \sum_p \sum_q w_p w_q \cdot (l_p^i - l_q^i) \cdot (l_p^j - {}_q^j)$$

The error covariance for observations of satellites i and j can now be written as:

$$E\{(l_r^i - {}_n^i) \cdot (l_r^j - {}_n^j)\} =$$

$$\sum_p w_p \cdot E\{(l_r^i - l_p^i) \cdot (l_r^j - {}_p^j)\} - \tfrac{1}{2} \sum_p \sum_q w_p w_q \cdot E\{(l_p^i - l_q^i) \cdot (l_p^j - {}_q^j)\} \tag{A15}$$

where we calculate the components $E\{(l_r^i - l_p^i) \cdot (l_r^j - {}_p^j)\}$ and $E\{(l_p^i - l_q^i) \cdot (l_p^j - {}_q^j)\}$ according to A1.1

8   Appendix II

Paper: Optimal linear combination of GNSS observables

Optimal linear combination of GNSS observables

Ragne Emardson and Per Jarlemark

SP Technical Research Institute of Sweden
+46105165727
+46105165620
ragne.emardson@sp.se
www.sp.se

Today, many GPS receivers can receive signals at two frequencies, L1 and L2. By forming a linear combination of the observed signals at the two frequencies a third observable may be formed. One common combination is known as L3. The purpose of this combination is to form an observable that is to a large extent insensitive to signal variations in the ionosphere. Another common example is to use L1 only which may be used for short baselines where ionospheric variations to a large extent are cancelled when differencing observations. Hence the less noisy observable L1 is used solely. A future GPS system will transmit signals on three frequencies in addition to the two described above also on L5. Also Galileo will transmit on three different frequencies. In this paper we present expressions for the linear combinations of observables optimized for different measurement conditions regarding ionospheric variability and receiver measurement noise. We present such models for the present two-frequency GPS constellation and a future three-frequency GPS as well as Galileo system. Using our new model for the two-frequency GPS constellation, we can have an improvement of almost 15% in the horizontal component compared to the best performing of the two standard combinations.

Introduction

The number of applications using the GPS technique grows steadily. Many of these applications use stand alone GPS receivers. However, there are also a large number of applications that utilize different support systems that are available today. These support systems are developed to achieve better accuracy in the GPS estimates and are usually based on some sort of relative measurements. The general idea with the support systems is to receive GNSS-signals at a stationary reference with known position coordinates and to use these to correct position data at a roving receiver in another location. The large benefit with these systems is that the roving and reference antenna can receive the signals from the same satellites with similar directions to the satellites. Hence, the errors are to a large extent cancelled when differencing the observations. Different types of support systems exist and are used today with GPS. The method often referred to as Differential GPS (DGPS) is based on the pseudorandom code observables [e.g., Gauthier et al., 2001] while Real Time Kinematic (RTK) is based on the carrier phase observables [e.g., Rizos, 2002]. In this paper, we focus on the RTK concept.

Today, many GPS receivers can receive signals at two frequencies denoted L1 and L2. By forming a linear combination of the observed signals at the two frequencies a third observable may be formed. This new observable is then used when processing the observations in order to estimate the sought parameters, such as actual position of the GPS receiver. One common combination is 2.55*L1-1.55*L2 which is known as L3 [e.g., Hoffman-Wellenhof et al, 1998]. The main purpose of this combination is to form an observable that is to a large extent insensitive to signal variations in the ionosphere. It is based on the assumption that the ionospheric effect is inversely proportional to the frequency squared. Another common example is 1*L1+0*L2 which is suitable for short baselines where ionospheric variations to a large extent are cancelled when differencing observations. Hence the less noisy observable L1 can be used solely.

Today the GPS constellation transmits signals on L1 at 1575.42 MHz and L2 on 1227.6 MHz. In a near future GPS will introduce signals on a third frequency L5 on 1176.45 MHz. Furthermore, the Galileo system will be deployed; transmitting signals on the L1, E5, and E6 frequency bands. In this paper, we present a method to find optimal linear combinations of the observations from these satellite systems. We also exemplify the method by determining the weights for the optimal combinations.

Modeling

In order to find optimal combinations of the observables, we model the received signal phase by GNSS receiver number 1 at frequency ϕ_n^1 as:

$$\ell_n^1 = \ell^1 + \xi_n g^1 + w_n^1 + \ell_A^1 + \ell_c^t + \ell_c^{r1} + \lambda_n N_n^1$$

Here ℓ_n^1 is the received phase at the frequency, ϕ_n, times the wavelength, λ_n

$$\ell_n^1 = \phi_n^1 \cdot \lambda_n$$

ℓ^1 is the true geometrical distance between the satellite and the receiving antenna, g^1 is a frequency independent measurement of the ionospheric thickness, ξ_n is the frequency dependent scaling and w_n^1 is receiver measurement noise and the local multipath, ℓ_A^1 is the signal delay in the neutral atmosphere, ℓ_c^t is the satellite clock error, ℓ_c^{r1} is the local clock error, and N_n^1 is an a priori unknown number of wavelengths.

Forming the difference between the observed signals at the rover, 1, and the reference station, 2, such as:

$$\ell_n = \ell_n^1 - \ell_n^2$$

we obtain an observable that can be used for determining the vector between the rover and reference position. Here, we assume that N is resolved. The local clock differences are identical for all satellite observations and are easily estimated when processing the observed measurements and are thus neglected in this work. We can now write the differenced observable as

$$\ell_n = \ell + \xi_n g + w_n + \ell_A$$

and the variance of the receiver noise difference and multipath difference is

$$\sigma_n^2 = Var[w_n]$$

and

$$\sigma_A^2 = Var[\ell_A].$$

By receiving signals at different frequencies, we can form a linear combination of these observables ℓ_n at the different frequencies as:

$$\hat{\ell} = a\ell_1 + b\ell_2 + c\ell_3$$

This linear combination is then used for the estimation of the sought parameters. We can now choose the parameters *a*, *b*, and *c* depending on our observing situation. In the next sections, we estimate optimal parameters for a two and three-frequency satellite navigation system by minimizing the variance in $\hat{\ell}$.

Parameter Estimation

Two-frequency combination

The current GPS satellites transmit signals on two different frequencies, L1 and L2. According to equation 8, we can write the linear combination of the observables at these two frequencies as:

$$\hat{\ell} = a\ell_1 + b\ell_2$$

In order to find useful linear combinations of the observables at these frequencies, that is values for the weights *a* and *b*, we seek *a* and *b* so that

$$E[\hat{\ell} - \ell] = 0$$

and the variance of $\hat{\ell}$- ℓ

$$Var[\hat{\ell} - \ell]$$

is minimized. We can write

$$E[\hat{\ell} - \ell] = aE[\ell_1] + bE[\ell_2] - \ell = 0$$

Assuming that the expected contribution from the ionosphere, the neutral atmosphere, and the receiver measurement noise to the observed signal is identical for both the rover and reference station, we obtain *a+b=1*. Forming the variance as

$$H = Var[\hat{\ell} - \ell] = a^2 Var[\ell_1 - \ell] + b^2 Var[\ell_2 - \ell] + 2ab E[(\ell_1 - \ell)(\ell_2 - \ell)] =$$
$$a^2 \xi_1^2 g^2 + a^2 \sigma_1^2 + b^2 \xi_2^2 g^2 + b^2 \sigma_2^2 + 2ab(\xi_1 \xi_2 g^2 + \sigma_1 \sigma_2 \chi) + \sigma_A^2$$

where we have used equation (4) and equation (9). Here χ is the correlation between the noise parameters w_1 and w_2. By setting $\partial H / \partial a = 0$ and *a+b=1*, we can solve for the parameters *a* and *b* that minimizes the variance in *H*. The solution to this equation is:

$$a = \frac{\xi_2^2 g^2 + \sigma_2^2 - \xi_1 \xi_2 g^2 + \sigma_1 \sigma_2 \chi}{\xi_1^2 g^2 + \sigma_1^2 + \xi_2^2 g^2 + \sigma_2^2 - 2\xi_1 \xi_2 g^2 + 2\sigma_1 \sigma_2 \chi}$$

and

$$b = 1 - \frac{\xi_2^2 g^2 + \sigma_2^2 - \xi_1 \xi_2 g^2 + \sigma_1 \sigma_2 \chi}{\xi_1^2 g^2 + \sigma_1^2 + \xi_2^2 g^2 + \sigma_2^2 - 2\xi_1 \xi_2 g^2 + 2\sigma_1 \sigma_2 \chi}$$

We can now make a few assumptions in order to calculate a and b. By assuming measurement values for the noise parameters as $\sigma_1 = \sigma_{0,1} / \sin(elevation)$ and $\sigma_2 = \sigma_{0,2} / \sin(elevation)$ where $\sigma_{0,1}$ and $\sigma_{0,2}$ is equal to 2.4mm and 2.9 mm respectively [Emardson et al., 2009]. We also assume zero correlation between the measurements noise on the two frequencies, $\chi = 0$. By now using the Klobuchar model [Klobuchar, 1996] for the ionosphere variation with distance, see Figure 63, and assuming a first order ionospheric effect on the received GPS signals, we can calculate a as a function of distance between the GNSS antennas for a certain satellite constellation. Figure 63 shows a as a function of distance between the antennas for observations with three different elevation angles to the satellite. In the figure is also shown the ionospheric effect on the L1 frequency calculated using the Klobuchar model for December 17, 2007 for the location 60° North and 15° East.
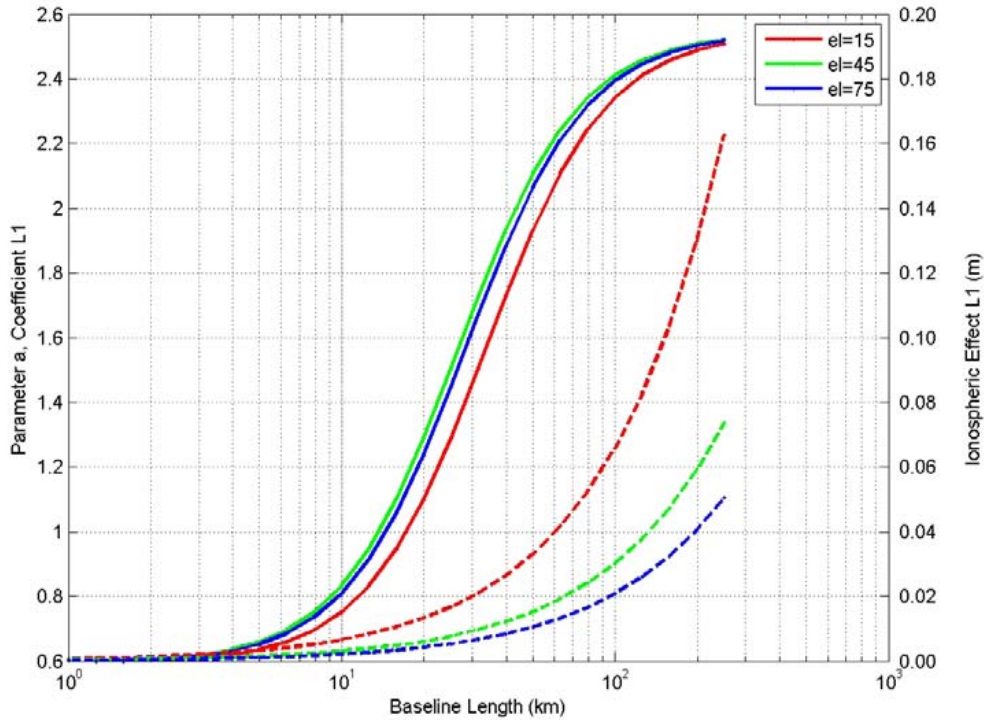

Figure 63   Values for the parameter a together with the ionospheric effect on L1. The values are presented for three different choices of elevation angles, namely 15, 45, and 75 degrees in south direction.

The figure clearly shows that for short baselines, i.e., distances less than or equal to 1 km, we should chose a=0.61 and b=0.39. For such short distances, the contribution from the

ionosphere is negligible. For long baselines, i.e., distances larger than 100 km, the parameters approach $a=2.55$ and $b=-1.55$ which is the standard linear combination of the observables on L1 and L2 forming the ionosphere independent L3 combination. For intermediate baselines, i.e., between 1 and 100 km, there is a smooth transition between the reported values. Interesting to note is that for baselines of about 15 km, the optimal solution for a is equal to one. As a consequence the value for b is zero. Hence the optimal solution is to use only the L1 observable in the parameter estimation process.

Using the values we find for a and b for different baseline lengths, we can calculate the variance H of the combined observable. Figure 64 and Figure 65 show the variance H of a combination of two GPS observables at 15° and 75° elevation angle respectively as function of baseline length. In the figures, H is shown for the combination derived in this paper using the values for a and b that minimizes the variance for elevation angles 15 and 75 degrees respectively, for L1 only observations only, and for the standard L3 combination. We have used the same assumed values on the noise parameters, ionosphere variability as earlier. We have also assumed a neutral atmosphere variability as described in [Emardson et al., 2009]
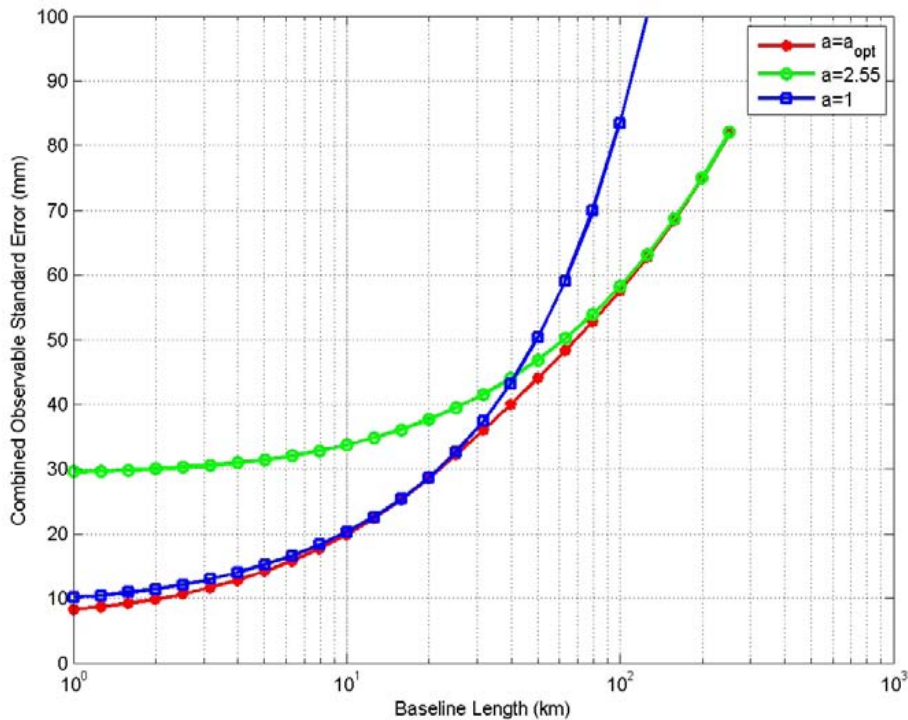

Figure 64   The variance H of a combination of two GPS observables at 15 degrees elevation angle as a function of baseline length. H is shown for the combination derived in this paper (stars), L1 only (squares), and L3 (circles).
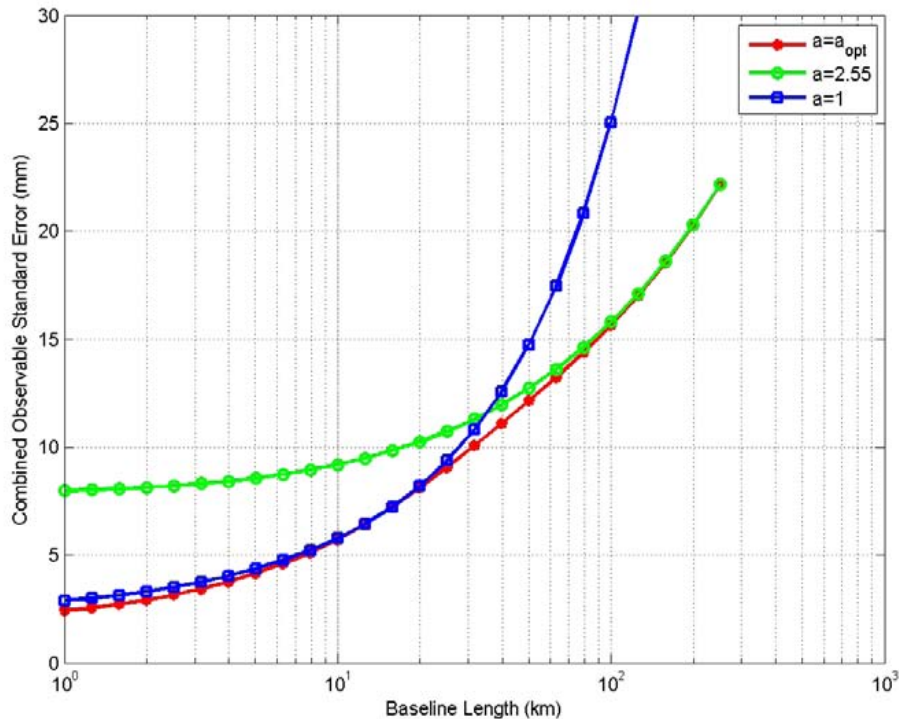
Figure 65   The variance H of a combination of two GPS observables at 75 degrees elevation angle as a function of baseline length. H is shown for the combination derived in this paper (stars), L1 only (squares), and L3 (circles).

The optimal solution agrees well with the L1 only solution for baselines around 10 km and with the L3 combination for baselines longer than 100 km. For distances between 10 and 100 km we can have an improvement of almost 20% when choosing the combination presented in this paper compared to the more appropriate of the two others.

We can now use the results obtained in order to study the effect on the estimated position. Under the same assumptions as before on receiver noise and ionospheric and neutral atmospheric variability together with satellite constellation, we can estimate position error as function of baseline length. We used the satellite constellation for December 17, 2007 at noon as seen from for the location 60° North and 15° East. The horizontal and vertical position error was calculated. The calculation was performed for different baseline lengths between the rover and reference station. For each baseline optimal a and b parameters were derived. These parameters were calculated, for each baseline, as mean values of the individual a and b parameters for each observation.
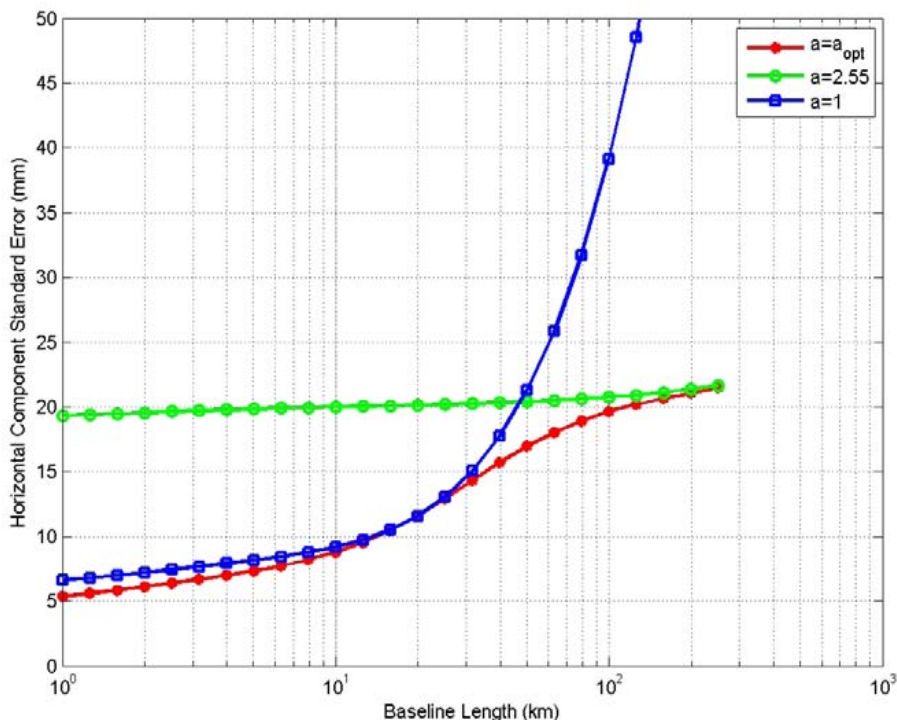
Figure 66   **Estimated position error in the horizontal component as function of baseline length.**
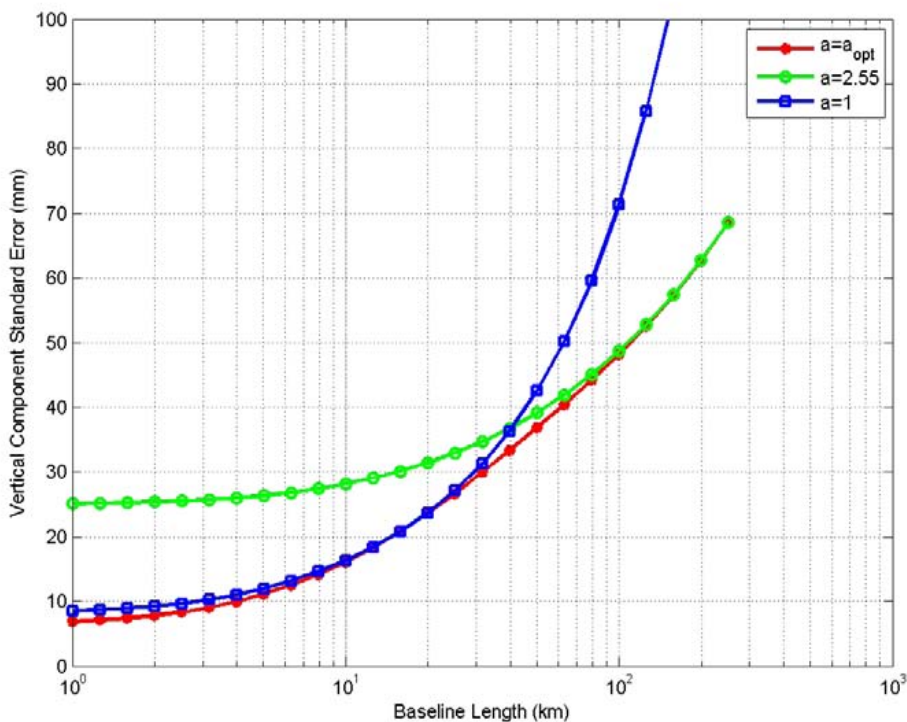

Figure 67   **Estimated position error in the vertical component as function of baseline length.**

The optimal solution agrees well with the L1 only solution for baselines around 10 km and with the L3 combination for baselines longer than 100 km. For distances between 10

and 100 km we can have an improvement of almost 15% in the horizontal component when choosing the combination presented in this paper compared to the more appropriate of the two others. The improvement is less significant for the vertical component.

Three-frequency combination

A third frequency, L5, will be introduced in the GPS. Also the Galileo system will transmit signals at three different frequencies. According to eq 7, we can write the linear combination of the observables at these two frequencies as:

$$\hat{\ell} = a\ell_1 + b\ell_2 + c\ell_3$$

An optimal linear combination of observables at three frequencies can be found. Following the procedure for the two frequency calculations we have

$$
\begin{aligned}
H = Var[\hat{\ell} - \ell] &= a^2 Var[\ell_1 - \ell] + b^2 Var[\ell_2 - \ell] + c^2 Var[\ell_3 - \ell] + \\
&2abE[(\ell_1 - \ell)(\ell_2 - \ell)] + 2acE[(\ell_1 - \ell)(\ell_3 - \ell)] + 2bcE[(\ell_2 - \ell)(\ell_3 - \ell)] = \\
&a^2 \xi_1^2 g^2 + a^2 \sigma_1^2 + b^2 \xi_2^2 g^2 + b^2 \sigma_2^2 + c^2 \xi_3^2 g^2 + c^2 \sigma_3^2 + \\
&2ab(\xi_1\xi_2 g^2 + \sigma_1\sigma_2\chi) + 2ac(\xi_1\xi_3 g^2 + \sigma_1\sigma_3\chi) + 2bc(\xi_2\xi_3 g^2 + \sigma_2\sigma_3\chi) + \sigma_A^2
\end{aligned}
$$

$\partial H / \partial a = 0$, $\partial H / \partial a = 0$, and $a+b+c=1$. By solving for a and b, we obtain

$$a = \frac{\sigma_1\sigma_3\chi_2\xi_2^2 - g^2\xi_3\sigma_1\sigma_2\chi_1\xi_2 - g^2\xi_1\sigma_2\sigma_3\chi_3\xi_2 + g^2\xi_1\xi_3\sigma_2^2 + \sigma_1\sigma_2^2\sigma_3\chi_2 - \sigma_1\sigma_2^2\sigma_3\chi_1\chi_3}{q_a}$$

where

$$
\begin{aligned}
q_a &= f\sigma_2^2\xi_1^2 - f\sigma_2\sigma_3\chi_3\xi_1^2 - f\xi_3\sigma_2^2 c_1 - 2g^2\xi_2\sigma_1\sigma_2\chi_1\xi_1 + g^2\xi_3\sigma_1\sigma_2\chi_1\xi_1 + g^2\xi_2\sigma_1\sigma_3\chi_2\xi_1 + \\
&g^2\xi_2\sigma_2\sigma_3\chi_3\xi_1 + f\xi_2^2\sigma_1^2 - g^2\xi_2\xi_3\sigma_1^2 + \sigma_1^2\sigma_2^2 - \sigma_1^2\sigma_2^2\chi_1^2 + g^2\xi_2\xi_3\sigma_1\sigma_2\chi_1 - \sigma_1\sigma_2^2\sigma_3\chi_2 - \\
&g^2\xi_2^2\sigma_1\sigma_3\chi_2 + \sigma_1^2\sigma_2\sigma_3\chi_1\chi_2 - \sigma_1^2\sigma_2\sigma_3\chi_3 + \sigma_1\sigma_2^2\sigma_3\chi_1\chi_3
\end{aligned}
$$

and

$$b = \frac{g^2\sigma_2\sigma_3\chi_3\xi_1^2 - g^2\xi_3\sigma_1\sigma_2\chi_1\xi_1 - g^2\xi_2\sigma_1\sigma_3\chi_2\xi_1 + g^2\xi_2\xi_3\sigma_1^2 - \sigma_1^2\sigma_2\sigma_3\chi_1\chi_2 + \sigma_1^2\sigma_2\sigma_3\chi_3}{q_b}$$

where

$$
\begin{aligned}
q_b &= g^2\sigma_2^2\xi_1^2 - g^2\sigma_2\sigma_3\chi_3\xi_1^2 - g^2\xi_3\sigma_2^2 c_1 - 2g^2\xi_2\sigma_1\sigma_2\chi_1\xi_1 + \\
&g^2\xi_3\sigma_1\sigma_2\chi_1\xi_1 + g^2\xi_2\sigma_1\sigma_3\chi_2\xi_1 + g^2\xi_2\sigma_2\sigma_3\chi_3\xi_1 + g^2\xi_2^2\sigma_1^2 - g^2\xi_2\xi_3\sigma_1^2 + \\
&\sigma_1^2\sigma_2^2 - \sigma_1^2\sigma_2^2\chi_1^2 + g^2\xi_2\xi_3\sigma_1\sigma_2\chi_1 - \sigma_1\sigma_2^2\sigma_3\chi_2 - g^2\xi_2^2\sigma_1\sigma_3\chi_2 + \\
&\sigma_1^2\sigma_2\sigma_3\chi_1\chi_2 - \sigma_1^2\sigma_2\sigma_3\chi_3 + \sigma_1\sigma_2^2\sigma_3\chi_1\chi_3
\end{aligned}
$$

We calculate *a, b* and *c* as a function of baseline distance in analogy with the parameter determination for the two-frequency case. In addition to the measurement values for the noise parameters $\sigma_1 = \sigma_{0,1}/\sin(elevation)$ and $\sigma_2 = \sigma_{0,2}/\sin(elevation)$ where $\sigma_{0,1}$ and $\sigma_{0,2}$ is equal to 2.4mm and 2.9 mm respectively, we assume $\sigma_{0,3} = 2.4$ mm and the same elevation dependence. We also assume zero correlation between the measurements noise on all frequencies, $\chi_1 = \chi_2 = \chi_3 = 0$. We use the Klobuchar model [Klobuchar, 1996] for the ionosphere variation with distance, see Figure 63, and assume a first order ionospheric effect on the received GNSS signals. Figure 68, Figure 69, and Figure 70shows *a, b , and c* as functions of distance between the GNSS antennas for observations with three different elevation angles to the satellite. In the Figure 68 is also shown the ionospheric effect on the L1 frequency calculated using the Klobuchar model for December 17, 2007 for the location 60° North and 15° East.
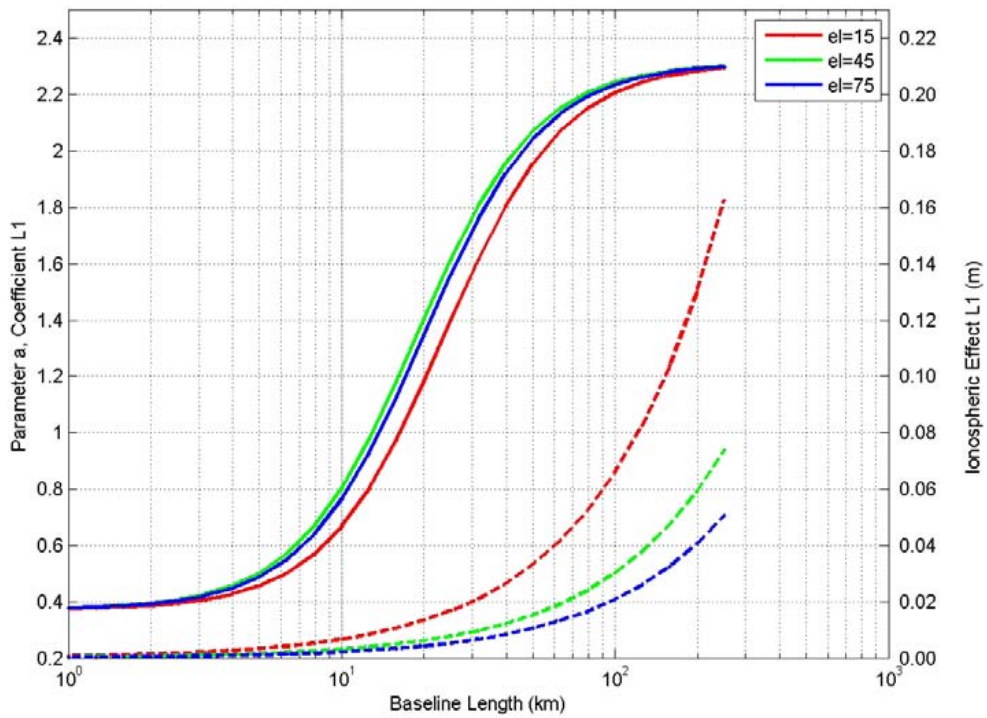

Figure 68 **Values for the parameter a together with the ionospheric effect on L1. The values are presented for three different choices of elevation angles, namely 15, 45, and 75 degrees.**
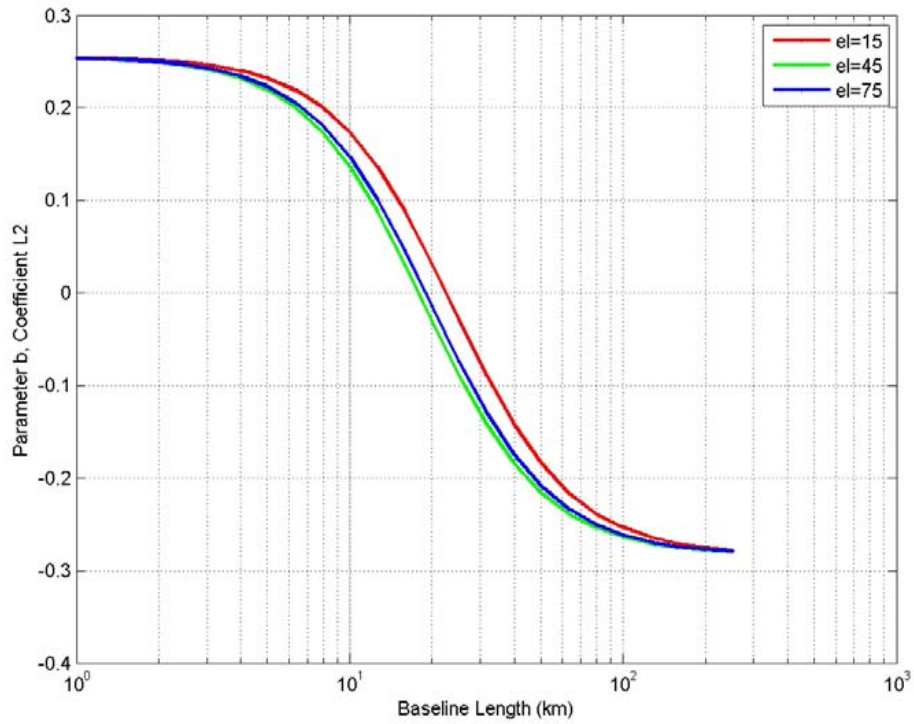
Figure 69 Values for the parameter b on L2. The values are presented for three different choices of elevation angles, namely 15, 45, and 75 degrees.
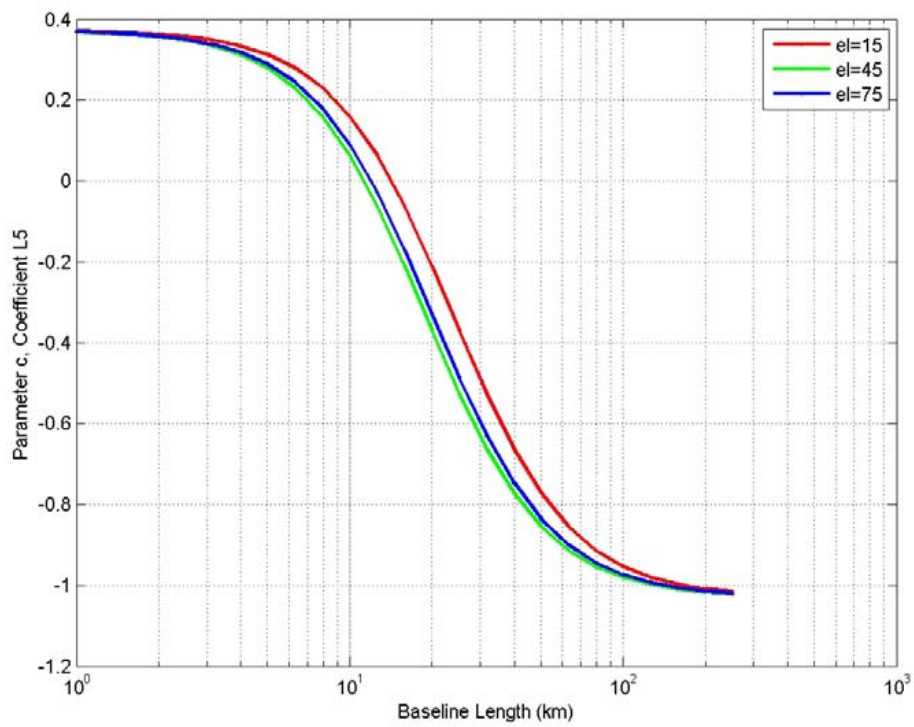

Figure 70 Values for the parameter c on L5. The values are presented for three different choices of elevation angles, namely 15, 45, and 75 degrees.

From the general formulations for *a*, *b* and *c*, we can calculate an ionosphere free combination for the three frequency combination as is done for the two-frequency combination with L3. We then find

$$\hat{\ell} \approx 2.31\ell_1 - 0.28\ell_2 - 1.03\ell_5$$

This result is similar to the combination presented by Odijk [2003] for a L1/L2/L5 combination

$$\hat{\ell} \approx 2.33\ell_1 - 0.36\ell_2 - 0.97\ell_5$$

which we obtain from our general formula by assuming identical measurement noise on the observables from all three frequencies.

Conclusions

We have derived linear combinations of carrier phase observables from GPS and Galileo. These combinations are optimal in the sense that they are best linear unbiased estimators (BLUE) of the received phase [e.g., Kay, 1993]. These combinations can be used in the processing of the observed GPS and Galileo data as a best choice on how to combine the different observables.

References

Emardson, Jarlemark, Bergstrand, Nilsson, and Johansson, CLOSE project report, SP report 2008, Lantmäteriet, Gävle, 2009.

Gauthier, L, P. Michel & J. Ventura-Traveset, and J. Benedicto, EGNOS: The First Step in Europe's Contribution to the Global Navigation Satellite System, ESA bulletin 105, 2001.

Hoffman-Wellenhof, B., Lichtenegger, H. & Collins, J., GPS: Theory & Practice. Springer-Verlag, Vienna New York, 4th ed., 1998.

Kay, Fundamentals of Statistical Signal Processing, Volume 1: Estimation Theory, Prentice Hall Inc., New Jersey, 1993.

Klobuchar, J. A., Ionospheric Effects on GPS, in Global Positioning System: Theory and Applications, edt. B. W. Parkinson and J. J. Spilker, vol.1, ch.12, p.485-514, 1996.

Odijk, Ionosphere-free phase combinations for modernized GPS, J of Surv. eng., DOI: 10.1061/(ASCE)0733-9453, 129:4(165), 2003.

Rizos, C, Network RTK research and implementation: A geodetic perspective, Journal of Global Positioning Systems, vol 1, 144-150, 2002.

Treuhaft R. N., G. E. Lanyi, The effects of the dynamic wet troposphereon radio interferometric measurements, Radio Sci., 22, 251-265, 1987.

9 Appendix III

According to the theory of atmospheric turbulence, the spatial variation in the ZWD, ℓ_w, between two locations $\mathbf{r}_i$ and $\mathbf{r}_j$ can be described using the structure function:

$$< \left[\ell_w(\mathbf{r_i}) - \ell_w(\mathbf{r_j}) \right]^2 > = k^2 \left\| \mathbf{r_i} - \mathbf{r_j} \right\|^{\alpha} \tag{C1}$$

where k^2 and α are constants. From theory of Kolmogorov turbulence we expect $\alpha = 2/3$ for distances larger than a few kilometres [*Treuhaft and Lanyi,* 1987]. However, many investigations have found α to be larger that $2/3$, closer to 1.

To describe temporal variations in the ZWD we can use the same expression by assuming that temporal variations are caused by the air moving with the wind (Taylor's frozen flow hypothesis), i.e. $\ell_w(\mathbf{r},t) = \ell_w(\mathbf{r} - \mathbf{v}(t - t_0), t_0)$ where $\mathbf{v}$ is the wind velocity, $\mathbf{r}$ the position and t the time. Thus, the variations in ZWD between location $\mathbf{r}_i$ at time t_i and location $\mathbf{r}_j$ at time t_j is described by the structure function:

$$< \left[\ell_w(\mathbf{r_i},t_i) - \ell_w(\mathbf{r_j},t_j) \right]^2 > = k^2 \left\| \mathbf{r_i} - \mathbf{r_j} - \mathbf{v}(t_i - t_j) \right\|^{\alpha} \tag{C2}$$

It should be noted that this assumes that the wind velocity is constant with height, which in general is not true. Furthermore, the frozen flow hypothesis may not be valid over very long time intervals.

We now consider the case that we have observations of $\ell_w(\mathbf{r}_0,t_0)$, $\ell_w(\mathbf{r}_1,t_1)$, $\ell_w(\mathbf{r}_2,t_2)$, , $\ell_w(\mathbf{r}_n,t_n)$ and want to use them to predict $\ell_w(\mathbf{r}_e,t_e)$. We choose $\ell_w(\mathbf{r}_0,t_0)$ as a reference and define $\delta\ell$ as:

$$\delta\ell(\mathbf{r},t) = \ell_w(\mathbf{r},t) - \ell_w(\mathbf{r}_0,t_0) \tag{C3}$$

The covariance between $\delta\ell(\mathbf{r}_i,t_i)$ and $\delta\ell(\mathbf{r}_j,t_j)$ will then be given by:

$$\begin{aligned}
< \delta\ell(\mathbf{r}_i,t_i) \cdot \delta\ell(\mathbf{r}_j,t_j) > = \frac{1}{2} \Big[& < \left[\ell_w(\mathbf{r_i},t_i) - \ell_w(\mathbf{r_0},t_0) \right]^2 > \\
& + < \left[\ell_w(\mathbf{r_j},t_j) - \ell_w(\mathbf{r_0},t_0) \right]^2 > \\
& - < \left[\ell_w(\mathbf{r_i},t_i) - \ell_w(\mathbf{r_j},t_j) \right]^2 > \Big]
\end{aligned} \tag{C4}$$

This expression can be evaluated by using (12).

In order to estimate $\ell_w(\mathbf{r}_e,t_e)$ we use a Minimum Mean Square Error (MMSE) estimator [*Kay,* 1993]. However, in order to calculate the MMSE estimate of $\ell_w(\mathbf{r}_e,t_e)$, $\hat{\ell}_w(\mathbf{r}_e,t_e)$, we need to know the Probability Density Function (PDF) of the ZWDs (or of the $\delta\ell$'s). Normally this is not known, however a good approximation is probably to assume that the $\delta\ell$'s have a Gaussian distribution, hence the joint PDF is given by:

$$p(\boldsymbol{\delta l}, \delta \ell_e) = \frac{1}{(2\pi)^{(n+1)/2} \det[C]} \exp\left\{-\frac{1}{2}\begin{bmatrix}\boldsymbol{\delta l}^T & \delta \ell_e\end{bmatrix} C^{-1}\begin{bmatrix}\boldsymbol{\delta l} \\ \delta \ell_e\end{bmatrix}\right\} \tag{C5}$$

where $\boldsymbol{\delta l} = [\delta \ell(\mathbf{r}_1, t_1), \delta \ell(\mathbf{r}_2, t_2), \ldots, \delta \ell(\mathbf{r}_n, t_n)]^T$ and $\delta \ell_e = \delta \ell(\mathbf{r}_e, t_1)$. The covariance matrix is given by:

$$C = \begin{bmatrix} <\boldsymbol{\delta l}\boldsymbol{\delta l}^T> & <\boldsymbol{\delta l}\delta \ell_e> \\ <\delta \ell_e\boldsymbol{\delta l}^T> & <\delta \ell_e^2> \end{bmatrix} = \begin{bmatrix} C_{mm} & C_{em} \\ C_{em}^T & C_{ee} \end{bmatrix} \tag{C6}$$

and can be calculated using (C5). Then the MMSE estimator of $\ell_w(\mathbf{r}_e, t_e)$ and its uncertainty will be given by [*Kay,* 1993]:

$$\hat{\ell}_w(\mathbf{r}_e, t_e) = \ell_w(\mathbf{r}_0, t_0) + C_{em}C_{mm}^{-1}\boldsymbol{\delta l} \tag{C7}$$

$$<\left[\hat{\ell}_w(\mathbf{r}_e, t_e) - \ell_w(\mathbf{r}_e, t_e)\right]^2> = C_{ee} + C_{em}C_{mm}^{-1}C_{em}^T \tag{C8}$$

In order to calculate the covariance matrix C we need to know k^2, which is generally not the case. However, it is easily realised that $C_{em} \propto k^2$ and $C_{mm}^{-1} \propto k^{-1}$, hence the MMSE estimator (C7) is independent of k^2. However, if we want to know the formal uncertainty of the estimator (equation (C8)) knowledge of k^2 is needed.

If not all observations are from the same time epoch we also need to know the wind velocity $\mathbf{v}$. Since this is generally not known we need to estimate it from the GPS data. This can for example be done by using a Maximum Likelihood (ML) estimator [*Kay,* 1993]. This means that the wind is obtained by choosing the $\mathbf{v}$ that maximises the PDF for $\boldsymbol{\delta l}$:

$$p(\boldsymbol{\delta l}; \mathbf{v}, k^2) = \frac{1}{(2\pi)^{n/2} \det[C_{mm}]} \exp\left\{-\frac{1}{2}\boldsymbol{\delta l}^T C_{mm}^{-1}\boldsymbol{\delta l}\right\} \tag{C9}$$

It turns out that in order to do this we also need to know k^2. Thus we make an ML estimation of k^2 also, and choose the values of $\mathbf{v}$ and k^2 that maximises (C9). The ML estimate of k^2, $\hat{k}^2$ is easily obtained by noting that $C(k) = k^2/k_0^2 C(k_0)$ where k_0^2 is some a priori value of k^2:

$$\hat{k}^2 = k_0^2 \frac{\boldsymbol{\delta l}^T C_{mm}(k_0)^{-1}\boldsymbol{\delta l}}{n} \tag{C10}$$

An expression for the ML estimate of the wind is not as easily obtained. Instead, it can for example be obtained by performing a grid search through all likely values of the wind velocity.

We have in the theory presented above assumed all stations to be at the same altitude. In general this will not be the case. To account for the small decrease of ZWD with height we use the following model to relate the ZWD observed at altitude h to a reference altitude h_0 [*Emardson and Johansson,* 1998]:

$$\ell_w(h) = \ell_w(h_0) \cdot \exp\left[-\frac{h - h_0}{H_{scl}}\right] \tag{C11}$$

where the scale height H_{scl} is taken to be 2 km in this work, corresponding approximately to the average water vapour scale height of the investigated area [*Nilsson et al.,* 2005].

10   Appendix IV

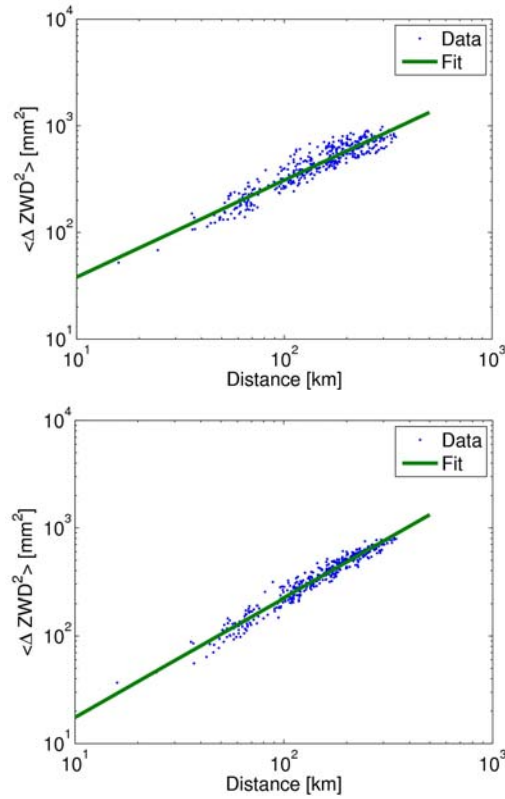This appendix shows examples of ZWD structure functions.

Figure 71   Spatial ZWD structure functions for July (left) and September (right) 2008.

Figure 71 shows the spatial structure function (equation (11)) for the months July and August 2008. The structure functions were calculated using ZWD data from 29 Swedish GPS stations located at latitudes between 56.5° and 59.0°. Shown are also a fit to (C1). This was done by estimating k^2 and α by fitting $\log[(l_w(\mathbf{r}_i) - l_w(\mathbf{r}_j))^2]$ to

$log(k^2) + \alpha \cdot \log(\mathsf{P}\mathbf{r}_i - \mathbf{r}_j\mathsf{P})$. This gave $k^2 = 4.7$ mm^2/km$^{0.91}$ and $\alpha = 0.91$ for the July period and $k^2 = 1.4$ mm^2/km$^{1.11}$ and $\alpha = 1.11$ for the August period.
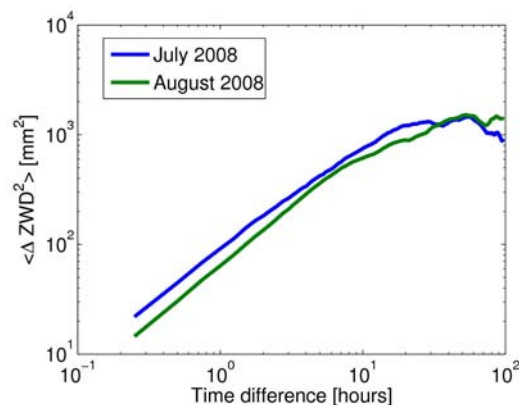
**Figure 72** **ZWD structure functions for the Borås station.**

In Figure 72 the temporal structure function for the Borås station, again for months July and August 2008. According to (12) we have that:

$$< [l_w(t_i) - l_w(t_j)]^2 >= k^2 \|\mathbf{v}\|^\alpha \, | t_i - t_j |^\alpha \tag{D1}$$

If we, in a similar way as before, fit the observed structure functions between 0 and 5 hours to this model, we get $k^2 \mathbf{P}\mathbf{v}\mathbf{P}^\alpha = 90.0 \text{ mm}^2 / \text{hour}^{0.98}$ and $\alpha = 0.98$ for July and $k^2 \mathbf{P}\mathbf{v}\mathbf{P}^\alpha = 64.2 \text{ mm}^2 / \text{hour}^{1.08}$ and $\alpha = 1.08$ for August.

SP Technical Research Institute of Sweden develops and transfers technology for improving competitiveness and quality in industry, and for safety, conservation of resources and good environment in society as a whole. With Sweden's widest and most sophisticated range of equipment and expertise for technical investigation, measurement, testing and certification, we perform research and development in close liaison with universities, institutes of technology and international partners.

SP is a EU-notified body and accredited test laboratory. Our headquarters are in Borås, in the west part of Sweden.
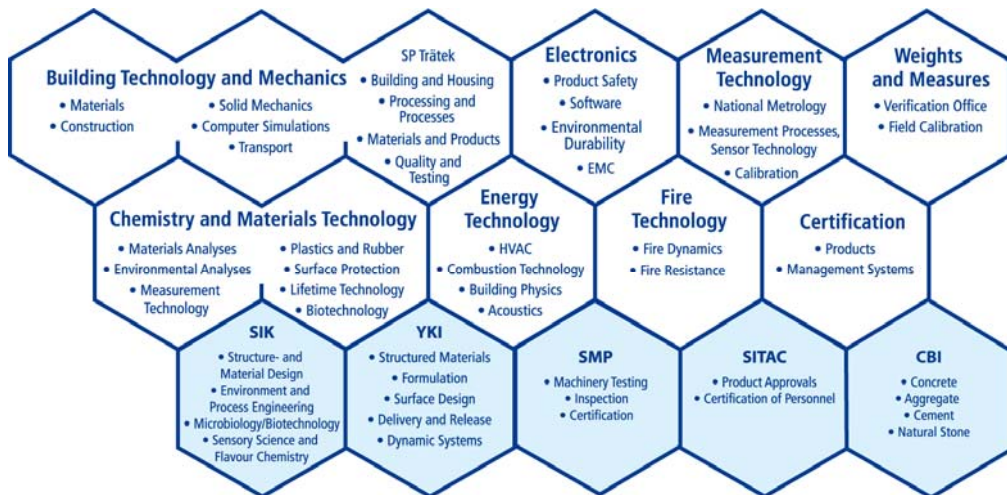
SP is organised into eight technology units and five subsidaries